Engineering Applications of Artificial Intelligence 163 (2026) 113130

Contents lists available at ScienceDirect

Engineering Applications of Artificial Intelligence

journal homepage: www.elsevier.com/locate/engappai

Solver-free artificial intelligence framework for stress-strain prediction and rapid field visualisation of fibre-reinforced polymer-confined recycled aggregate concrete

Temitope E. Dada [a,b], Guobin Gong [a,b,*], Jun Xia [a,b], Luigi Di Sarno [b]

[a] Department of Civil Engineering, Xi'an Jiaotong-Liverpool University (XJTLU), Suzhou, Jiangsu Province, 215123, PR China
[b] Department of Civil and Environmental Engineering, The University of Liverpool, Liverpool, L69 3GQ, United Kingdom

ARTICLE INFO

Keywords:
Artificial intelligence
Stress-strain prediction
Long short-term memory neural network
Deep learning
Surrogate visualisation
Fibre-reinforced polymer-confined recycled aggregate concrete

ABSTRACT

Accurately predicting the stress-strain behaviour of fibre-reinforced polymer (FRP)-confined recycled aggregate concrete (FRCRAC) remains challenging due to the complex mechanics introduced by recycled aggregate. This study presents a novel two-stage machine-learning (ML) framework with a mechanics-inspired visualisation module (MIVM) to predict and visualise the stress-strain behaviour of FRCRAC. First, Optuna-optimised Categorical Boosting (CATO) models are used to predict ultimate axial strength, axial strain, and hoop strain. These predictions are then integrated into Long Short-Term Memory (LSTMO) models to construct full axial and hoop stress-strain curves, forming a CATO-LSTMO framework. Trained via ten-fold cross-validation on a combination of 194 experimental and 600 synthetic datasets, CATO-LSTMO significantly outperforms conventional analytical and hybrid models with a coefficient of determination, R^2, above 98 %. Secondly, a solver-free MIVM that replicates finite element (FE) behaviour is proposed to enhance the physical interpretation of ML models. Three dedicated Categorical Boosting regressors are trained on over 350,000 nodal field outputs from Abaqus simulations to predict the three-dimensional stress, strain, and displacement distributions across 21 loading frames. These predictions are then scaled using the previously ML-generated stress-strain curves to reconstruct the frame-wise three-dimensional contour plots. The MIVM visualisations achieve results comparable to Abaqus outputs, while being about 500 times faster. This study contributes to artificial intelligence through novel hybrid ML frameworks and solver-free surrogate visualisation. The integrated CATO-LSTMO-MIVM framework is deployed as an interactive web application, and it offers practical use in engineering applications for rapidly estimating and visualising the stress-strain behaviour of FRCRAC.

1. Introduction

The advocacy for sustainability and recycling of demolition waste in construction projects is growing amidst the increasing need for virgin materials in construction. This campaign is targeted towards the efficient utilisation of resources and construction waste management. Specifically, recycled aggregates (RA) are being considered as replacements for natural aggregates (NA) to reduce the over-exploitation of NA reserves and the wastes that end up in landfills. While advancements have been made in studying the properties of RA and its effect on concrete, the adoption in structural application is still arguably low. This is because concrete containing RA, also known as recycled aggregate concrete (RAC), exhibits some undesirable properties (Qureshi et al., 2020; Kurad et al., 2017; Ali et al., 2023; Xie et al., 2018; Medina et al., 2014; Thomas et al., 2013; Behnood et al., 2015). Comparing some physical properties of RA to NA, RA typically has lower density, larger porosity and higher water absorption than NA (Li et al., 2021). Regarding rheology, RAC is often associated with reduced workability and flow compared to natural aggregate concrete (NAC) due to the rough edges and surfaces of RA (Kurad et al., 2017; Leite et al., 2013; Omer et al., 2024). Studies on the mechanical properties of RAC reveal that RA reduces the compressive and tensile strengths of concrete compared to NA. It is, therefore, important to deal with the effects of subpar properties in structural applications (Xie et al., 2018; Teng et al., 2016; Zhou et al., 2021).

One of the methods to enhance the behaviour of RAC is the external

* Corresponding author. Department of Civil Engineering, Xi'an Jiaotong-Liverpool University (XJTLU), Suzhou, Jiangsu Province, 215123, PR China.
E-mail address: guobin.gong@xjtlu.edu.cn (G. Gong).

https://doi.org/10.1016/j.engappai.2025.113130
Received 24 June 2025; Received in revised form 30 October 2025; Accepted 7 November 2025
0952-1976/© 2025 Elsevier Ltd. All rights are reserved, including those for text and data mining, AI training, and similar technologies.

strengthening with fibre-reinforced polymers (FRP). FRPs are composites with high tensile strength, strength-to-weight ratio, and corrosion resistance, amongst other good properties. FRP has emerged as an efficient solution to enhance the strength and deformation characteristics of RAC. This is because the desirable properties of FRP are used to counteract the weakness of RAC, consequently making the FRP-confined recycled aggregate concrete (FRCRAC) suitable for structural applications.

The mechanism of FRP-confined recycled aggregate concrete subjected to uniaxial compression is such that the FRP layers provide passive confinement to the concrete core. This confinement is in response to the lateral expansion of the concrete induced by the Poisson effect when loaded axially. For an effectively confined concrete column, the FRP continues to confine the concrete core until the failure of the FRP by rupture. This is illustrated in Fig. 1. The confining stress at failure is defined in Equation (1), as originally proposed by Lam & Teng (Lam and Teng, 2003a).

$$\text{Confining stress} f_l = \frac{2E_f \varepsilon_{h,rup} t_f}{D} \quad (1)$$

where $D, E_f, \varepsilon_{h,rup}, t_f$ represent the diameter of the concrete core, elastic modulus (MPa), rupture strain, and the thickness of the FRP jacket, respectively.

The mechanism of FRCRAC is complex, as there are multiple levels of interactions, including the FRP-concrete interface, fibre-matrix, aggregate-binder and the old mortar-old natural aggregate. These interactions make the accurate quantification of the ultimate strength, ultimate strain and the stress-strain response of FRCRAC challenging.

1.1. Existing stress-strain models of FRCRAC

The accurate prediction of stress-strain curves is fundamental to the study of the behaviour of structural elements such as FRP-confined recycled aggregate concrete (FRCRAC). The strength capacity and ductility of the structural element are illustrated by the shapes and points on the curves. For FRCRAC, the curve is obtained by plotting the stress values against the strain values till failure.

As illustrated in Fig. 2, the stress-strain curve of FRCRAC is typically divided into two portions and connected by a transition curve. For curves with strain hardening behaviour, the end of the first portion signifies the approximate capacity of the concrete core, which is also the point at which the capacity enhancement of the FRCRAC by FRP commences. The end of the second portion signifies the failure point of the FRP and the ultimate failure of the FRCRAC.

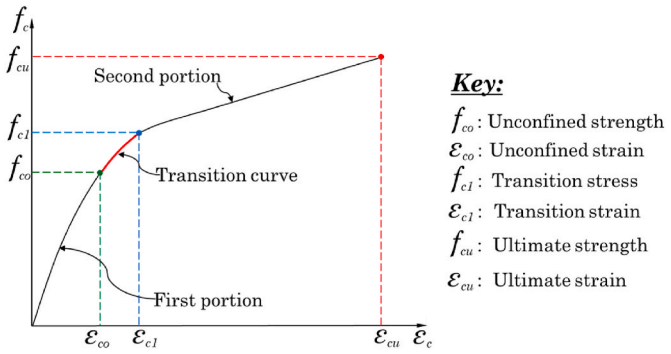

Fig. 2. The illustration of the typical stress-strain curve.

1.1.1. Empirical and analytical models

Many design-oriented and analytical equations have been proposed in previous studies to describe the stress-strain curves of FRP-confined concrete (Popovics, 1973; Richard and Abbott, 1975; Fardis and Khalili, 1982; Karbhari and Gao, 1997; Lam and Teng, 2003b; Xiao and Wu, 2003; Youssef et al., 2007; Teng et al., 2009). A significant number of the existing models were developed for FRP-confined natural aggregate concrete (FRCNAC) and afterwards adopted for FRCRAC. While the adopted FRCNAC models have performed well in some cases, there are two fundamental drawbacks: (1) determining the constituting parameters (ultimate conditions and others) of the models can be inaccurate because of the complexities introduced by RA. (2) the axial stress-strain equations to predict the curves can be unreliable as they mostly do not take into consideration the intricacies introduced by RA. Meanwhile, design-oriented and analytical models have been proposed to predict the stress-strain curve of FRCRAC, as demonstrated in some studies (Zhou et al., 2021; Zhao et al., 2014; Teng et al., 2016; Chen et al., 2018; Jiang et al., 2020), where some existing FRCNAC models are adopted as presented in Table 1 for predicting the stress-strain curves of FRCRAC.

1.1.2. Hybridised analytical-ML models

The ML approach has also been increasingly used to refine the analytical models for predicting more accurate stress-strain curves, leading to the development of hybrid analytical-ML frameworks. These approaches typically employ the ML models to predict the peak and ultimate conditions of FRCRAC (Dada et al., 2024; Xu et al., 2022; Zhang et al., 2024; Chen et al., 2025; Zhao et al., 2023), which are then integrated into analytical stress-strain formulations. For example, Zhao et al. (2023) used an XGBoost optimised with beetle antennae search (BAS) framework to refine the stress-strain model of Teng et al. (2009), by substituting the ultimate condition parameters with the ML predictions,

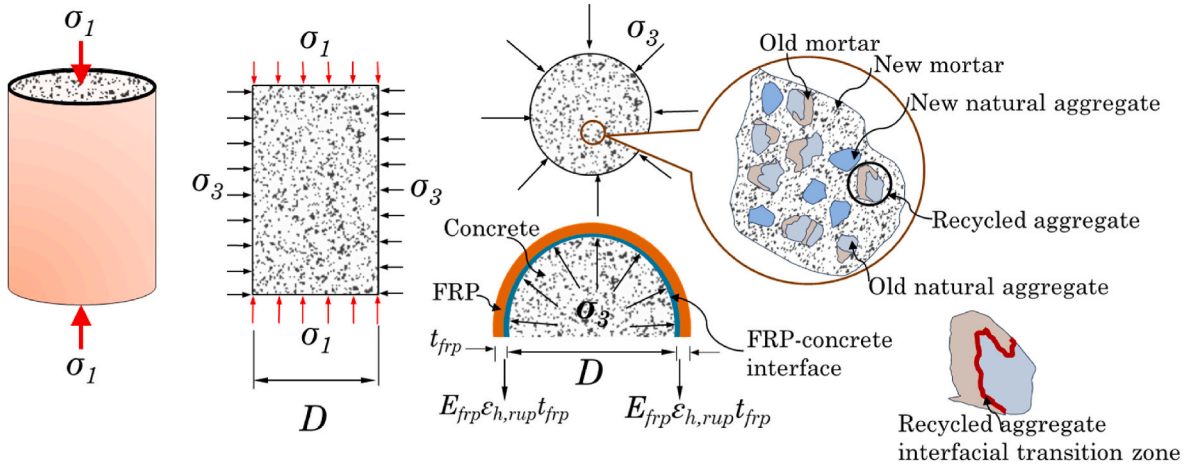

Fig. 1. The illustrative diagram of the mechanism of a confined concrete.

Table 1
Existing models to predict stress-strain curves of FRP-confined concrete.

Model	Year	Axial stress-strain curve equation	Ultimate condition equations	
			Strength	Strain
Richard and Abbott (1975)	1975	$f_c = \frac{(E_{c1}-E_{c2})\varepsilon_c}{\left\{1+\left[\frac{(E_{c1}-E_{c2})\varepsilon_c}{f_o}\right]^n\right\}^{\frac{1}{n}}} + E_{c2}\varepsilon_c$ $n = 1 + \frac{1}{\frac{E_{c1}}{E_{c2}}-1}$ $f_o = f_{cu} - E_{cu}\varepsilon_{cu}$, $E_{c1} = 4730\sqrt{f_{co}}$	–	–
Fardis and Khalili (1982)	1982	$f_c = \frac{E_c\varepsilon_c}{1+\varepsilon_c\left(\frac{E_c}{f_l}-\frac{1}{\varepsilon_{cu}}\right)}$	$f_{cu} = f_{co} + 4.1f_l$	$\varepsilon_{cu} = 0.002 + 0.001\left(\frac{E_{frp}t_{frp}}{Df_{co}}\right)$
Jolly and Lilistone (1998)	1998	$f_c = \begin{cases} 0.67\frac{f_{co}}{\gamma_m}\left[2\frac{\varepsilon_c}{0.002}-\left(\frac{\varepsilon_c}{0.002}\right)^2\right]+E_p\varepsilon_{cl} \\ f_c = 0.67\frac{f_{co}}{\gamma_m}+E_p\varepsilon_c \end{cases}$ $0.002 \le \varepsilon_c \le \varepsilon_{cu}$ $0 \le \varepsilon_c \le 0.002$	$f_{cu} = f_{co}\left(1+3.594\left(\frac{2t_{frp}}{D}\right)\left(\frac{E_{frp}\varepsilon_{frp}}{f_{co}}\right)\right)$ $\varepsilon_{lu} = 0.0117 + 0.0321\left(\frac{2t_{frp}}{D}\right)\left(\frac{E_{frp}}{E_c}\right)$	–
Xiao and Wu (2000)	2000	$f_c = \begin{cases} E_c\varepsilon_c + 2v_cf_l \\ 1.1f_{co} + \left[4.1 - 0.75\left(\frac{f_{co}^2}{E_l}\right)\right]f_l \end{cases}$ $1.1f_{co} < f_c \le f_{cu}$ $0 \le f_c \le 1.1f_{co}$ $v_c = 0.18$	$f_{cu} = 1.1f_{co} + \left[4.1 - 0.75\left(\frac{f_{co}^2}{E_l}\right)\right]f_l$	$\varepsilon_{cu} = \varepsilon_{co}\left(\frac{\varepsilon_{h,rup}+\varepsilon_o}{\varepsilon_{co}\mu_{tu}}\right)$, $\varepsilon_o = -0.0005\,\mu_{tu} = 7\left(\frac{E_l}{f_{co}}\right)^{-0.8}$
Lam and Teng (2003b)	2003	$f_c = \begin{cases} E_{c1}\varepsilon_c - \frac{(E_{c1}-E_{c2})^2}{4f_o}\varepsilon_c^2 \\ f_{co}+E_{c2}\varepsilon_c \end{cases}$ $\varepsilon_{c1} < \varepsilon_c \le \varepsilon_{cu}$ $0 \le \varepsilon_c \le \varepsilon_{c1}$ $f_o = f_{co}$, $\varepsilon_{c1} = \frac{2f_{co}}{E_{c1}-E_{c2}}$, $E_{c2} = \frac{f_{cu}-f_{co}}{\varepsilon_{cu}}$	$f_{cu} = f_{co} + 3.3\frac{f_l}{f_{co}}$	$\varepsilon_{cu} = \begin{cases} \left(1.75+12\left(\frac{f_l}{f_{co}}\right)\left(\frac{\varepsilon_{h,rup}}{\varepsilon_{co}}\right)^{0.45}\right)\varepsilon_{co} \\ \left(1.75+5.53\left(\frac{f_l}{f_{co}}\right)\left(\frac{\varepsilon_{frp}}{\varepsilon_{co}}\right)^{0.45}\right)\varepsilon_{co} \end{cases}$ FRP wrap FRP Tube
Lin and Li (2003)	2003	$f_c = f_{cu}\left[2\left(\frac{\varepsilon_c}{\varepsilon_{cu}}\right)-\left(\frac{\varepsilon_c}{\varepsilon_{cu}}\right)^2\right]$	$f_{cu} = f_{co} + f_l\tan^2\left(45^\circ+\frac{\phi}{2}\right)$ $\phi = 36^\circ + 1^\circ\left(\frac{f_{co}}{35}\right) \le 45^\circ$	$\varepsilon_{cu} = \varepsilon_{co}\left[1+2.24\tan^2\left(45^\circ+\frac{\phi}{2}\right)\frac{f_l}{f_{co}}\right]$
Youssef et al. (2007)	2007	$f_c = \begin{cases} E_c\varepsilon_c\left[1-\frac{1}{m}\left(\frac{\varepsilon_c}{\varepsilon_{c1}}\right)^{m-1}\right] \\ f_{c1}+E_{c2}(\varepsilon_c-\varepsilon_{c1}) \end{cases}$ $\varepsilon_c > \varepsilon_{c1}$ $0 \le \varepsilon_c \le \varepsilon_{c1}$ $\varepsilon_{c1} = 0.002748 + 0.1169\left(\frac{4t_{frp}E_{frp}\varepsilon_{l1}}{f_{co}}\right)^{0.857}\left(\frac{f_{frp}}{E_{frp}}\right)^{0.5}$ $\varepsilon_{l1} = 0.002$ $f_{c1} = f_{co} + 3f_{co}\left(\frac{4t_{frp}E_{frp}\varepsilon_{l1}}{Df_{co}}\right)^{1.25}$, $m = \frac{E_c\varepsilon_{c1}}{E_c\varepsilon_{c1}-f_{c1}}$ If $\rho_k < 0.01$ and $\varepsilon_{c1} < \varepsilon_c \le \varepsilon_{cu}$ If $\rho_k \ge 0.01$ and $\varepsilon_{c1} < \varepsilon_c \le \varepsilon_{cu}$ $0 \le \varepsilon_c \le \varepsilon_{c1}$	$f_{cu} = f_{co}\left(1+2.25\left(\frac{f_l}{f_{co}}\right)^{1.25}\right)$	$\varepsilon_{cu} = 0.003368 + 0.2590\left(\frac{f_l}{f_{co}}\right)\left(\frac{f_{frp}}{E_{frp}}\right)^{0.5}$
Teng et al. (2009)	2009	$f_c = \begin{cases} E_{c1}\varepsilon_c - \frac{(E_{c1}-E_{c2})^2}{4f_o}\varepsilon_c^2 \\ \begin{cases} f_{co}+E_{c2}\varepsilon_c \\ f_{co}-\frac{f_{co}-f_{cu}}{\varepsilon_{cu}-\varepsilon_{co}}(\varepsilon_c-\varepsilon_{co}) \end{cases} \end{cases}$ $f_o = f_{co}, \varepsilon_{c1} = \frac{2f_{co}}{E_{c1}-E_{c2}}, E_{c2} = \frac{f_{cu}-f_{co}}{\varepsilon_{cu}}, \rho_k = \frac{E_l}{(f_{co}/\varepsilon_{co})}$	$f_{cu} = f_{co} + 3.3\frac{f_l}{f_{co}}$	$\varepsilon_{cu} = \left(1.75 + 6.5\left(\frac{E_l}{f_{co}/\varepsilon_{co}}\right)^{0.8}\left(\frac{\varepsilon_{h,rup}}{\varepsilon_{co}}\right)^{1.45}\right)\varepsilon_{co}$
Zhou and Wu (2012)	2012	$f_c = \left[(E_{c1}\varepsilon_p - f_o)e^{\frac{-\varepsilon_c}{\varepsilon_p}} + f_o + E_{c2}\varepsilon_c\right]\left(1-e^{\frac{-\varepsilon_c}{\varepsilon_p}}\right)$ $f_o = f_{co} + 0.8(mf_{le}) + 10.7$, $E_{c2} = \frac{f_{cu}-f_o}{\varepsilon_{cu}}$ $\varepsilon_p = p\varepsilon_o$, $\varepsilon_o = f_o/E_{c1}$ p is the shape factor, ranging from 0 to 1	$f_{cu} = f_{co} + 3.3\frac{f_l}{f_{co}}$	$\varepsilon_{cu} = \left(1.75 + 6.5\left(\frac{E_l}{f_{co}/\varepsilon_{co}}\right)^{0.8}\left(\frac{\varepsilon_{h,rup}}{\varepsilon_{co}}\right)^{1.45}\right)\varepsilon_{co}$

(continued on next page)

Table 1 (*continued*)

Model	Year	Axial stress-strain curve equation	Ultimate condition equations	
			Strength	Strain
Dada et al. (2024)	2024	$f_c = \left[(E_{c1}\varepsilon_p - f_o)e^{\frac{-\varepsilon_c}{\varepsilon_p}} + f_o + E_{c2}\varepsilon_c\right]\left(1 - e^{\frac{-\varepsilon_c}{\varepsilon_p}}\right) f_o = f_{co}, E_{c1} = 4120\sqrt{f_{co}}$ for FRCRAC $E'_{c2} = \frac{f_{cu} - f_o}{\varepsilon_{cu}}$, $E_{c2} = wE'_{c2}$ $\varepsilon_p = p\varepsilon_o, \varepsilon_o = f_o/E_{c1}$ $p = \begin{cases} \frac{\rho_k}{E'_{c2}} = \frac{2E_{frp}t_{frp}\varepsilon_{cu}}{D(f_{cu} - f_{co})} \\ 1 \end{cases}$ FRCNAC FRCRAC ($p \geq 0.5$)	$f_{cu} = 0.877f_{co} + 7.254f_l^{0.734}$ General model for FRCNAC. $f_{cu} = 0.519f_{co} + 26.347f_l^{0.317}$ General model for FRCRAC. $f_{cu} = 0.417f_{co} + 21.621f_l^{0.432}$ For recycled concrete aggregate $f_{cu} = 0.816f_{co} + 7.107f_l^{0.766}$ For recycled brick aggregate	$\varepsilon_{cu} = \varepsilon_{co}\left(1 + \frac{\varepsilon_{h,rup} - 2.075\upsilon_c\varepsilon_{co}}{\varepsilon_{co}\mu_{tu}}\right)$ $\mu_{tu} = 5.338\left(\frac{\rho_c}{f_{co}}\right)^{-0.663}$ General model for FRCNAC. $\varepsilon_{cu} = \varepsilon_{co}\left(2.848 + 12.424\left(\frac{f_l}{f_{co}}\right)^{0.847}\right)$ For recycled concrete aggregate $\varepsilon_{cu} = \varepsilon_{co}\left(4.936 + 3.635\left(\frac{f_l}{f_{co}}\right)^{0.875}\right)$ For recycled concrete lump.

thereby significantly improving curve accuracy. Similarly, Dada et al. (2024) proposed a robust hybrid framework by modifying the existing analytical model of Zhou and Wu (2012) and refining the same with the prediction of the CatBoost model optimised with Optuna, achieving strong curve reproduction performance. More recently, Chen et al. (2025) utilised the least-squares boosting models to calibrate the model of Lam and Teng (2001), successfully reproducing the axial stress-strain curves of FRCRAC. While these hybrid solutions improve the estimation of the constitutive parameters, the problem of the analytical model not considering the intricacies of RA remains largely unsolved.

1.1.3. Sequential-based ML models

Beyond the predictions of ultimate parameters, recent studies have utilised ML algorithms with the capability to manage sequential data to predict stress-strain curves of materials and structures (Zhang et al., 2021; Fu et al., 2023; Meng and Pei, 2023). These algorithms, including the recurrent neural network (RNN), gated recurrent unit (GRU), and long short-term memory (LSTM), have been developed to handle historical memory dependence. Yang et al. (2024) utilised LSTM to predict the stress-strain curve of recycled aggregate concrete, with predictions better than analytical models. It seems that no existing study has applied LSTM to predict the stress-strain curve of FRCRAC despite its better accuracy. This study will utilise the LSTM algorithm to predict the stress-strain curve of FRCRAC. The performance will also be compared to existing analytical and hybrid analytical-ML models.

1.1.4. ML integrated with mechanics-inspired visualisation

While the accurate predictions of the ultimate conditions and stress-strain behaviour of structural elements are important in structural engineering, visualising the spatial distribution of the key parameters, such as stress, strain, and displacement, is also of significant interest (Ali et al., 2024; Chakrabarti et al., 2008; Bonifácio et al., 2019). To achieve this visualisation via simulation, the finite element (FE) method is a well-established method, as it enables detailed modelling of the confinement effects, load transfer, material deformation and failure mechanisms (Isleem et al., 2025). However, the application of FE to FRCRAC presents unique challenges. The heterogeneous composition of RA complicates the calibration of the material parameters such as stiffness degradation, damage evolution and plasticity properties (e Silva et al., 2021; Yu et al., 2021). Some of these parameters could be difficult to obtain experimentally, and as such, some level of uncertainty is introduced into conventional FE models. Meanwhile, FE can be computationally expensive and time-consuming while simulating nonlinear problems such as FRCRAC.

The machine learning (ML) approach can overcome some of the FE challenges, though with its own limitations. While ML requires high computational cost and time during training, the output during usage is near instantaneous, compared to FE, which requires meshing and solver convergence (Chakrabarti et al., 2008; Isleem et al., 2025; Bessa et al., 2017). However, ML models are limited by physical interpretability, especially in simulation validation and interactive visualisation of structural outputs. This limitation births the motivation for the development of ML frameworks with rapid computational performance and spatial explainability.

Combining ML with a mechanics-inspired visualisation module provides a promising alternative. Previous studies (Ali et al., 2024; Isleem et al., 2022, 2025) have used FE to generate synthetic data to augment experimental training datasets in ML (an approach referred to as FE-ML in this study). While this FE-ML has helped to improve ML performances, the earlier highlighted challenges associated with FE remain. In this study, we extend the FE-ML approach by integrating a CatBoost-LSTM (CATO-LSTMO) model with a mechanics–inspired visualisation module (MIVM) that predicts the full-field responses. In particular, a unique simulation-informed ML pipeline is introduced where the nodal stress, strain and displacement fields generated using Abaqus are used to train distinct CatBoost regression models. The models predict the spatial distribution of axial stress, axial strain and vertical displacement across the FRCRAC cylinder. The stress-strain curve obtained using the CATO-LSTMO is used to scale the ML-predicted field distribution, implying the construction of spatially resolved frame-wise contour plots without implementing a full FE solver. This is proposed to solve the challenge of complex calibrations and significantly reduce computational costs. More importantly, this approach enhances the interpretability of the ML framework as the mechanics-based visualisation gives physical insights into FRCRAC behaviour.

1.2. Research significance and aim of the study

This study aims to develop a robust and scalable hybrid machine learning (ML) framework that combines Optuna-optimised Categorical Boosting (CATO) and Long Short-Term Memory (LSTMO) models to predict and visualise the complete axial and hoop stress-strain responses of FRCRAC. The framework is enhanced with a finite element (FE)-inspired post-processing module to enable physics-informed visualisation of stress, strain, and displacement fields. The research helps to advance the predictive efficiency and interpretability of ML tools in structural engineering. The primary objectives of the study are as follows:

- To develop a categorical boosting model optimised with Optuna (CATO) to predict the ultimate strength, axial strain and hoop strain of FRCRAC based on geometric, material and confinement parameters.
- To integrate CATO with an LSTM-based sequential learning model (CATO-LSTMO) to predict the full axial and hoop stress-strain curves of FRCRAC.
- To generate nodal instances using finite element (FE) simulations and utilise them as training data for field-level ML models.

- To develop three CatBoost models based on the FE simulation data to accurately predict stress, strain and displacement field contours and integrate them with CATO-LSTMO curves for spatially resolved visualisation.
- To deploy the complete framework combining CATO-LSTMO and the visualisation framework as an interactive web-based application for practical applications.

1.3. Novelty and contributions of the study

The novel contributions of this study are highlighted in this section as follows:

- *Hybrid CATO-LSTMO framework:* A novel hybrid ML framework is proposed by combining an Optuna-optimised categorical boosting (CATO) with Long Short-Term Memory (LSTMO) to predict the full axial and hoop stress-strain curve of FRCRAC. This method improves prediction accuracy and generalisation. To the authors' knowledge, this is the first time this hybrid framework has been utilised for FRCRAC.
- *Novel Mechanics-inspired post-processing visualisation module:* A novel post-processing visualisation module inspired by the finite element (FE) principles is developed to transform ML-predicted stress-strain curves into spatially distributed stress, strain, and displacement fields. In contrast to the traditional finite element approach, this approach does not require constitutive law assumptions and complicated calibration of material properties, offering a more efficient alternative. Integrating ML predictions with mesh-based field reconstruction represents a new direction in interpreting ML models in structural engineering.
- *Simulation-informed ML dataset for nodal field prediction:* While FEM tools like Abaqus have been used in previous studies to generate training data for ML, such efforts have been focused on extracting scalar outputs (for instance, peak strength or strain). This study introduces a unique simulation-to-ML pipeline, where 351,540 nodal-level instances were extracted from 27 Abaqus simulations, each providing 21 frame-wise stress, strain and displacement fields. This helps to directly train ML models to predict field nodal values needed for spatial visualisation. This is the first study to train ML models to predict field-level responses for FRCRAC with nodal resolution.
- *Rapid, scalable visualisation with FEM-like fidelity:* The proposed integrated ML-visualisation framework achieves a near-instantaneous frame-wise prediction and visualisation of structural responses with computational inference speed over 500 times faster than Abaqus while delivering physically comparable results. This represents an efficient alternative to traditional FE solvers and can help with the rapid analysis and interpretation of FRCRAC.
- *Model development for practical use:* The full ML-MIVM framework is deployed as an interactive web-based application, providing an accessible tool for predicting the behaviour of FRCRAC without needing high-performance computing.

2. Methodology

2.1. Methodology workflow

The proposed methodology integrates a hybrid ML model with a mechanics-inspired post-processing module to predict the stress-strain behaviour and visualise the internal field responses of FRCRAC. The framework consists of two major components, namely the CATO-LSTMO and the ML-MIVM.

The workflow, shown in Fig. 3, begins with data collection and comprehensive data pre-processing. Next is the feature engineering to select the relevant features needed for the CATO and LSTMO frameworks. The database was augmented by generating synthetic data using kernel density estimation (KDE), with rigorous checks for the

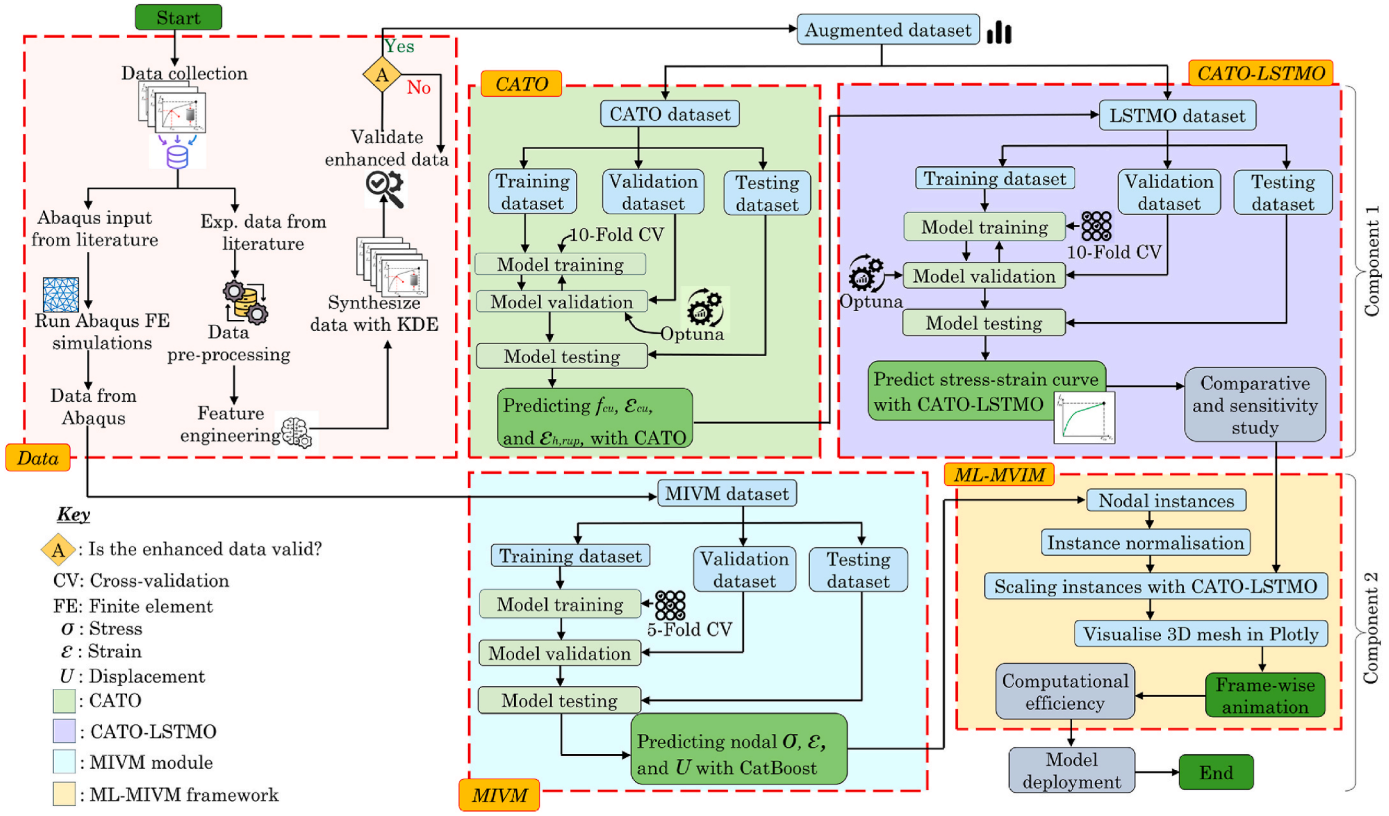

Fig. 3. Flowchart of methodology.

trustworthiness of the augmented data. The augmented dataset (794 samples: 194 experimental + 600 synthetic via KDE) is split into 70 % training (555 samples), 15 % validation (119 samples) and 15 % testing (119 samples) for both CATO and CATO-LSTMO. It is important to note that the testing set consists exclusively of original experimental samples to ensure an unbiased assessment of the generalisation.

The CATO was used to predict the ultimate strength, ultimate axial strain and ultimate hoop strain for FRCRAC. The CATO predictions were incorporated into the LSTMO training datasets, enabling sequential learning of the full axial and hoop stress-strain curves. The optimal hyperparameters of CATO and LSTMO were determined using Optuna in the validation set by applying a mean squared error (MSE) loss function over 1000 and 50 trials, respectively. The CATO and LSTMO models were trained on the best parameters via ten-fold cross-validation and evaluated using the four measures presented in Table 8. The predicted stress-strain curve of LSTMO was compared with the experimental values, and sensitivity analyses were carried out.

To support the visualisation component, auxiliary training datasets were generated using Abaqus finite element simulations across a design matrix of 27 parameter combinations. 21 frame-wise outputs over a mesh of 620 nodes were extracted from each simulation, with a total of 351,540 nodal instances. The simulation matrix was designed to capture the entire range of the CATO-LSTMO input conditions so as to ensure coherence between the predictive and visual components.

Furthermore, three separate CatBoost models were trained on the Abaqus data to predict nodal stress, strain and displacement values. The model was trained on 70 % of the datasets, validated on 15 % and tested on the remaining 15 %. Afterwards, the nodal field predictions were dynamically scaled using the stress-strain curve generated by the CATO-LSTMO, enabling a physics-informed field construction. In addition, the computational efficiency was evaluated by comparing the computational time for an identical analysis in Abaqus and the ML-MIVM framework.

Finally, a graphical user interface was built using Streamlit, and the entire ML-MIVM framework was deployed as an interactive web-based application. All implementations were carried out using Python 3.10.11, Scikit-learn 1.3.2, TensorFlow 2.9.0 and Optuna 1.2.2.

2.2. Categorical boosting

The categorical boosting (CatBoost) is an ensemble algorithm developed by Prokhorenkova et al. (2018). It combines gradient boosting with ordered boosting and efficient handling of categorical features. The ordered boosting approach was used to solve the problem of prediction shift and target leakage associated with the gradient-boosting decision tree (GBDT). The combination of the ordered boosting with a newly developed algorithm to handle categorical features more efficiently birthed CatBoost. CatBoost learns complex patterns using the novel leaf-wise tree growth. The detailed mathematical description and implementation of CatBoost for FRCRAC can be found in Prokhorenkova et al. (2018).

2.3. Long short-term memory

Standard neural networks, a computer system of algorithms developed based on the mechanism of the human brain to learn patterns in data, have a major shortcoming of learning from scratch every time. Recurrent neural networks (RNNs) were used to address the "forgetfulness" problem. However, RNNs also have the challenge of remembering things for a long time because of the vanishing and exploding gradients problems. Hochreiter and Schmidhuber (1997) addressed these problems in 1997 by introducing the Long Short-Term Memory (LSTM) model, a type of RNN that uses memory cells and control gates to determine what to remember or forget over time. This is illustrated in the schematic diagram in Fig. 4. The memory cells, which are the constant error carousels (CEC), help to maintain the error signal within the cell store of each unit and update information over time. The gates (input gate, forget gate, and output gate) are the controllers that help to

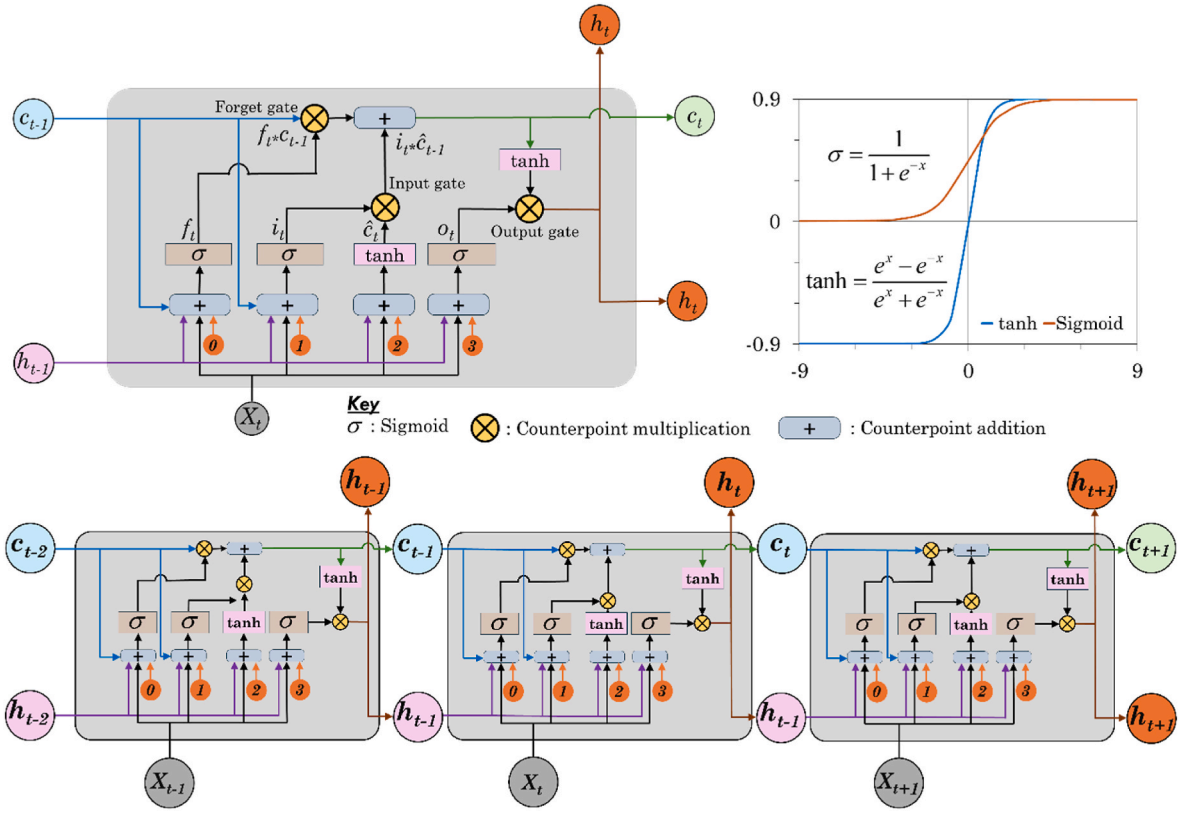

Fig. 4. Schematic diagram of LSTM.

regulate the inflow and outflow of information to and from the CEC. The three gates and the memory cell form the fundamental LSTM components.

2.3.1. Forget gate

The forget gate was introduced by Gers et al. (2000) to determine the amount of old data in the CEC to be forgotten. The forget gate uses the sigmoid σ activation function to compute a value between 0 (completely forget) and 1 (completely keep) for each number in the cell state. The forget gate f_t can be expressed mathematically by Equation (2).

$$\textit{Forget gate} \quad f_t = \sigma\left(W_f \cdot [h_{t-1}, X_t] + b_f\right) \tag{2}$$

where W_f and b_f are the weight matrix and bias vector of f_t, respectively. X_t is the current input vector at time t and h_{t-1} is the output vector from the previous time $t-1$. The sigmoid σ activation function can be expressed by Equation (3).

$$\textit{Activation function} \quad \sigma = \frac{1}{(1 + exp(-x))} \tag{3}$$

Non-useful information is discarded from the memory by combining the memory cell state c_{t-1} with the output of the forget gate as $f_t \cdot c_{t-1}$

2.3.2. Input gate

The input gate decides how much of the new information from the current input X_t, represented by the candidate cell state, $\widehat{C}_t$ should be added to the CEC c_t. This is expressed mathematically by Equation (4).

$$\textit{Input gate} \quad i_t = \sigma(W_i \cdot [h_{t-1}, X_t] + b_i) \tag{4}$$

2.3.3. Memory cell

The candidate cell state is a function of the current input X_t and the previous hidden state h_{t-1}. This is represented in Equation (5).

$$\textit{Candidate cell} \quad \widehat{C}_t = tanh(W_C \cdot [h_{t-1}, X_t] + b_C) \tag{5}$$

where W_i and b_i are the weight matrix and bias vector of i_t, respectively. Also, W_c and b_c are the weight matrix and bias vector of the memory cell state c_t. tanh is the hyperbolic tangent function given by Equation (6).

$$\textit{Hyperbolic tangent function}, \quad tanh = \frac{[exp(x) - exp(-x)]}{[exp(x) + exp(-x)]} \tag{6}$$

The memory cell state (also the CEC) c_t is then updated by combining the effects of the forget and input gates. This can be represented by Equation (7).

$$CEC, \quad c_t = f_t \cdot c_{t-1} + i_t \cdot \widehat{C}_t \tag{7}$$

2.3.4. Output gate

The output gate o_t controls the flow of information from the current memory cell to the next hidden state, which is also the output of the LSTM unit. The result of the output gate can be computed using Equation (8).

$$\textit{Output gate} \quad o_t = \sigma(W_o \cdot [h_{t-1}, X_t] + b_o) o_t = \sigma(W_o \cdot [h_{t-1}, X_t] + b_o) \tag{8}$$

The hidden state h_t is then computed by filtering the cell state using a tanh function and then multiplying it by the result of the output gate, as expressed in Equation (9).

$$\textit{Hidden state} \quad h_t = o_t \cdot tanh(c_t) \tag{9}$$

where W_o and b_o are the weight and bias vectors of o_t, respectively.

2.3.5. Multi-output LSTM model

In this study, a pair of stress and strain values was predicted at every point, which makes the LSTM multi-output. This is achieved by passing the hidden state h_t through a fully connected layer to produce multiple outputs simultaneously. Mathematically, the output layer is then modified as expressed in Equation (10).

$$\textit{Output layer} \quad \widehat{Y}_t = W_{out} \cdot h_t + b_{out} \tag{10}$$

where W_{out} and b_{out} are the weight and bias vectors of the output layer, respectively. $\widehat{Y}_t$ represents the predicted multi-output at time t.

2.4. LSTM for FRCRAC architecture

The architecture of the LSTM framework to predict the stress-strain behaviour of FRCRAC with its components, as presented in Fig. 5, is discussed in this section. The framework is broadly categorised into the input, hidden, and output layers. The hidden layers contain the Dense, RepeatVector, LSTM, Dropout and TimeDistributed layers. The input layer processes the static feature vector of FRCRAC [X_1,X_2,X_3,X_4,...,X_t], which includes geometry, material, confinement and CATO-predicted ultimate conditions, and passes it to the Dense layer. The Dense layer contains a tunable number of hidden units (optimised with Optuna), and the ReLU activation function transforms the raw input into higher-level features suitable for subsequent sequence generation.

Next, the RepeatVector layer replicates the processed feature vector 25 times to match the desired sequence length for the LSTM processing. This expansion fixes the input sequence length at 25 steps, corresponding to the 25 discretised points along the stress-strain curve. Although each time step receives the same feature information, the recurrent hidden states of the LSTM evolve across the sequence, enabling the model to generate the sequential progression of the curve over the 25 points. This discretisation was used to model both the axial and hoop stress-strain curves.

The output of the RepeatVector layer is connected to the two stacked LSTM layers, each with tuneable hidden units and the standard LSTM activation functions (sigmoid for gating and tanh for state updates). These layers process the repeated sequence and capture the temporal dependencies within the data. A dropout layer is applied to prevent overfitting. Finally, a TimeDistributed Dense layer with two output units generates the stress and strain predictions for each of the 25 time steps, producing the complete predicted stress-strain curve of FRCRAC [$Y_1, Y_2, Y_3, Y_4, \ldots, Y_t$].

The following information about the specimen is presented for FRCRAC: geometry properties (diameter D and height H), properties of aggregates (aggregate type A_t, maximum size $R_{\max}$ and percentage content of the RCA R_c), properties of binder (water-to-cement ratio w/c), properties of plain concrete (peak strain ε_{co} and strength f_{co}), properties of FRP (thickness t_f and modulus E_{frp}), properties of confined concrete (ultimate axial strain ε_{cu}, hoop strain $\varepsilon_{h,rup}$, and strength f_{cu}) were provided.

2.5. CatBoost and LSTM optimisation with Optuna

It is often exhaustive to search for the optimal combinations of hyperparameters for ML and deep learning algorithms. Six hyperparameters of CatBoost and four hyperparameters in the LSTM network were optimised using Optuna, with the Tree-structured Parzen Estimator (TPE) sampler. Optuna, a next-generation Bayesian-based optimisation framework, was developed by Akiba et al. (2019), and it allows for a dynamically constructed search space through the "define-by-run" programming philosophy. The framework is robust and enables user-defined customisation through its sampling and pruning algorithms. It is also more efficient than other frameworks such as random search, Beetle Antennae Search, GridSearchCV, and Particle Swarm Optimisation. Hereafter, the LSTM and CatBoost optimised with Optuna are represented by LSTMO and CATO, respectively. Mathematically, Optuna operates through the objective function, Bayesian optimisation and pruning. These are defined as follows:

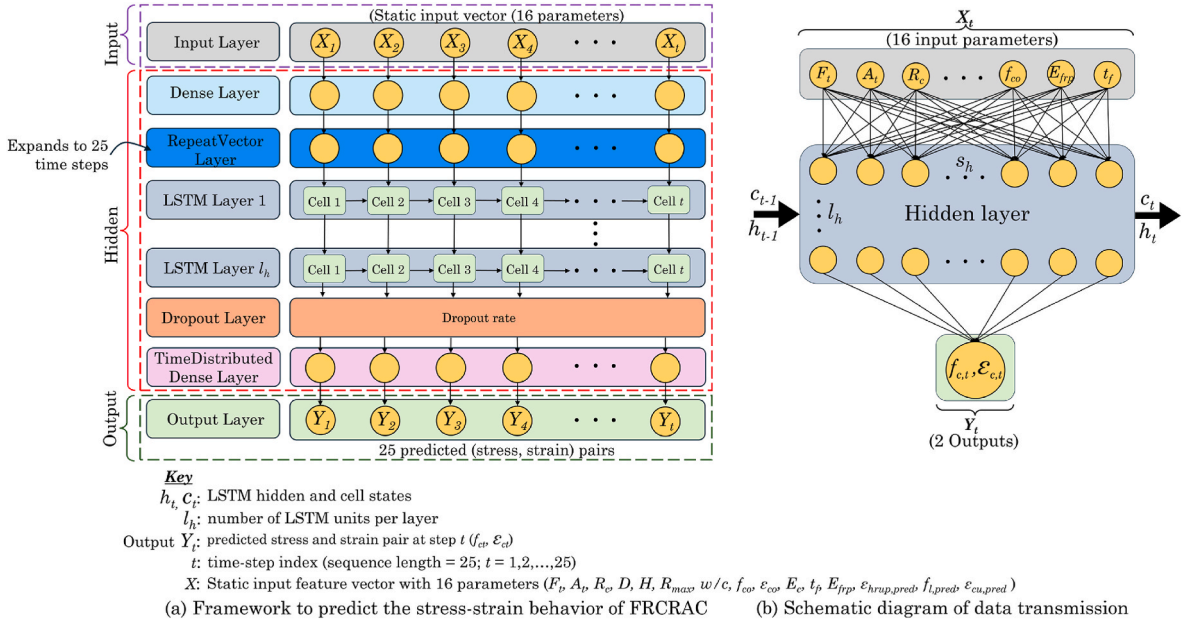

Fig. 5. The LSTM framework architecture.

$$\textit{Objective function} \quad f(x) : \mathbb{R}^d \rightarrow \mathbb{R} \tag{11}$$

where $f(x)$ is the value to be minimised or maximised and x is the vector of hyperparameters to be optimised.

Optuna uses Bayesian optimisation to model the objective function probabilistically by maximising the acquisition function $a(x)$ as follows:

$$x_{next} = \underset{x}{\operatorname{argmax}} a(x|D) \tag{12}$$

where x_{next} is the next hyperparameter set and $a(x|D)$ is based on the previous trial D.

The efficiency of Optuna is based on its ability to stop early poor-performing trials, which is known as pruning. The pruning criterion is defined as:

$$\textit{Pruning criterion} \quad g(x,t) < \textit{threshold} \tag{13}$$

where $g(x,t)$ denotes the performance of the model at step t. If the performance falls below a specified threshold, the trial is terminated early.

The hyperparameters optimised in CATO and LSTMO in this study are briefly described in this section, and the search ranges are presented in Table 2.

The following hyperparameters for CATO are described as follows:

- *Learning_rate:* The learning rate controls the step size of each iteration with which the gradient optimisation algorithm learns. This enhances stability and prevents overfitting, but it also increases training time.
- *Depth:* This is the depth of the trees in the ensembles, and the maximum depth of each tree is determined in the boosting process. Shallow trees capture simpler patterns, while deeper trees increase capacity, though too much could lead to overfitting.
- *L2_leaf_reg:* This is the regularisation parameter that penalises large weights in leaf nodes, which helps to prevent overfitting. It is the strength of L2 regularisation applied to the model weight.
- *Bagging_temperature:* This parameter determines the level of randomness when sampling the building trees. High bagging temperature value increases the randomness and improves the robustness of the model.
- *Border_count:* This controls the quality of the decision tree as it specifies the number of splits for numerical features.
- *Iterations:* This is the number of boosting iterations (trees) to train, and it determines the number of trees in the ensemble. High iterations can improve accuracy, but also increase training cost.

Table 2
Hyperparameters and search ranges for CATO and LSTMO.

Framework	Hyperparameter	Search Range
CATO	learning_rate	0.01–0.3
	depth	4–10
	l2_leaf_reg	1e-5 – 10 (log scale)
	bagging_temperature	1e-4 – 1 (log scale)
	border_count	32–256
	iterations	100–500
LSTMO	Units	32–128
	Dropout	0.2–0.5
	Epoch	10–100
	Batch size	16–128

The following hyperparameters for LSTMO are described as follows:

- *Units:* This parameter determines the number of hidden units in the LSTM layers. This determines the capacity of the model to learn complex patterns, and a large number of units improves performance.
- *Dropout:* The dropout rate is defined by the dropout parameter. This is a regularisation technique that prevents overfitting by randomly dropping out units during training. Generally, high dropout rates increase regularisation, but it can be detrimental to learning when too high.
- *Epoch:* The epoch controls the number of iterations during training. This is essentially the number of times the entire dataset is seen during training. High epochs improve model performance, but they also increase training time.
- *Batch size:* The batch size parameter controls the number of samples processed before updates. Large batch sizes generally reduce training time, but they hinder convergence and generalisation.

The search spaces were selected to balance model complexity, convergence stability, and computational efficiency. For CATO, Optuna

explored hyperparameters that regulate learning rate, depth, regularisation, randomness and tree growth. Furthermore, the number of hidden units, dropout rate, training epochs and batch size were the hyperparameters tuned in the LSTMO framework. For both frameworks, the optimisation objective was to minimise the validation mean squared error (MSE), and the best hyperparameter sets identified are presented in Tables 10 and 11 in the results section.

For the CATO framework, 1000 Optuna trials were used because of the wider hyperparameter search space (some containing log-scaled continuous ranges) and the computational efficiency of the categorical boosting algorithm, which allowed exhaustive search. In contrast, only 50 trials were set for LSTMO, as the hyperparameter space was smaller and the training is significantly more computationally expensive. The pruning mechanism of Optuna ensured that poor-performing LSTMO trials were terminated early, and preliminary runs confirmed that the validation performance stabilised well within 50 trials.

2.6. Database development for CATO-LSTMO

The database development was split into two broad categories. The first is for the CATO-LSTMO framework, and the second is for the post-processing framework. The database for the CATO-LSTMO contains 194 experimental observations of FRCRAC obtained from 10 published sources (Zhou et al., 2016, 2021; Zhao et al., 2014; Teng et al., 2016; Chen et al., 2018; Jiang et al., 2020; Gao et al., 2016; Xie and Ozbakkaloglu, 2016; Li et al., 2019; Nguyen and Livaoğlu, 2020). The summary and details of each specimen in the databases are presented in Tables A.1 and A.2, respectively, in the Appendix. While the aggregate types are broadly categorised into NA and RA, the RA types are further classified into three groups, namely, recycled concrete aggregate (RCA), recycled concrete lump (RCL) and recycled brick (RBA). Also, the FRPs were classified as carbon and glass types.

The experimental database spans a broad range of geometric, material and confinement properties. The diameter of the specimens varied between 100 and 300 mm, and height between 200 and 600 mm, ensuring a height-to-diameter ratio less than three. The aggregate replacement covered the full range of 0–100 %, and the water-to-cement ratios varied between 0.30 and 0.62. The unconfined compressive strength of the concretes ranged from 16.8 MPa to 78.4 MPa, with elastic moduli ranging between 18.6 GPa and 34.6 GPa. The thicknesses of the FRP jackets range between 0.11 mm and 3.40 mm, and the FRP tensile strengths between 42 and 236 MPa. At ultimate conditions, the confined compressive strength reached up to 161 MPa and the ultimate strains up to 3.36 %. This range of parameters demonstrates that the database encompasses a representative spectrum of realistic FRCRAC behaviour, thereby providing a robust basis for training, validating and testing the CATO-LSTMO framework.

2.7. Data pre-processing and augmentation for CATO-LSTMO

This section presents the full data pipeline used for CATO and LSTMO, including preprocessing of the raw dataset (filtering and encoding), augmentation with KDE, validation with synthetic data trustworthiness, feature engineering, and standardisation. These steps ensured that the models were trained on a statistically representative and physically realistic dataset.

The 194 observations were pruned down from the initial 281 collected from the literature after pre-processing. The 281 data were filtered using four criteria: (1) only the specimens with the record of the strain (unconfined, ultimate and rupture strain) values, (2) a height-to-diameter ratio of less than three to prevent the effect of failure due to slenderness, (3) a record of the effective water-to-cement ratio and (4) a record of the percentage content of RCA were considered.

The histogram showing the distributions of the variables in Fig. 6 shows that the RA replacement ratios are concentrated below 50 % but extend up to 100 %, reflecting both common experimental practice and extreme replacement cases. The water-to-cement ratios (0.30–0.62) span mixes from low-to high-strength concretes, while the unconfined compressive strengths (16.8–78.4 MPa) capture the behaviour of both the weak and structural-grade concretes. The FRP tensile strength (42–236 MPa) and thicknesses (0.11–3.40 mm) distribution also demonstrates that the database covers confinement scenarios from weak to strong confinements. The correlation heatmap in Fig. 7 further highlights meaningful physical relationships. For instance, higher RA content correlates with lower ultimate compressive strength, while FRP thickness and tensile strength correlate positively with confined strength and strain capacities. These observed relationships confirm that the database reflects realistic interdependencies in FRCRAC behaviour rather than isolated parameter ranges.

Building on this curated dataset, the existing 194 experimental observations within the database were further augmented using the kernel density estimation (KDE) method to generate an additional 600 datasets

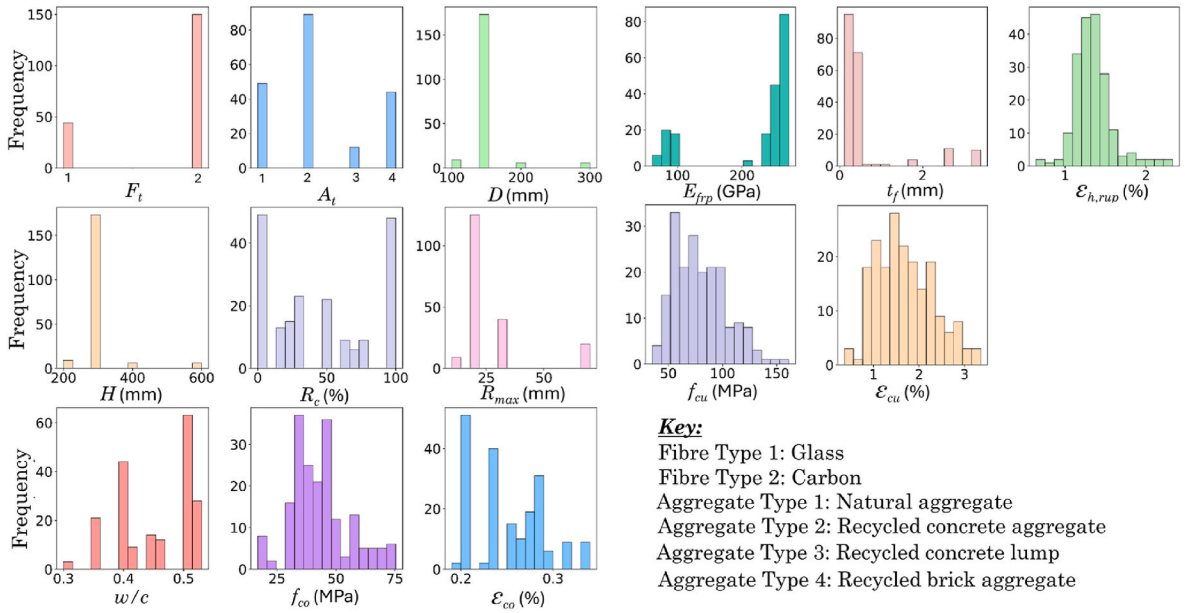

Fig. 6. Histogram of the FRCRAC database.

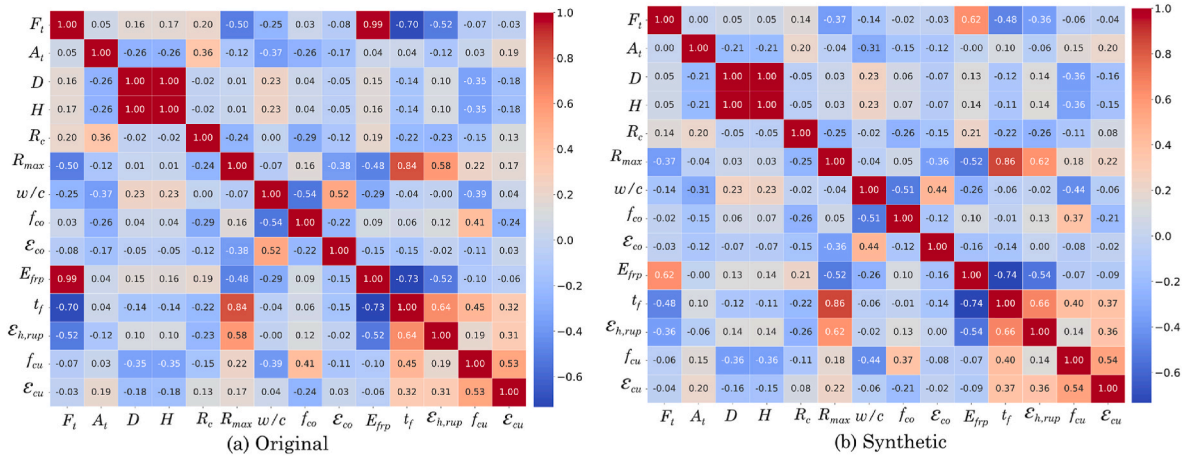

Fig. 7. The correlation matrices (a) original (b) synthetic.

to compensate for the limited FRCRAC experimental observations. The synthetic data were generated to be within the distribution and bounds of the original specimens, thereby preserving physical realism. The focus of the augmentation was to increase the variability of the training samples and improve the robustness of the CATO-LSTMO in capturing the stress-strain behaviours of FRCRAC. From a practical viewpoint, this augmentation is particularly relevant because of the expensive nature and limited availability of FRCRAC data. Therefore, this approach enhances the available datasets, supporting the development of predictive tools that can be reliably applied in real-world applications.

2.7.1. Kernel density estimation data augmentation

The Kernel density estimation is a technique used to estimate the probability density function (PDF) of random variables from a finite data sample. In this case, the PDF of the original dataset is estimated, and new data points are generated. The kernel function K (a Gaussian distribution in this study) is placed at each data point x and afterwards summed to form a smooth probability density curve. This can be expressed mathematically in Equation (14) as:

$$KDE\ function \quad f(x) = \frac{1}{nb}\sum_{i=1}^{n} K\left(\frac{x - x_i}{b}\right) \tag{14}$$

where K is the kernel function, b is the bandwidth parameter and n is the number of data points. Furthermore, new data points are generated by randomly sampling the estimated distribution. This creates synthetic data with statistical properties similar to those of the original datasets. For this study, a bandwidth of 0.2 and a n value of 600 datasets were used.

2.7.2. Data quality of the enhanced dataset

The quality of the additional 600 datasets generated with KDE was evaluated to ensure bias is not introduced into the augmented datasets. The column shape and pair trend scores of 92.20 % and 93.73 % were achieved, with an average score of 92.97 %. This signifies a high quality of the synthetic data. Other methods used for further evaluation include comparing the statistical properties of the original and synthetic databases. The split feature validation technique (SFVT) was also used to confirm the quality of the generated data. Furthermore, the Pearson correlation matrices, empirical cumulative distribution function curves and the 10-fold cross-validation using extreme gradient boosting (XGBoost) regressor were implemented to check the trustworthiness of the dataset.

- *The Pearson correlation matrices:*

The correlation matrices of the original and synthetic datasets were also evaluated. As shown in Fig. 7, the heatmaps for both databases show similarities in pattern and intensity. This implies that the generated synthetic data is of high quality.

- *The empirical cumulative distribution function:*

The distribution of each parameter in the database was evaluated using the empirical cumulative distribution function (ECDF) to identify the outliers.

The result in Fig. 8 shows good agreement between the distribution of the original, synthetic and augmented datasets.

- *The split feature validation technique:*

The split feature validation technique (SFVT), a novel method developed by Dada et al. (2024) was implemented for two secondary features, namely confinement stress and confinement stiffness. The result showed a testing R^2 of 99.51 % and 98.63 % for the confinement stress and the confinement stiffness, respectively.

- *Statistical analysis of databases:*

An established, thorough way to check the quality of the generated data is by comparing the statistical properties of both original and synthetic datasets. The minimum, maximum, average values and standard deviations were computed, and the results in Tables 3–4 showed good similarities between the original and synthetic database. This confirms the high quality of the generated datasets without bias.

- Ten-fold cross-validation:

The ten-fold cross-validation was applied to the original (194) and augmented (794) datasets using the extreme gradient boosting (XGBoost) regressor to predict the ultimate conditions of the FRCRAC. The performance result in Table 5 shows significant improvement in the performance of the model with the augmented datasets, especially for the hoop strain.

Collectively, these validation results demonstrate that the synthetic datasets expand the training sample size, while preserving the statistical fidelity and physical realism of the original database. This improves the robustness of CATO-LSTMO without compromising its real-world applicability to FRCRAC.

2.7.3. Feature engineering

In this section, the selection and development of new features for optimum performance of the LSTMO model were carried out. Two new

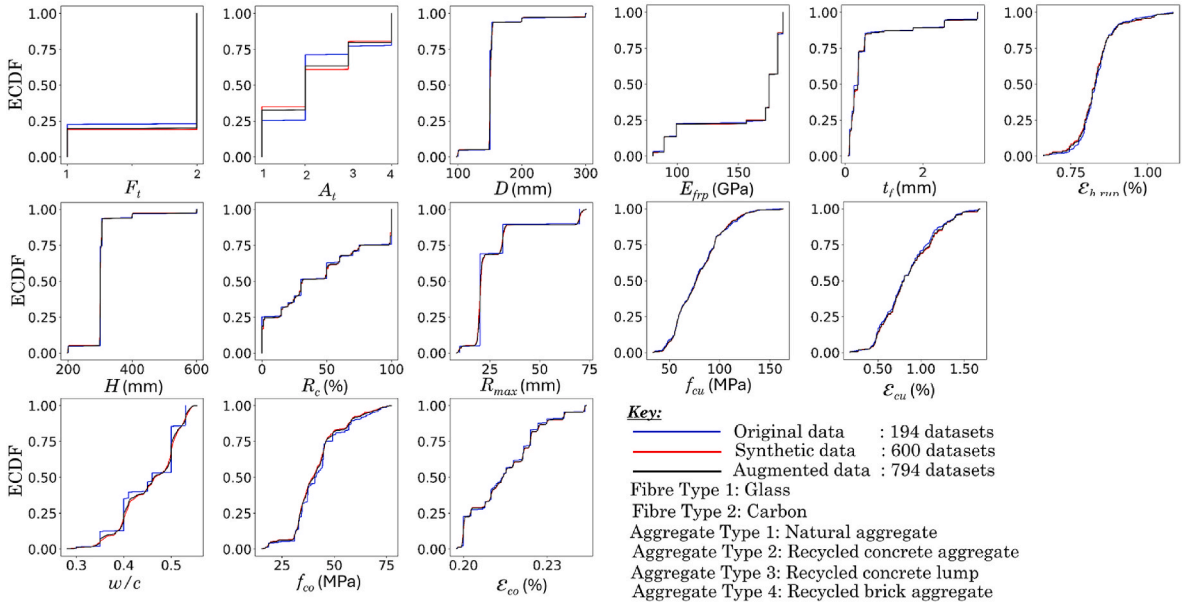

Fig. 8. The ECDF for original, synthetic and augmented datasets.

Table 3
Statistical properties of the original FRCRAC database.

	Parameter	Description	Unit	Min. Value	Max. Value	Average	Std.
Aggregate	A_t	Aggregate type	–	–	–	–	–
	R_{max}	Max RCA size	mm	10.00	70.00	27.06	15.52
	R_c	RCA content	%	0.00	100.00	45.18	38.30
Binder	w/c	Water/cement	–	0.30	0.53	0.45	0.06
Geometry	D	Diameter	mm	100.00	300.00	154.18	29.59
	H	Height	mm	200.00	600.00	308.71	59.19
Unconfined concrete	ε_{co}	Peak strain	%	0.19	0.35	0.25	0.04
	f_{co}	Peak strength	MPa	16.80	75.39	42.83	12.34
FRP	F_t	Fibre type	–	–	–	–	–
	t_f	FRP overall thickness	mm	0.11	3.40	0.60	0.87
	E_{frp}	FRP modulus	GPa	60.80	272.73	218.74	73.91
Confined concrete	f_{cu}	Ult. confined strength	MPa	35.17	161.26	79.33	23.85
	$\varepsilon_{h,rup}$	Rupture strain	%	0.64	2.33	1.35	0.25
	ε_{cu}	Ult. axial strain	%	0.36	3.36	1.69	0.62

Table 4
Statistical properties of the synthetic FRCRAC database.

	Parameter	Description	Unit	Min. Value	Max. Value	Average	Std.
Aggregate	A_t	Aggregate type	–	–	–	–	–
	R_{max}	Max RCA size	mm	8.36	73.28	27.26	15.91
	R_c	RCA content	%	0.00	100.00	45.33	37.86
Binder	w/c	Water/cement	–	0.28	0.55	0.46	0.06
Geometry	D	Diameter	mm	97.67	300.97	153.59	27.81
	H	Height	mm	197.44	600.96	306.93	55.61
Unconfined concrete	ε_{co}	Peak strain	%	0.19	0.35	0.25	0.04
	f_{co}	Peak strength	MPa	15.40	77.43	41.50	11.87
FRP	F_t	Fibre type	–	–	–	–	–
	t_f	FRP overall thickness	mm	0.08	3.41	0.60	0.88
	E_{frp}	FRP modulus	GPa	60.80	272.73	218.86	73.07
Confined concrete	f_{cu}	Ult. confined strength	MPa	34.04	162.82	79.45	23.29
	$\varepsilon_{h,rup}$	Rupture strain	%	0.64	2.33	1.33	0.27
	ε_{cu}	Ult. axial strain	%	0.36	3.36	1.72	0.63

Note: Ult. = ultimate; min. = minimum; max. = maximum; std. = Standard deviation.

features, confinement stress f_l and concrete modulus, were calculated based on the proposition by Teng et al. (2009) and ACI, respectively. The input features for CATO and LSTMO are presented in Table 6.

Where $\varepsilon_{h,rup,pred}$ is the rupture strain predicted by CATO, distinguished from the experimental rupture strain $\varepsilon_{h,rup}$ in Equation (1). $f_{cu,pred}$, $\varepsilon_{cu,pred}$ are the predicted ultimate strength and ultimate axial strain using CATO. $f_{l,pred}$ is the confining stress (predicted) adapted from Equation (1).

$$\text{Confining stress (predicted)} \quad f_{l,pred} = \frac{2E_{frp}t_f\varepsilon_{h,rup,pred}}{D} \tag{15}$$

Table 5
The prediction of the ultimate conditions of original and augmented data using XGBoost.

Data	Ultimate Condition	Parameters	R^2 (%)	MAE (MPa/ $\times 10^{-2}$)	RMSE (MPa/ $\times 10^{-2}$)	MAPE (%)
Original	Strength	10-Fold CV	93.57	4.366	6.611	5.524
		Testing Data	94.25	3.614	5.086	5.328
	Axial Strain	10-Fold CV	79.10	0.176	0.249	11.305
		Testing Data	86.06	0.208	0.262	14.255
	Hoop Strain	10-Fold CV	89.30	0.049	0.067	3.776
		Testing Data	85.74	0.076	0.100	5.778
Augmented	Strength	10-Fold CV	95.42	2.687	4.361	3.550
		Testing Data	97.42	2.713	3.930	3.341
	Axial Strain	10-Fold CV	94.62	0.101	0.146	6.394
		Testing Data	97.20	0.076	0.099	4.773
	Hoop Strain	10-Fold CV	96.94	0.030	0.043	2.339
		Testing Data	93.28	0.045	0.067	3.450

Note: std. = Standard deviation.

Table 6
Input forms for CATO and LSTMO.

Framework	Target feature	Variables
CATO	$\varepsilon_{h,rup}$	$F_t, A_t, D, H, R_{max}, R_c, w/c, f_{co}, \varepsilon_{co}, E_c, t_f, E_{frp}$
	f_{cu}	$F_t, A_t, D, H, R_{max}, R_c, w/c, f_{co}, \varepsilon_{co}, E_c, t_f, E_{frp}, \varepsilon_{h,rup,pred}, f_{l,pred}$
	ε_{cu}	$F_t, A_t, D, H, R_{max}, R_c, w/c, f_{co}, \varepsilon_{co}, E_c, t_f, E_{frp}, \varepsilon_{h,rup,pred}, f_{l,pred}$
LSTMO	Axial (f_c, $\varepsilon_{c,a}$)	$F_t, A_t, D, H, R_{max}, R_c, w/c, f_{co}, \varepsilon_{co}, E_c, t_f, E_{frp}, \varepsilon_{h,rup,pred}, f_{l,pred} f_{cu,pred}, \varepsilon_{cu,pred}$
	Hoop (f_c, $\varepsilon_{c,h}$)	$F_t, A_t, D, H, R_{max}, R_c, w/c, f_{co}, \varepsilon_{co}, E_c, t_f, E_{frp}, \varepsilon_{h,rup,pred}, f_{l,pred} f_{cu,pred}, \varepsilon_{cu,pred}$

E_c is the concrete modulus calculated by the model proposed by Dada et al. (2024) for FRCRAC, as presented in Equation (16).

$$\text{Concrete modulus} \quad E_c = 4120\sqrt{f_{co}} \tag{16}$$

2.7.4. Standardisation of the dataset

Auto-scaling and standardisation are crucial to machine learning as they help prevent the overestimation of the influence of large data values. The standardisation in this study was implemented by normalising unscaled datasets with z-score using Equation (17).

$$\text{z} - \text{score} \quad Z = \frac{X - \mu}{\sigma} \tag{17}$$

where Z is the standardised value, X is the original value, μ is the average value and σ is the standard deviation of the feature.

2.8. Simulation-informed data generation and field model training

A simulation-informed dataset was generated using the finite element (FE) method to enable the spatial visualisation of stress, strain, and displacement fields. The commercial FE software Abaqus was used to simulate FRP-confined concrete under axial compression. Key material properties and geometry parameters were varied to match the ranges of the CATO-LSTMO training database.

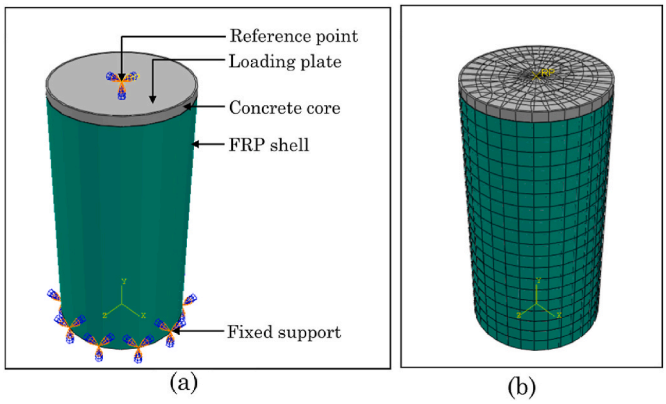

Fig. 9. The model for FRP-confined concrete in Abaqus (a) rendered assembly (b) mesh.

2.8.1. Simulation matrix design

27 FE simulations were conducted based on a factorial matrix combining three levels of the unconfined concrete strength (25, 50, 50 MPa), FRP thickness (0.11, 0.33, 0.55 mm), and FRP modulus (60, 150, 272 GPa). For each simulation, 21 frame-wise output steps were extracted to capture the full progression from the initial loading (0 %) to failure (100 %).

To enable consistent tracking and integration, each simulation instance was uniquely labelled. The label followed the format CS [Strength]_T [Thickness]_M [Modulus], where CS is the unconfined compressive strength in MPa, T is the overall FRP thickness in mm, and M is the FRP modulus in MPa. For example, the simulation label CS50_T33_M150K implies a simulation case with an unconfined strength of 50 MPa, FRP thickness of 0.33 mm and FRP modulus of 150 GPa.

2.8.2. FEM modelling and input parameters

All simulations were modelled as a cylinder, with each having a diameter of 150 mm and a height of 300 mm, maintaining a height-to-diameter ratio of 2. The height of the FRP was slightly reduced to 290 mm to ensure the load was not directly applied to the FRP from the top via the loading plate. The rendered assembly and the mesh of the model are presented in Fig. 9. The concrete is modelled using 3D elements (C3D8R), and the FRP (S4R) is modelled using shell elements. A surface-to-surface interaction was used to bond the concrete and the FRP parts. The boundary conditions included a fixed base and a displacement-controlled load applied at the top via a rigid plate. The dynamic explicit analysis was adopted due to contact interaction, nonlinear material behaviour and numerical stability (convergence).

A summary of the properties of concrete and FRP material is presented in Table 7. The concrete was defined using the concrete damage parameter (CDP), while the Hashin damage criterion was used for the FRP. The CDP and the stress-strain parameters for the unconfined concrete used were obtained from the study (Nguyen and Livaoğlu, 2020) as presented in Table 8.

A uniform mesh size of 15 mm was applied to all parts. For each simulation, the nodal-level von Mises stress, maximum principal strain, and displacement magnitudes were extracted. These outputs were collected at every frame using a custom Python script executed through the Abaqus command line interface. This extraction procedure resulted in a total of 351,540 nodal instances (27 simulations × 21 frames × 620

Table 7
The general and mechanical properties of the concrete and FRP.

Material	Density (tonnes/m^3)	Poisson's ratio	Modulus (GPa)
Concrete	2.30	0.2	15.42–30.26
FRP	1.56	0.3	60.80–272.27

Table 8
The concrete damage parameter for the modelling.

Dilation angle	Eccentricity	f_{bo}/f_{co}	K	Viscosity parameter
35	0.1	1.16	0.667	0.007985

Note: f_{bo}/f_{co} is the ratio of biaxial to uniaxial compressive strength, and K is the shape factor.

Table 9
The measures of the model performance for empirical and ML models.

Measure	Notation	Expression	Ideal Value
Coefficient of determination	R^2	$R^2 = 1 - \frac{\sum_{i=1}^{n}(y_i - \bar{y}_i)^2}{\sum_{i=1}^{n}(y_i - \bar{y}_i)^2}$	1
Root mean square error	RMSE	$RMSE = \sqrt{\frac{\sum_{i=1}^{n}\lvert(y_i - \bar{y}_i)^2\rvert}{n}}$	0
Mean absolute error	MAE	$MAE = \frac{\sum_{i=1}^{n}\lvert y_i - y_i'\rvert}{n}$	0
Mean absolute percentage error	MAPE	$MAPE = \frac{100\%}{n}\sum_{n=1}^{n}\left\lvert\frac{y_i - y_i'}{y_i}\right\rvert$	0

Note: where y' = predicted value, y = experimental value, $\bar{y}$ = mean predicted value, $\bar{y}$ = mean experimental value, μ_y = standard deviation of the predicted value, $\mu_{y'}$ = standard deviation of the experimental value, n = number of samples.

nodes), which formed the training dataset for CatBoost-based field-level regressors in subsection 2.8.3.

2.8.3. Field ML model training

The data obtained via simulation in subsection 2.8.2 is used to train three distinct CatBoost models. The models were developed to predict field-level stress, strain and displacements based on the four inputs, including unconfined strength, FRP thickness, FRP modulus and the Abaqus frame index. The data were standardised using the Min-Max normalisation. The dataset was split into 70 % training, 15 % validation, and 15 % testing subsets. Performance metrics included R^2, MAE, and RMSE, as presented in Table 8.

2.9. Mechanics-inspired visualisation module

The final part of the framework is the visualisation module, which transforms the nodal fields predicted by the CatBoost into mechanics-informed spatial visualisation. This is done by dynamically scaling the predicted nodal stress, strain and displacement magnitudes using the axial stress-strain curves predicted by the CATO-LSTMO or CATO-MZW in Dada et al. (2024).

In principle, the axial stress and strain values of each frame index (0–20) are obtained from the ML-predicted stress-strain curve. The predicted nodal stress, strain and displacement are first normalised (relative to their respective maximum values) and then scaled by the axial stress or corresponding strain value of the specific frame. This scaling process ensures that the evolution of the field is consistent with the material response. This also allows the model to approximate the contours realistically without relying on iterative solvers or complex constitutive laws.

Furthermore, the three-dimensional geometry of the FRCRAC is reconstructed using the 620-node cylindrical mesh and its associated triangular elements in the Python library Plotly. Each node is assigned a dynamically scaled value for stress, strain or displacement, with the resulting field rendered using Mesh3D and Scatter functions in Plotly. A colour gradient similar to the Abaqus visualisation style is used for the contour plots. This module bridges the gap between data-driven predictions and physically interpretable responses. While it does not replace full FE solvers, it provides a computationally efficient, explainable and visually intuitive alternative for rapid assessment of FRCRAC behaviour under axial loading.

3. Measure of accuracy and efficiency

3.1. Measure of accuracy

The performance metrics for both the CATO and CATO-LSTMO frameworks are measured using the metrics in Table 9.

The R^2 reflects the goodness of fit, and the MAE measures the average error magnitude (in absolute terms) in the prediction set. RMSE is the square root of the average squared difference between the actual and predicted values. It indicates how much error the model will produce while predicting, with higher weights generally assigned for larger errors. MAPE measures the average percentage error (in absolute terms) between the predicted and actual values.

3.2. The measure of computational efficiency

A benchmark comparison was conducted against the conventional FE method (using Abaqus) to evaluate the computational efficiency of the ML-MIVM framework. Both methods were tested under identical FRP-confined concrete configurations with consistent geometry, material properties, loading and boundary conditions. Each analysis was repeated five times to assess consistency and repeatability.

The total time to generate the complete set of 21 frame-wise outputs was measured for both Abaqus and the ML-MIVM framework. For Abaqus, the timing was recorded from the moment of job submission to the completion of the post-processing (when the visualisation outputs became available). For ML-MIVM, the timing was captured from the moment the prediction command "Predict" was selected to the final rendering of the visualisation. Also, both approaches were executed on the same computational hardware to ensure fair comparison.

The computational efficiency was quantified using Equation (18) represented as:

$$\text{Speed factor} \quad SF = \frac{T_{Abaqus}}{T_{ML-MIVM}} \tag{18}$$

where T_{Abaqus} and $T_{ML-MIVM}$ are the computational time (in seconds) for Abaqus and the ML-MIVM framework, respectively.

Table 10
Hyperparameters tuned by Optuna for CATO.

Target	Hyperparameters					
	Learning rate	Depth	L2 regulation	Bagging temperature	Border count	iterations
f_{cu}	0.035	7	0.0010	0.0008	145	437
ε_{cu}	0.270	5	6.7072	0.0003	133	495
$\varepsilon_{h,rup}$	0.085	5	0.0054	0.0042	237	261

Table 11
Hyperparameters tuned by Optuna for LSTMO.

Target	Hyperparameters			
	Units	Dropout	Epoch	Batch size
Axial ($f_c, \varepsilon_{c,a}$)	100	0.390	87	23
Hoop ($f_c, \varepsilon_{c,h}$)	84	0.112	67	16

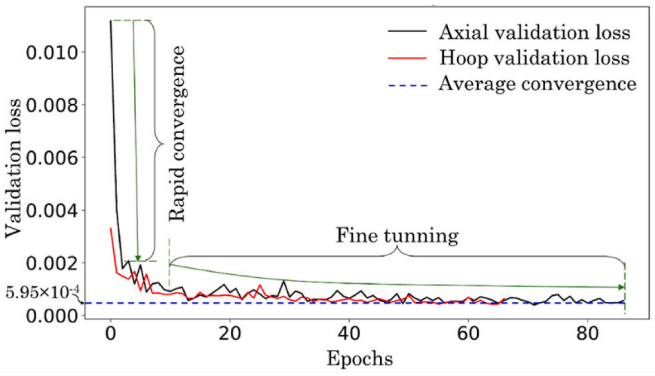

Fig. 10. The validation loss trend with epoch for axial and hoop conditions for LSTMO.

4. Results and discussions

4.1. Hyperparameters and model training

The hyperparameters of the CatBoost and LSTM algorithms for both the axial and hoop datasets were tuned with Optuna, and the results are presented in Tables 10 and 11.

Furthermore, the result of the tuned LSTM (LSTMO), trained via ten-fold cross-validation, is presented in Fig. 10. The plot shows the trend of the validation loss with increasing epochs for both the axial and hoop cases. As observed, the initial stage experienced a rapid convergence (drop) in validation loss, followed by a fine-tuning section with gradual convergence. The average convergence validation loss was 5.95×10^{-4}, and a similar trend was observed for both hoop and axial cases.

It is noteworthy that the axial trend has a higher initial validation loss and a larger final number of epochs compared to the hoop trend.

4.2. CATO prediction of the ultimate conditions of FRCRAC

The performance of the CATO in predicting the ultimate strength (f_{cu}), axial strain (ε_{cu}) and hoop strain ($\varepsilon_{h,rup}$) are presented in Table 12. The ultimate hoop strain in this study is also the rupture strain of the FRCRAC because all the specimens considered experienced post-peak hardening and failed by rupture. The result in Table 11 indicates that CATO performed excellently in predicting the ultimate strength with a testing R^2, MAE, RMSE and MAPE of 96.10 %, 2.578 MPa, 4.755 MPa and 3.096 %, respectively. Furthermore, for the ultimate strain, CATO achieved a testing R^2, MAE, RMSE and MAPE of 93.58 %, 0.121×10^{-2}, 0.172×10^{-2} and 7.40 %, respectively. This is consistent with the earlier result reported by Dada et al. (2024). For the ultimate hoop strain (rupture strain), CATO predicted well, with a testing R^2, MAE, RMSE and MAPE of 84.11 %, 0.071×10^{-2}, 0.100×10^{-2} and 5.02 %, respectively.

The regression plots for the ultimate strength, axial and hoop strain values are presented in Fig. 11. For strength, almost all the predicted points were within an identity error limit of ±10 %. Also, the predicted values for the ultimate axial and hoop strain were within the identity error limit of ±20 %.

4.3. Performance of CATO-LSTMO for predicting the stress-strain curves of FRCRAC

After the successful predictions of the ultimate conditions using CATO, the predicted values were integrated into the LSTMO to form the CATO-LSTMO framework. This CATO-LSTMO framework is used to predict the stress-strain curves of FRCRAC, with the plots of the stress-strain curves varied for percentage RA replacement, types of aggregates (NA, RCA, RCL, and RBA), FRP thickness and different unconfined strength. The results were compared with the experimental values, which are presented in Figs. 12–14.

Each of the 25 points for the curves predicted by the CATO-LSTMO framework is determined by a pair of stress and strain for each point. The coordinates of the predicted stress-strain points are compared with points extracted from the experimental data using the R^2, MAE and RMSE metrics. The average performances of the 25 stress-strain points for the training, validation and testing datasets are presented in Table 13. The results show a testing R^2, MAE and RMSE of 98.83 %, 1.559 and 1.134, respectively, for the axial curves. Also, a testing R^2, MAE and RMSE of 98.51 %, 1.220 and 1.948, respectively, was achieved for the hoop curves. A close agreement between the metrics of the training, validation and testing sets was also observed, which implies robustness and generalisation of the model over unseen data.

The performance of the stress-strain curves predicted by the CATO-LSTMO model is of high accuracy and agreement with the experimental curves. The CATO-LSTMO model also captures with high accuracy the influence of variation in FRP thickness, RA content and type. Figs. 12–14 show a significant increase in confinement with increasing thickness of FRP, regardless of the FRP type. Also, as evidently shown in Fig. 14, the ultimate strength reduces with increasing content of RA (increased RA reduces unconfined strength). However, it should be noted that the change in confinement due to FRP thickness is more significant than the one observed due to percentage RA content. These results are consistent with the experimental results.

Figs. 12–15 show that CATO-LSTMO predictions agree with the experimental curves.

4.4. Performance of CATO-LSTMO for predicting the ultimate conditions of FRCRAC

The ultimate conditions, including the ultimate strength, axial strain and hoop strain values for the predicted, were compared with the experimental. The ultimate conditions of the CATO-LSTMO were obtained by obtaining the last predicted point (25th point) of each sample.

Table 12
Performance of CATO for ultimate strength, axial and hoop strain.

Datasets	f_{cu}				ε_{cu}				$\varepsilon_{h,rup}$			
	R^2 (%)	MAE (MPa)	RMSE (MPa)	MAPE (%)	R^2 (%)	MAE (× 10^{-2})	RMSE (× 10^{-2})	MAPE (%)	R^2 (%)	MAE (× 10^{-2})	RMSE (× 10^{-2})	MAPE (%)
Training	99.80	0.782	1.033	1.058	99.20	0.035	0.054	2.249	95.00	0.045	0.059	3.536
Validation	98.24	2.381	3.156	2.962	91.29	0.125	0.165	7.577	86.90	0.066	0.092	5.120
Testing	96.10	2.578	4.755	3.096	93.58	0.121	0.172	7.402	84.11	0.071	0.100	5.021
Data	98.95	1.333	2.394	1.708	96.33	0.086	0.120	5.375	92.45	0.053	0.073	4.077

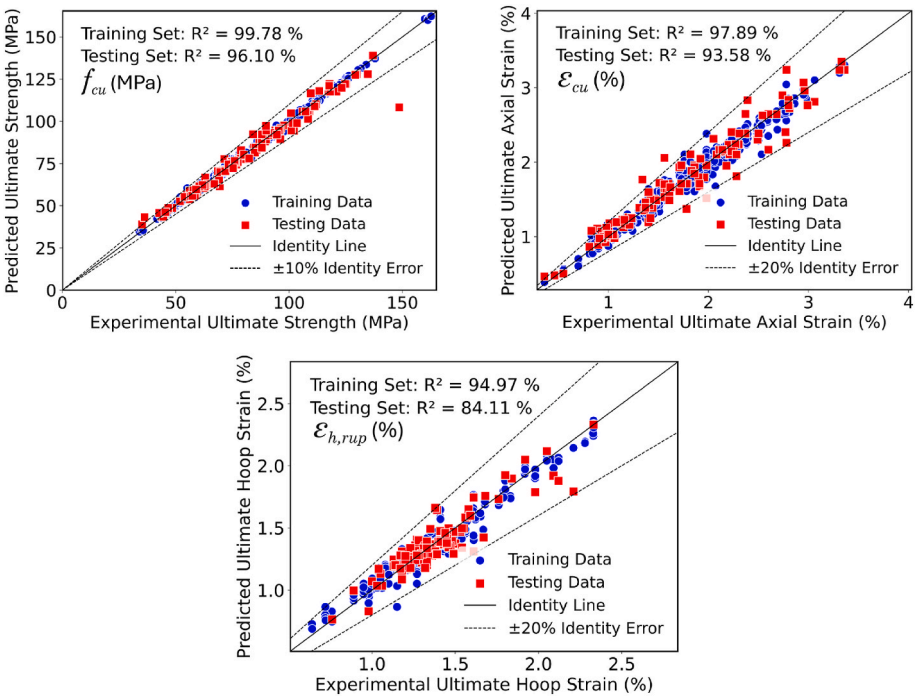

Fig. 11. The regression plots of CATO for ultimate strength, axial and hoop strain.

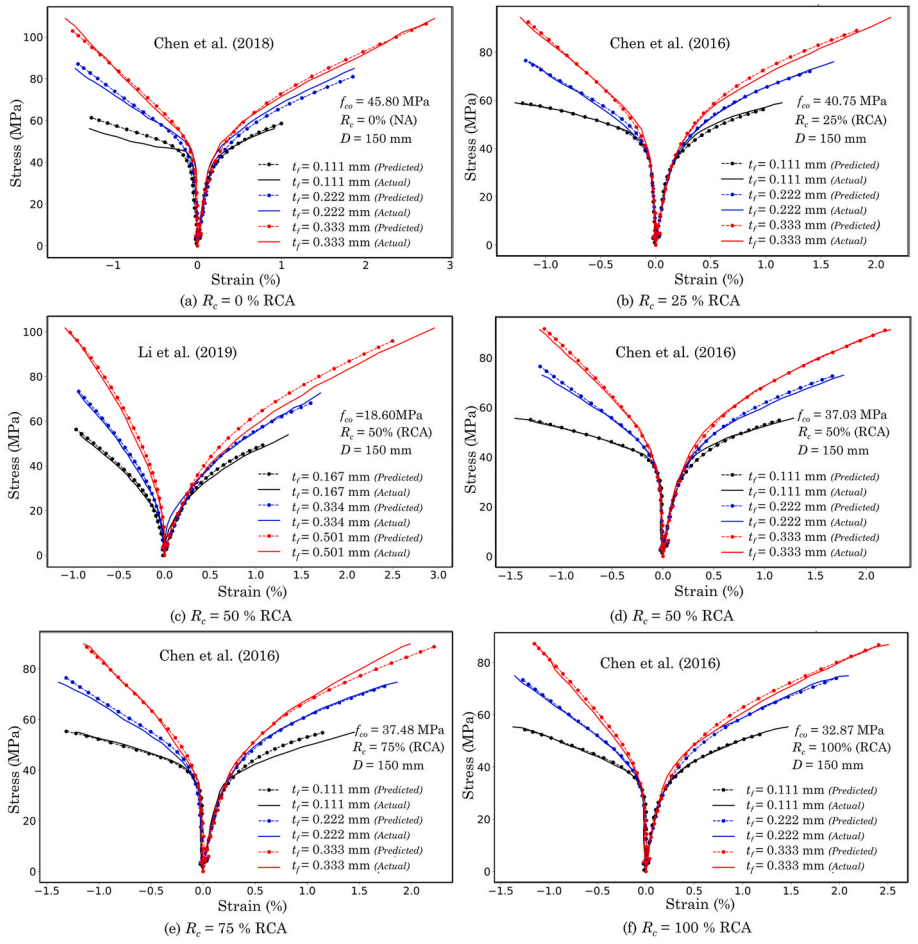

Fig. 12. Predicted and experimental stress-strain curves for RCA.

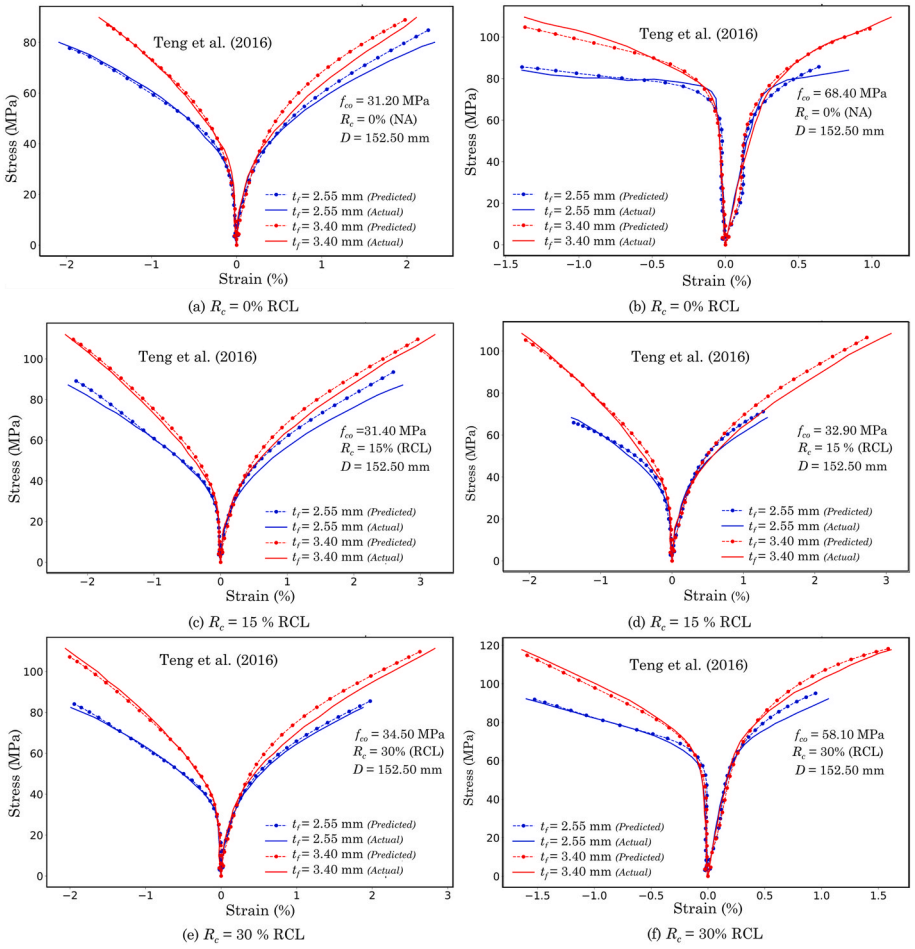

Fig. 13. Predicted and experimental stress-strain curves for RCL.

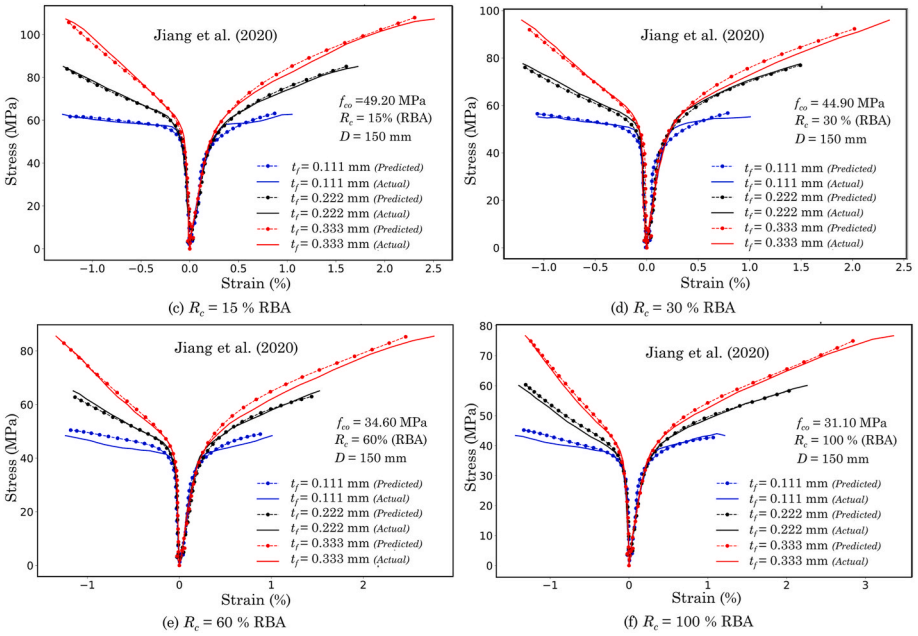

Fig. 14. Predicted and experimental stress-strain curves for RBA.

Table 13
CATO-LSTMO performance for average stress-strain points.

Datasets	Axial			Hoop		
	R^2 (%)	MAE	RMSE	R^2 (%)	MAE	RMSE
Training	99.05	0.984	1.277	99.19	0.989	1.282
Validation	98.61	1.021	1.393	98.80	0.932	1.212
Testing	98.83	1.559	1.134	98.52	1.220	1.948

The performance of CATO-LSTMO to predict these ultimate conditions was evaluated using the R^2, MAE, RMSE and MAPE metrics.

The results presented in Table 14 show high predictive performance for the training, validation, and entire datasets, with the ultimate strength attaining a testing R^2, MAE, RMSE and MAPE of 97.63 %, 2.90 MPa, 3.96 MPa and 3.42 %, respectively. Also, the CATO-LSTMO achieved a testing R^2, MAE, RMSE and MAPE of 91.08 %, 0.144×10^{-2}, 0.172×10^{-2} and 8.12 %, respectively, for the ultimate axial strain prediction. A testing R^2, MAE, RMSE and MAPE of 93.92 %, 0.048×10^{-2}, 3.957×10^{-2} and 3.45 %, respectively, was also attained for ultimate hoop strain prediction. These results show higher CATO-LSTMO performance and robustness in the prediction of ultimate strength compared to the ultimate strain conditions, though CATO-LSTMO performed better for hoop strain than axial strain.

It is also worth noting that CATO-LSTMO performed better than CATO in terms of robustness. This is observed in the closeness between the training and testing metrics. In particular, there is a significant improvement in the accuracy and robustness of CATO-LSTMO in predicting the ultimate hoop strain. This improved robustness is because LSTM helps to smooth the variability in the data, which helps to predict well on unseen data. Furthermore, the CATO-LSTMO benefits from the capability of LSTM to model the progression of the stress-strain curve, which provides a more accurate final prediction for both ultimate axial and hoop conditions. The regression plots comparing the predicted and experimental ultimate conditions are presented in Fig. 16.

4.5. Comparative study of CATO-LSTMO in predicting FRCRAC ultimate conditions

The CATO-LSTMO was compared to AdaBoosting (ADB), Support Vector Regressor (SVR), Artificial Neural Network (ANN) and the traditional Recurrent Neural Networks (RNN) in predicting the ultimate conditions of the FRCRAC. The results, as presented in Table 15, show that the metrics of CATO-LSTMO presented in Table 13 outperform the results of the models in Table 15. The CATO-LSTMO consistently show the highest value for R^2 and the lowest values for MAE, RMSE and MAPE for the ultimate conditions. The outlier was the slight underperformance of CATO-LSTMO for hoop strain predictions compared to ADB. It must also be noted that the MAPE result for RNN was outrageously high because of its sensitivity and instability after de-normalisation.

The performance metrics for both CATO-LSTMO and other ML models are presented in the bar charts in Fig. 17. The higher bars for R^2 and lower bars for the error metrics, MAE, RMSE and MAPE, imply high performance.

4.6. Comparative study of CATO-LSTMO in predicting the stress-strain curve of FRCRAC

The performance of CATO-LSTMO in predicting the stress-strain curve was compared to the experiment stress-strain curves and predictions by Teng et al. (2009) and the CATO-MZW model developed by Dada et al. (2024). The models were used to predict the stress-strain responses of FRCRAC containing NA, RCA, RCL and RBA at different percentage contents and varying levels of FRP thickness. The experimental specimens considered in the comparative study were obtained from the study of Teng et al. (2016), Chen et al. (2016) and Jiang et al. (2020). The plots of the curves are presented in Fig. 18.

From Fig. 18, it is evident that the CATO-LSTMO model performed best, having the predictions closest to the experimental curves for all types of RA and thicknesses of FRP. The next is the hybrid model, CATO-MZW, which performs satisfactorily for the majority of the predictions. Moreover, an overestimation of stress was observed, which makes it less reliable compared to CATO-LSTMO. The empirical model of Teng et al. (2009) performs the least, with huge divergence at the second branch of the curve for the majority of the tests. It performed significantly worse in the prediction of FRCRAC containing RBA. However, it is worth noting that the model of Teng et al. (2009) was initially developed for NA. It was considered because many existing studies have adopted it in predicting the stress-strain curve of FRCRAC.

The predicted stress–strain curves demonstrate that the CATO-LSTMO framework effectively reproduces the rupture-controlled hardening behaviour of uniformly confined FRCRAC. However, as recent 3D strain-field investigations (Li and Wu, 2023) and eccentric-loading

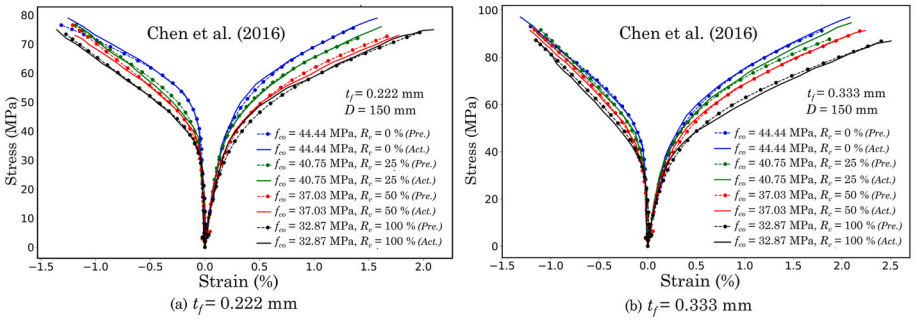

(a) t_f = 0.222 mm (b) t_f = 0.333 mm

Fig. 15. Variation of RCA content.

Table 14
The CATO-LSTMO performance in predicting the ultimate conditions.

Datasets	f_{cu}				ε_{cu}				ε_{cu}			
	R^2 (%)	MAE (MPa)	RMSE (MPa)	MAPE (%)	R^2 (%)	MAE ($\times 10^{-2}$)	RMSE ($\times 10^{-2}$)	MAPE (%)	R^2 (%)	MAE ($\times 10^{-2}$)	RMSE ($\times 10^{-2}$)	MAPE (%)
Training	97.66	2.761	3.534	3.766	93.73	0.124	0.159	7.562	94.99	0.043	0.058	3.228
Validation	97.84	2.737	3.361	3.897	92.11	0.131	0.168	8.092	92.29	0.048	0.070	3.608
Testing	97.63	2.897	3.957	3.422	91.08	0.144	0.172	8.121	93.92	0.048	0.066	3.449
Data	97.68	2.772	3.562	3.745	93.38	0.126	0.161	7.671	94.64	0.044	0.060	3.288

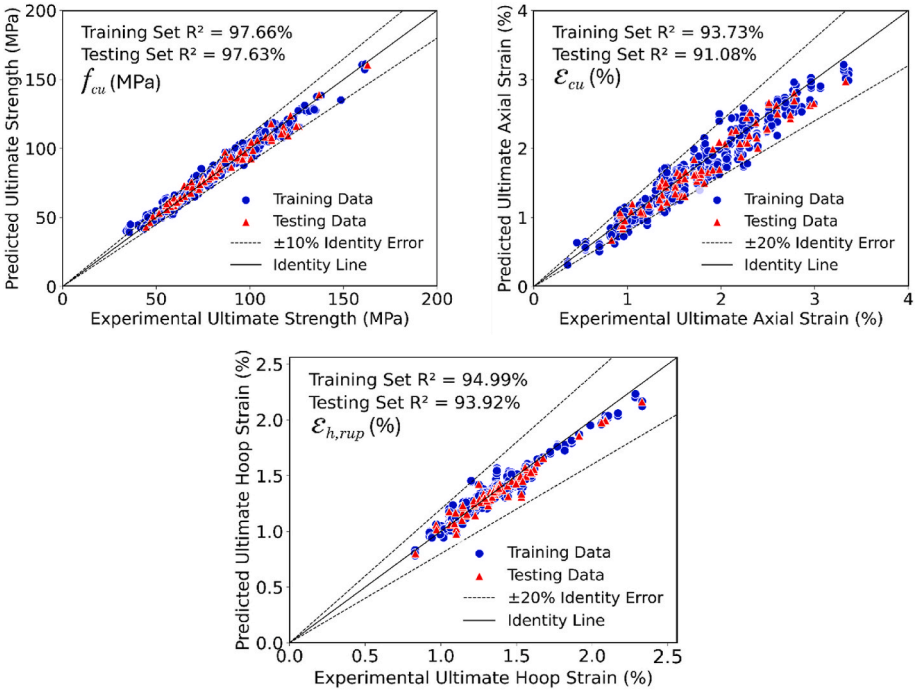

Fig. 16. Regression plots for LSTM performance for predicting ultimate conditions.

analyses (Wu et al., 2025) highlight, practical confinement conditions are rarely uniform. Spatial variations in confinement efficiency, caused by cross-sectional geometry, aggregate heterogeneity, and load eccentricity, lead to heterogeneous stress redistribution and localised volumetric-strain evolution within the concrete core. These non-uniform mechanisms govern the transition from uniform dilation to localised cracking, which in turn produces anisotropic deformation and strain-softening beyond peak load.

Li and Wu (2023) used full-field 3D evidence to demonstrate that strong confinement gradients are developed in FRP-confined square and rectangular columns. This causes crack networks to concentrate near the corners due to weak lateral restraints, while the interior of the columns is relatively intact. Furthermore, Wu et al. (2025) demonstrated that eccentric loading amplifies this non-uniform confinement, producing asymmetric stress-strain responses and progressive stiffness degradation on the tension side. Together, these studies clarify that the post-peak softening and anisotropic behaviour of FRP-confined concrete are rooted in measurable variations of confinement pressure, volumetric-strain evolution, and stress redistribution factors that cannot be inferred purely from global stress-strain data.

Recognising these mechanisms establishes a clear pathway toward a hybrid, mechanism-informed learning framework. Future extensions of CATO-LSTMO could incorporate confinement-related indicators (such as confinement index, lateral-to-axial stress ratio, and volumetric-strain trajectory) as physics-aware input features or as regularisation constraints in the training process. Integrating these mechanistic parameters enables the framework to learn physically consistent stress-strain responses under both uniform and non-uniform confinement, thereby enhancing its robustness across diverse geometries and loading conditions while maintaining solver-free computational efficiency.

Table 15
Performance of other base ML models in predicting the ultimate conditions.

Model	Datasets	f_{cu}				ε_{cu}				$\varepsilon_{h,rup}$			
		R^2 (%)	MAE (MPa)	RMSE (MPa)	MAPE (%)	R^2 (%)	MAE ($\times 10^{-2}$)	RMSE ($\times 10^{-2}$)	MAPE (%)	R^2 (%)	MAE ($\times 10^{-2}$)	RMSE ($\times 10^{-2}$)	MAPE (%)
ADB	Training	90.40	5.794	7.151	7.652	86.42	0.002	0.002	13.631	94.96	0.048	0.059	3.814
	Validation	88.51	5.853	7.752	7.715	83.77	0.200	0.241	13.590	93.08	0.051	0.066	4.019
	Testing	91.78	5.885	7.371	7.360	81.40	0.197	0.248	12.690	95.24	0.046	0.058	3.499
	Data	90.44	5.809	7.236	7.629	85.79	0.196	0.237	13.532	94.83	0.048	0.059	3.803
SVR	Training	80.12	8.862	10.292	12.668	88.59	0.186	0.215	13.259	75.74	0.106	0.128	8.297
	Validation	81.49	8.326	9.837	12.171	84.29	0.211	0.237	14.148	77.80	0.096	0.119	7.409
	Testing	84.55	8.543	10.103	11.000	84.68	0.187	0.225	12.093	75.43	0.109	0.132	7.969
	Data	80.89	8.776	10.228	12.450	87.90	0.189	0.218	13.230	75.96	0.105	0.128	8.175
ANN	Training	95.10	3.967	5.111	5.387	94.25	0.117	0.153	7.682	92.05	0.056	0.074	4.278
	Validation	86.52	5.892	8.395	7.913	87.43	0.167	0.212	11.122	81.90	0.076	0.107	5.868
	Testing	90.45	5.301	7.946	6.836	87.07	0.146	0.207	9.137	83.61	0.077	0.108	5.771
	Data	93.74	4.293	5.853	5.785	93.04	0.125	0.166	8.171	90.25	0.060	0.081	4.587
RNN	Training	93.90	4.350	5.700	34.679	91.97	0.140	0.180	49.564	91.71	0.057	0.075	20.704
	Validation	77.41	7.256	10.869	33.579	80.00	0.205	0.268	44.921	77.83	0.085	0.119	20.420
	Testing	84.56	6.524	10.101	35.732	82.52	0.193	0.240	41.680	80.01	0.083	0.119	22.021
	Data	91.23	4.859	6.929	34.734	90.11	0.152	0.197	48.418	89.22	0.062	0.086	20.838

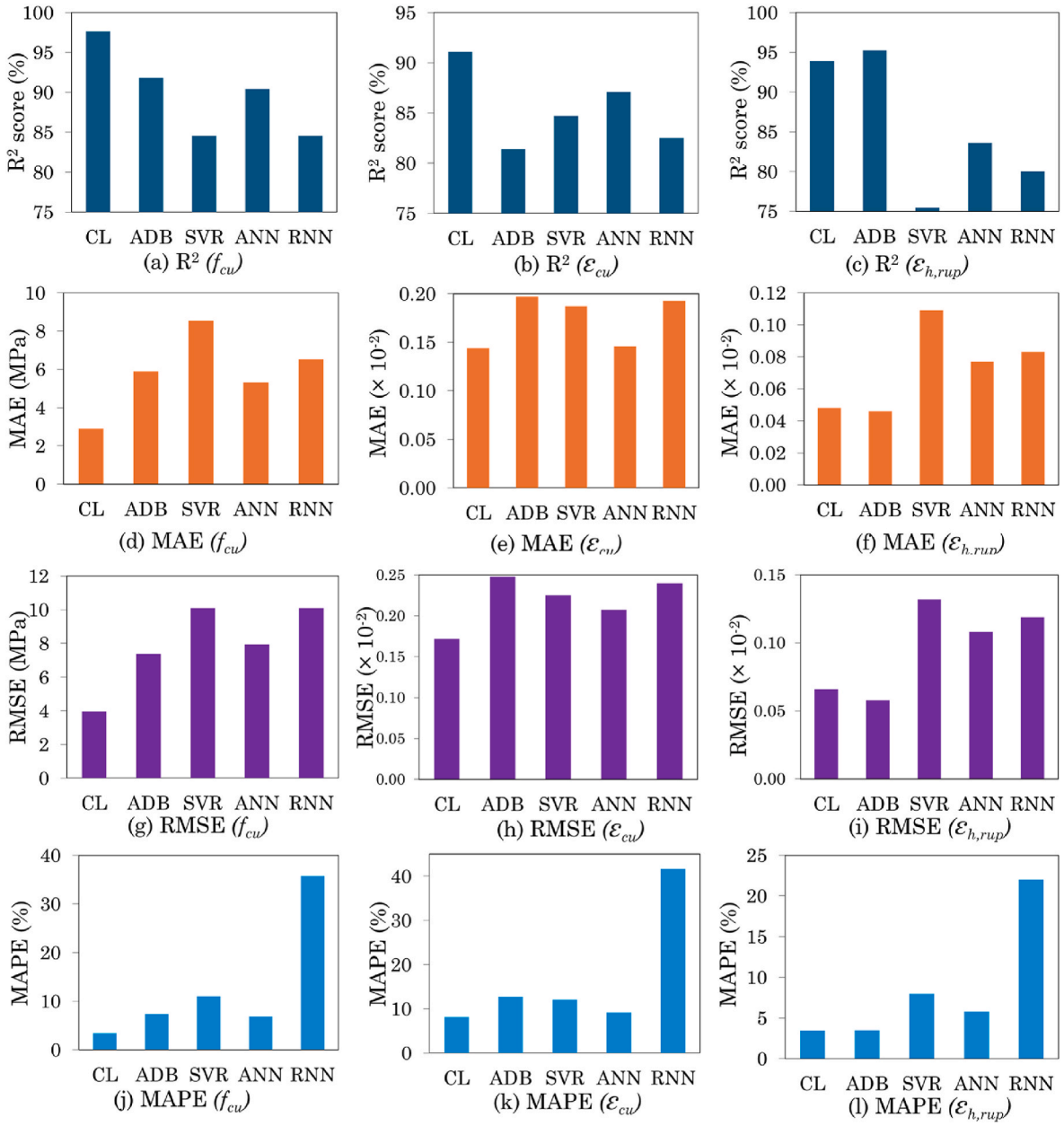

Fig. 17. Performance metrics of the ML predictions for f_{cu}, ε_{cu} and $\varepsilon_{h,rup}$. CL represents CATO-LSTMO.

4.7. Performance and interpretation of ML-MIVM

The CatBoost regression models for visualisation, trained on the nodal outputs from Abaqus, demonstrated high predictive performance for stress, strain and displacement across all dataset partitions. For the stress prediction, the model attained R^2 values of 99.952 % for training, 99.950 % for validation, and 99.953 % for testing, indicating accuracy and generalisability. Similarly, the strain model performed excellently with R^2 values of 99.948 % for training, 99.945 % for validation, and 99.948 % for testing, capturing the deformation characteristics. The displacement model achieved the highest performance with R^2 values of 99.987 % across the training, validation and testing sets, confirming accuracy and stability. These results suggest that the CatBoost models are robust and able to predict the distributions of the field outputs of the FRCRAC.

The result of the contour visualisation for the ML-MIVM framework is presented in the section in Figs. 19–21. The performances of the stress, strain and displacement contours are further discussed in consonance with the fundamental principles and experimental outputs.

4.7.1. Stress visualisation

Fig. 19 shows the stress contour visualisation depicting the progressive development of the stresses within the confined FRCRAC. Frame 0 shows zero stress values at the start of the simulation without any load. As the loading progresses, as presented in Frames 1–5, stress concentrations become evident around the circumference, indicating the mechanism between the concrete dilation and the FRP confinement. At Frame 20, high-stress values approaching the ultimate stress magnitude are observed to be concentrated around the mid-height of the specimen. This stress evolution highlights the capability of ML-MIVM to visualise the stress redistribution mechanism in FRCRAC accurately.

4.7.2. Strain visualisation

Similar to the results of the stress contours, the strain contour evolution also shows the ML-MIVM capability to visualise the inelastic deformation. Negligible strain values were observed at the start of the

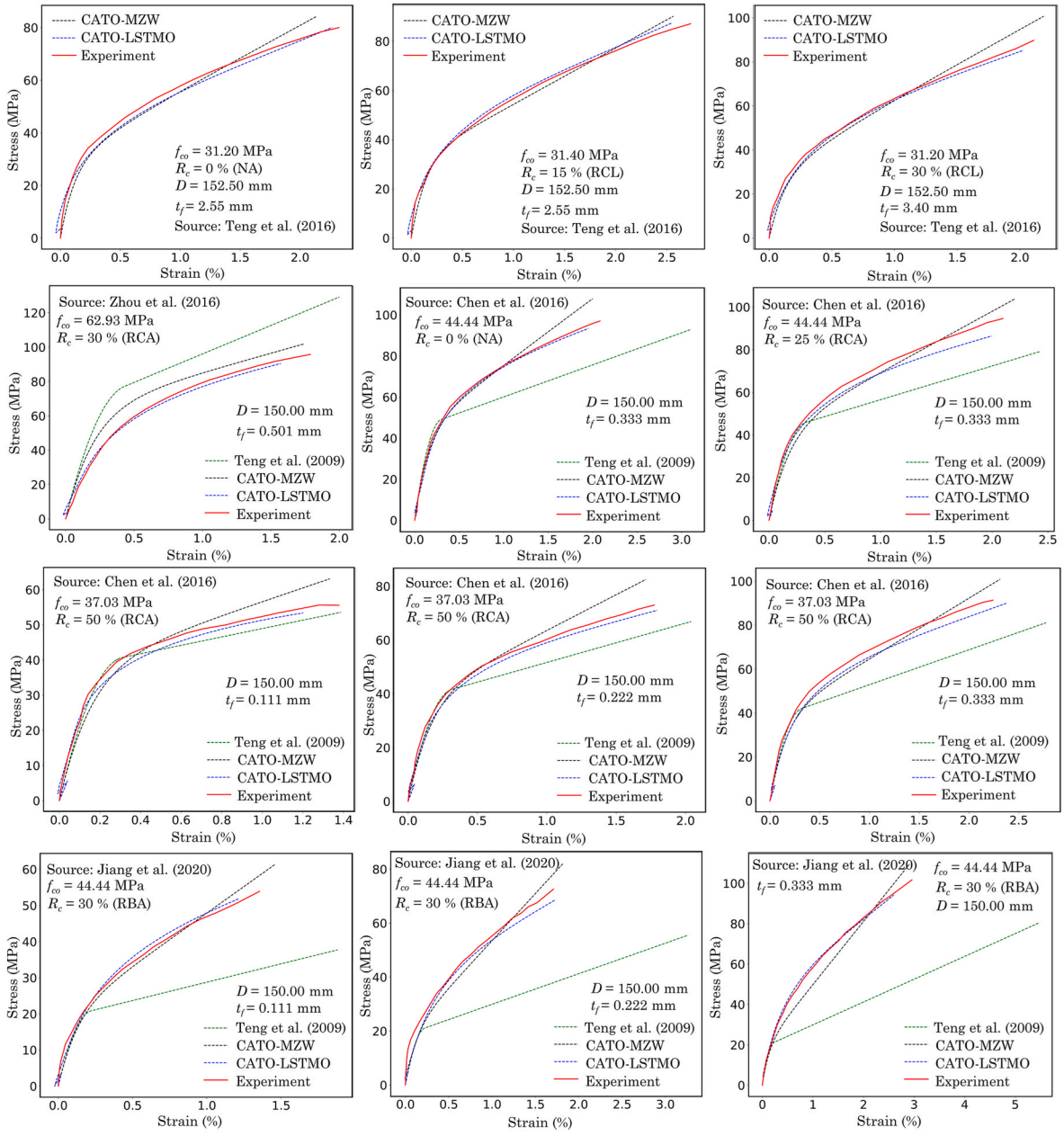

Fig. 18. Comparison of CATO-LSTMO with the experiment (Teng et al., 2009) and CATO-MZW.

simulation, as shown in Frames 0 and 1 of Fig. 20. The evolution became pronounced as the loading progressed with bands of localised strain along the height of the specimen, as shown in Frames 3–5. The higher strain values in these frames also indicate crack initiation and lateral expansion confined by the FRP. By Frame 20, the ultimate strain level was achieved at mid-height, with the distribution indicating the interaction between the concrete dilation and FRP tensile engagement. The similarity between the stress and strain contours also implies a positive relationship between the two fields, though non-linear. This agrees with the mechanism and experimental observation of FRP-confined concrete. The smooth progression of these contours across frames validates the capability of ML-MIVM in visualising the strain-hardening behaviour and ductility enhancement of FRP-confined concrete.

4.7.3. Displacement visualisation

The displacement contours show the global deformation behaviour of the FRCRAC under axial compression, as presented in Fig. 21. While the initial Frame 0 exhibits no displacement when no load is applied, the subsequent frames reveal progressive axial shortening. As the loading progressed, the base experienced no displacement, as expected for fixed support, while the top experienced the maximum displacement. From Frames 3–20, the displacement distribution remains very similar, with the only variation being the magnitude of the displacement as the loading progresses. The ML-MIVM successfully captures the displacement behaviour of FRCRAC, and the contours align with physics-based mechanism and experimental observation.

Summarily, the model captures the stress, strain and displacement fields with a high degree of accuracy in alignment with the physical behaviour of FRCRAC. The framewise evolution also highlights the gradual redistribution of the internal fields from the elastic to inelastic zones.

4.8. Comparing MIVM with Abaqus visualisation and efficiency

4.8.1. Visualisation

To further assess the visualisation ability of the ML-MIVM

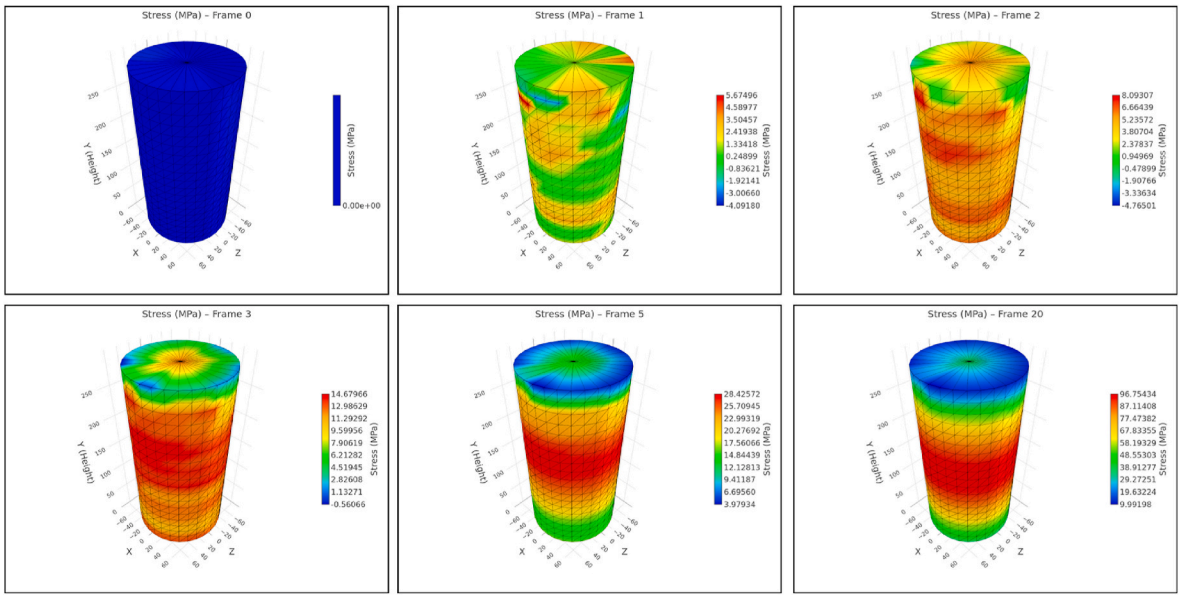

Fig. 19. The stress contours visualisation output of the ML-MIVM for selected frames.

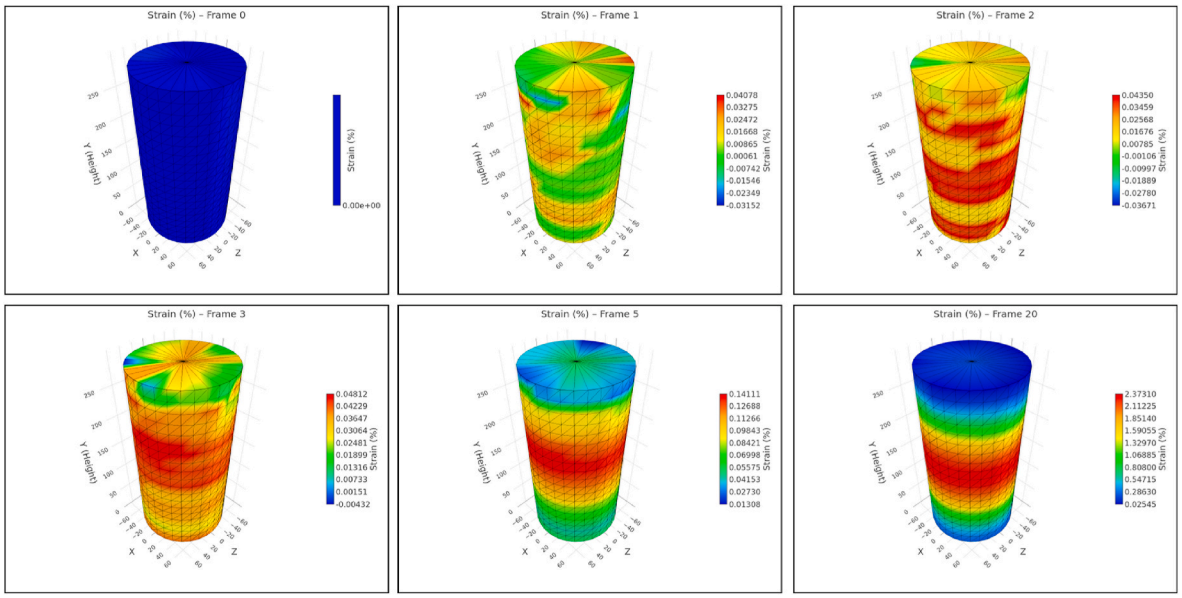

Fig. 20. The strain contour visualisation of the MIVM for selected frames.

framework, the displacement result for FRCRAC is compared with the output of a well-established commercial FE software, Abaqus. The quick analysis in Abaqus was carried out using the same loading, material inputs and boundary conditions. The displacement contours and values from both models in Fig. 22 (a) and (b) show similar profiles.

The minimum displacement was at the fixed base for both models, and the maximum was at the free top end where the load was applied. The similarity in the pattern and values of the displacement confirms the reliability of ML-MIVM in visualising the fields of FRCRAC. In addition to the qualitative contour comparison, a node-by-node quantitative assessment was performed between ML-MIVM predictions and Abaqus results for the displacement visualisation. The analysis shows an average R^2 value of 0.95, MAE of 0.28 mm and RMSE of 0.44 mm across all nodal instances. The high coefficient of determination and low error demonstrate that ML-MIVM not only replicate global displacement profiles but also agrees well quantitatively with the finite element outputs at the nodal level.

4.8.2. *Efficiency*

The computational efficiency of the ML-MIVM framework was benchmarked against the conventional Abaqus FE simulation. Table 16 and Fig. 23 summarise the timing results from five repeated runs of identical displacement-controlled loading scenarios for both methods.

On average, Abaqus required approximately 35 min to complete a full simulation for a test case, while ML-MIVM delivered equivalent results in just 4.29 s. This implies that the ML-MIVM is 518 times faster than Abaqus on average, highlighting the rapid prediction and visualisation.

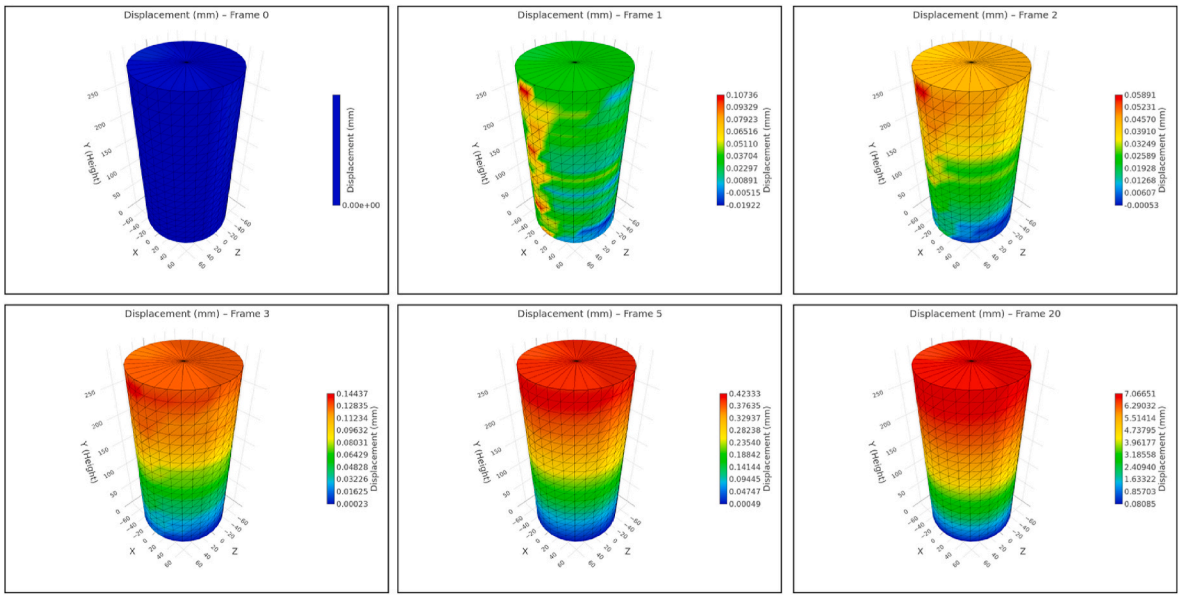

Fig. 21. The displacement contour visualisation output of the MIVM for selected frames.

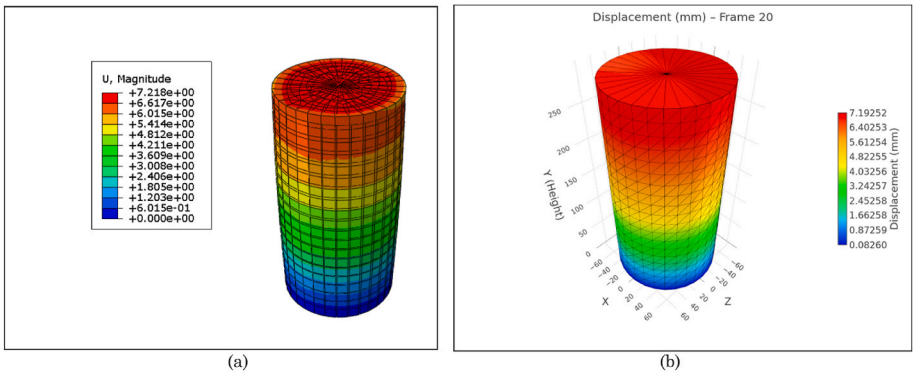

(a) (b)

Fig. 22. Displacement contours (a) Abaqus output (b) ML-MIVM output.

Table 16
The computational efficiency of Abaqus and ML-MIVM.

Method	Iteration time (seconds)					Mean	Std.
	1	2	3	4	5		
Abaqus	2293.16	2295.80	2073.90	2268.08	2197.64	2225.72	93.66
ML-MIVM	04.14	04.10	04.32	04.54	04.33	4.29	0.18

4.9. Advantages of the MIVM visualisation module

The ML-MIVM framework offers some key advantages when compared to traditional finite element analysis (such as Abaqus) and experimental approaches. These merits relate to computational efficiency and modelling flexibility, as discussed in the following subsections.

- *Computational efficiency:* The deployed ML-MIVM framework enables a near-instantaneous prediction of the stress-strain responses and field visualisations of FRCRAC. This significantly reduces the computational time compared to the conventional FE approach, which requires significant time for iterative solver convergence, especially when performing nonlinear analysis.
- *Material calibration:* While conventional FE modelling requires detailed calibration of material properties, including physical, elasto-plastic, damage and fracture properties, this is not required in the ML-MIVM framework. The calibration process could be tedious and prone to huge uncertainty in FE when dealing with materials like FRCRAC, compared to the ML-MIVM framework that simply learns from the ML-predicted stress-strain responses, thereby bypassing the need for explicit calibration of complex constitutive equations.
- *Data-driven governing behaviour:* Conventional FE analyses often rely on assumed constitutive models, which may not fully capture the complexity of FRCRAC. The ML-MIVM framework bypasses this limitation by using the ML-predicted stress-strain curve as the governing input, enabling it to adapt flexibly across varying material behaviour.

5. Interpretability of the CATO and CATO-LSTMO models

To understand the physical consistency of the CATO and CATO-

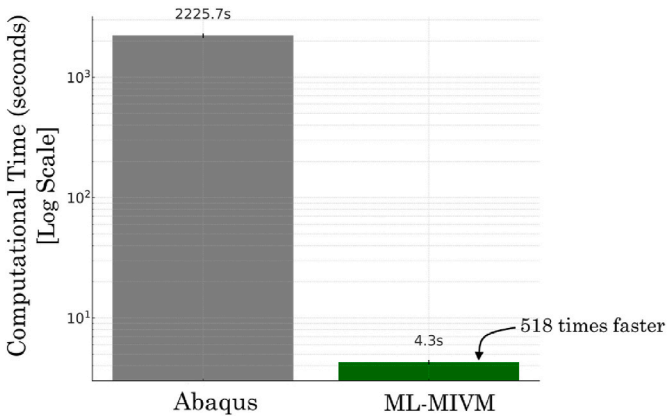

Fig. 23. Comparison of the computational time for Abaqus and ML-MIVM.

LSTMO models, their interpretability analyses are presented in this section. These models were interpreted using the SHapley Additive exPlanations (SHAP) feature importance for the CATO models (rupture strain, ultimate confined strength and confined strain) and the permutation feature importance for the CATO-LSTMO model as presented in Fig. 24.

For the rupture strain prediction, SHAP analysis in Fig. 24a shows that the FRP modulus, thickness and unconfined strain are the most influential parameters. This result reflects the dependence of the rupture strain on the FRP material properties and the strain capacity of the unconfined concrete. Other features, including the unconfined strength, RCA size and content, play the secondary role, highlighting the secondary influence that aggregate characteristics could have on the rupture behaviour.

As shown in Fig. 24b, the confining stress is the most important feature influencing the CATO model for the ultimate confined strength. This is secondarily followed by the overall thickness and unconfined strength of the FRP. The height and concrete modulus also have some influence, indicating that both confinement and unconfined concrete properties govern the prediction of FRCRAC. This is consistent with the classical theory of FRP-confined concrete stated earlier in the introduction section.

Similarly, for the CATO model predicting the ultimate confined strain, the SHAP analysis in Fig. 24c shows that the confining stress is the most influential variable. This is followed by the overall thickness of the FRP and the unconfined strength. This also aligns with the mechanics-based expectations, as higher confinement and stronger FRP jackets directly enhance strain capacity. Other variables include the concrete modulus, fibre modulus, and RCA content, which are consistent with their moderating roles in strain predictions.

Furthermore, the result of the permutation importance analysis for the CATO-LSTMO model in Fig. 24d shows that the ultimate confined strength and the confining stress are the two most significant influential parameters. These are followed by the FRP thickness and modulus. This ranking demonstrates that the sequence-based learning of the LSTM architecture significantly depends on the prediction of the CATO strength model. This strengthens the logic of the hybrid framework, where the CATO prediction strengthens the curve prediction accuracy by the LSTMO part. It is important to note that the influence of the ultimate confined strength in the curve prediction aligns with the logic of the analytical equations in Table 1 and hybrid analytical-ML models.

These interpretability results confirm that both the predictions of the CATO and CATO-LSTMO models are driven by variables that are significant to the FRCRAC behaviour. This consistency enhances the trustworthiness and interpretability of the proposed framework.

6. Deployment of the ML-MIVM framework

In this section, the integrated ML-MIVM framework is deployed online as an application software using Streamlit, with the graphical user interface (GUI) shown in Fig. 25. The application software is an interactive prediction and visualisation platform for investigating the behaviour of FRCRAC under axial compression.

The users can input a range of parameters, including aggregate type, aggregate replacement percentage, water-cement ratio, geometric dimensions (height and diameter), unconfined concrete strength and strain values, modulus and thickness of the FRP. Based on these inputs, the application predicts the ultimate axial strength, axial strain, and hoop strain using the CATO models that were developed earlier in the study.

Furthermore, the application generates the complete stress-strain curves based on the selected stress-strain model (CATO-MZW or

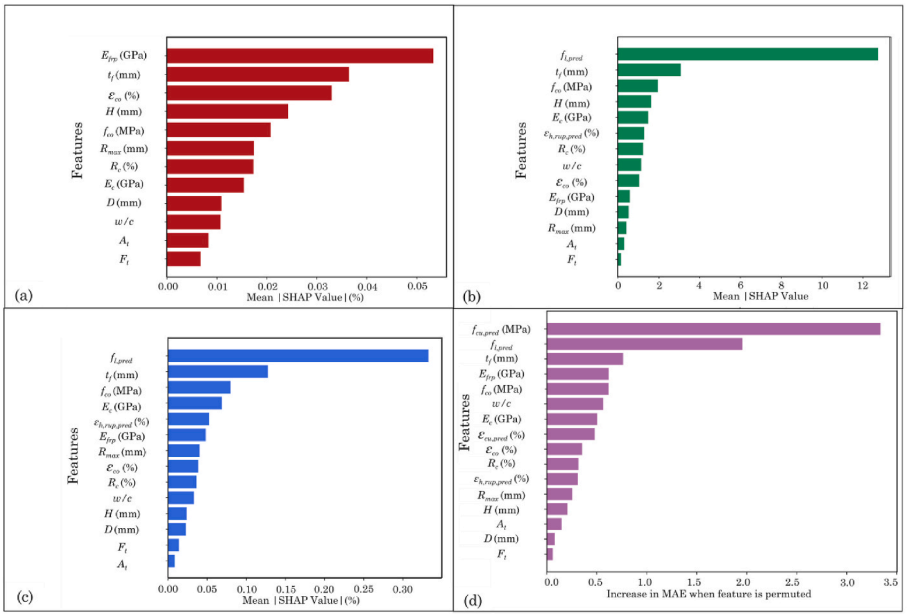

Fig. 24. Feature importance of (a) CATO predicting rupture strain prediction, (b) CATO predicting the ultimate strength, (c) CATO predicting the ultimate axial strain, (d) CATO-LSTMO predicting the stress-strain curves.

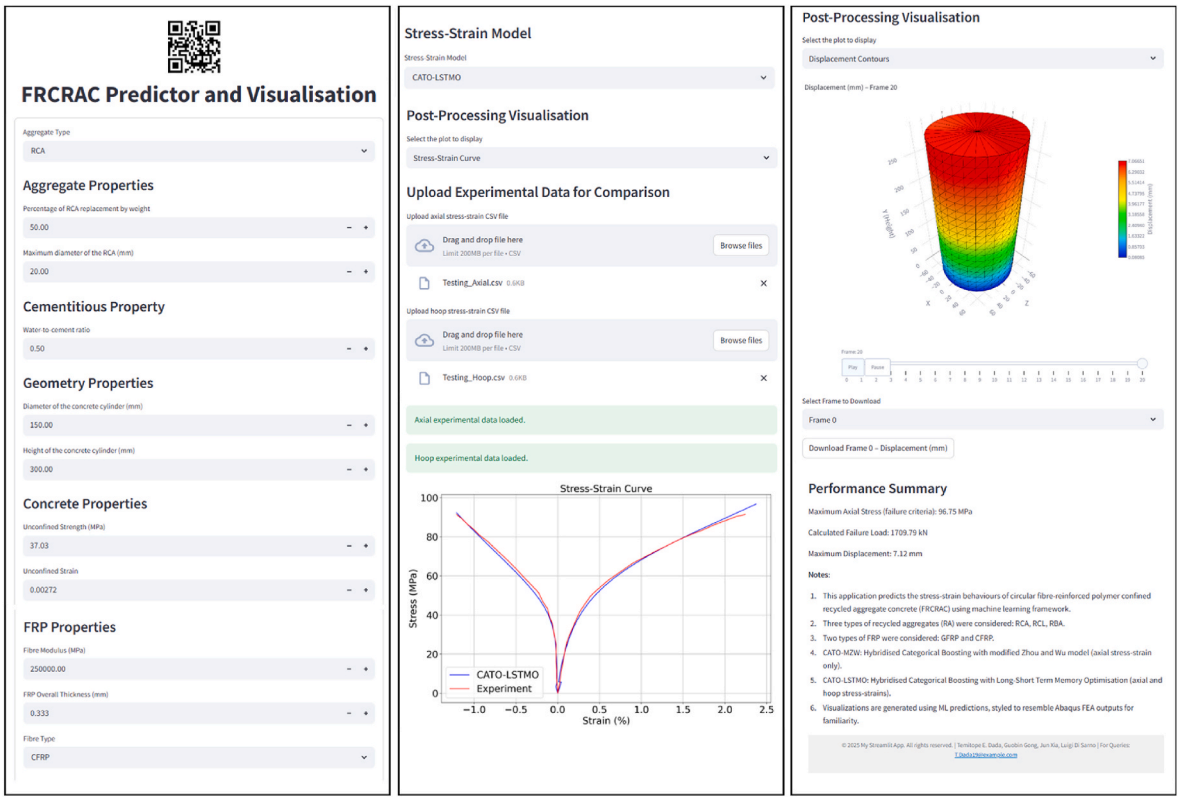

Fig. 25. The graphical user interface of the ML-MIVM model.

CATO-LSTMO) using either the ML-analytical (CATO-MZW) or sequence-based hybrid ML (CATO-LSTMO) models. For CAT-LSTMO, the application predicts both the axial and hoop stress-strain responses, while only the axial response is predicted in CATO-MZW. Meanwhile, users have the option to upload experimental data in the Comma-Separated Value (CSV) format, with the strain and stress titles in the first two columns of a spreadsheet. This helps to directly compare the ML predictions with the test results, which enables validation and performance benchmarking of the models.

The users can also visualise the contours of stress, strain, and displacement. The stress-strain curves, load-displacement curves, and field contours can be downloaded as images in the Portable Network Graphic (PNG) format, which enhances easy usage of the outputs. The model can be accessed using the QR code provided in Fig. 25 or via the URL https://frcrac.streamlit.app/.

7. Conclusions, limitations, and implications for construction practice

7.1. Conclusions

Despite the advancements in predicting the stress-strain behaviour of FRP-confined recycled aggregate concrete (FRCRAC), particularly through analytical and hybrid ML-analytical methods, challenges remain in achieving high predictive accuracy and efficiently generating interpretable structural insights. This study introduces a comprehensive hybrid ML framework enhanced by a mechanics-inspired post-processing visualisation module to predict and interpret the behaviour of FRCRAC under axial compression. A novel hybrid CatBoost-LSTM framework (integrating an Optuna-optimised Categorical Boosting model (CATO) and a Long Short-Term Memory Optimised model (LSTMO)) was developed to predict the complete axial and hoop stress-strain curves. To provide spatial interpretability, an auxiliary simulation-informed nodal-instance level dataset was generated using FE simulations. This enabled the training of CatBoost field models that reconstruct field-level stress, strain, and displacement contours scaled by the CATO-LSTMO output. This gives efficient predictions and visualisation, and enhances the interpretability of ML models. Based on the results, the following conclusions are drawn:

- The hybrid CATO-LSTMO framework accurately predicts the ultimate conditions and complete axial and hoop stress-strain response of FRCRAC, outperforming existing analytical and hybrid ML-analytical models across different types of FRP and RA. The model leverages both experimental and synthetic data, with all R^2 values exceeding 97 % accuracy.
- The simulation-informed visualisation module, built on simulation-informed nodal data, successfully translated the stress-strain responses predicted by CATO-LSTMO into field-level stress, strain, and displacement contours with frame-wise consistency and fidelity.
- The ML-MIVM visualisation framework significantly outperformed conventional FE solvers in computational efficiency, achieving a speed of over 500 times while delivering similar contour evolution.
- The framework successfully facilitated interpretable and scalable visualisation of field-level instances throughout the entire loading process. This enhances physical insights into the structural behaviour of FRCRAC.
- The deployed online application enables interactive prediction, comparison and visualisation, allowing users to input custom material parameters, select models and compare outputs with experimental data.

7.2. Limitations and future research

While the proposed CATO-LSTMO and ML-MIVM framework demonstrates high accuracy and strong spatial interpretability, a number of limitations are acknowledged. First, the predictive performances of the model were validated only within the parameter space of the recycled

aggregates (RA) and fibre-reinforced polymer (FRP) types considered in the datasets considered in the study. This may limit generalisability to entirely unseen material systems. Second, the framework is constrained to monotonic uniaxial compressive loading conditions and does not currently account for cyclic or multi-axial loading scenarios. Incorporating such conditions in future datasets would extend the applicability of the model to be more robust in different loading scenarios.

Third, because only specimens exhibiting strain-hardening were used during model training, the framework is currently limited to capturing hardening behaviour up to FRP rupture and may not generalise to strain-softening. Since post-peak softening significantly influences failure modes, ductility, and energy dissipation in FRP-confined concrete, the present FRCRAC framework may not accurately capture these behaviours. Future work will incorporate datasets with softening responses to extend the predictive capability of the CATO-LSTMO framework across a wider range of confinement conditions. Fourth, the present framework was developed for uniformly confined cylindrical specimens and may not directly apply to non-uniform confinement scenarios such as partial wrappings or non-cylindrical geometries. Such conditions often lead to pronounced post-peak strain-softening and anisotropic stress-strain responses, which this current framework does not capture. Extending the framework to handle non-uniform confinement is a key direction for future research.

From a modelling perspective, the current framework uses a single static-to-sequence LSTM architecture. More advanced approaches, such as physics-informed temporal convolutional networks or transformer architectures, may further enhance the long-term dependencies of the stress-strain curves. Finally, while the ML-MIVM visualisation module provides physically interpretable spatial contours of stress, strain and displacement, it operates without an iterative solver and, as such, might not capture localised damage like FE.

7.3. Broader implications for sustainable construction

The findings of this study have significant implications for advancing sustainability in the construction industry. The accurate prediction of the FRP-confined recycled aggregate concrete (FRCRAC) behaviour by the proposed framework directly supports the wider structural adoption of recycled aggregates. This ultimately helps in reducing sole reliance on natural aggregates and overall carbon emissions.

Furthermore, the CATO-LSTMO-MIVM framework advances the principle of a circular economy in construction. The reliable predictions of FRCRAC performance enable safer and greener structures while effectively reusing demolition waste as scale. This helps engineers to specify recycled materials with confidence and accelerate the adoption of low-carbon concrete solutions.

Also, combining ML accuracy with interpretable outputs provides the industry with a practical design tool. The framework allows rapid, data-driven decisions while reducing dependence on costly and power-intensive simulations. Finally, by lowering both financial and environmental costs, this framework makes advanced predictive capabilities more accessible for widespread adoption in practice.

CRediT authorship contribution statement

Temitope E. Dada: Writing – original draft, Software, Formal analysis, Data curation. **Guobin Gong:** Writing – review & editing, Supervision, Conceptualization. **Jun Xia:** Writing – review & editing, Supervision. **Luigi Di Sarno:** Writing – review & editing, Supervision.

Ethics approval and consent to participate

Not applicable.

Consent for publication

The authors give their consent for publication.

Funding

The financial support is supported by Xi'an Jiaotong-Liverpool University (RDF 18-01-23, PGRS, 1906002 and REF-20-01-01). This work is also supported by the PhD scholarship from the Nigerian Petroleum Technological Development Fund (PTDF) tenable at Xi'an Jiaotong-Liverpool University.

Declaration of competing interest

The authors declare that they have no known competing financial interests or personal relationships that could have appeared to influence the work reported in this paper.

Acknowledgements

The financial support by Xi'an Jiaotong-Liverpool University (RDF 18-01-23, PGRS 1906002 and REF-20-01-01) is gratefully acknowledged. This work is also supported by the PhD scholarship from the Nigerian Petroleum Technological Development Fund (PTDF) tenable at Xi'an Jiaotong-Liverpool University.

Appendix

Table A.1
The data summary for RCA

Literature/data properties			Aggregate/fresh concrete properties				Geometry		Unconfined concrete properties			FRP properties		Confined concrete properties		
Source	Year	No of Data	A_t	R_c (%)	R_{max} (mm)	w/c (%)	D (mm)	H (mm)	f_{co} (MPa)	ε_{co} (%)	E_c (GPa)	E_{frp} (GPa)	T_{frp} (mm)	f_{cu} (MPa)	ε_{cu} (%)	$\varepsilon_{h,rup}$ (%)
Zhao et al. (2014)	2014	18	NA, RCA	0–100	20	0.53	153	305	34.30–45.00	0.26–0.30	27.00–31.60	98.7	0.17–0.51	42.70–71.90	0.81–1.78	1.18–1.54
Teng et al. (2016)	2016	20	NA, RCL	0–30	70	0.45–0.46	152.5	305	31.20–68.40	0.19–0.25	–	78.8	2.55–3.40	68.30–123.30	0.83–3.33	1.38–2.33
Zhou et al. (2016)	2016	30	NA, RCA	0–100	31.5	0.30–0.45	150	300	37.82–75.39	0.20	30.30–33.00	272.73	0.17–0.50	55.09–134.76	0.82–2.25	1.10–1.49

(*continued on next page*)

Table A.1 (*continued*)

Literature/data properties			Aggregate/fresh concrete properties				Geometry		Unconfined concrete properties			FRP properties		Confined concrete properties		
Source	Year	No of Data	A_t	R_c (%)	R_{max} (mm)	w/c (%)	D (mm)	H (mm)	f_{co} (MPa)	ε_{co} (%)	E_c (GPa)	E_{frp} (GPa)	T_{frp} (mm)	f_{cu} (MPa)	ε_{cu} (%)	$\varepsilon_{h,rup}$ (%)
Chen et al. (2016)	2016	45	NA, RCA	0–100	20	0.5	150	300	32.87–44.44	0.27–0.35	22.27–26.96	250	0.11–0.33	54.99–97.04	1.08–2.78	1.04–1.61
Gao et al. (2016)	2016	9	NA, RBA	0–100	10	0.41	100	200	31.73–35.86	0.26–0.30	–	60.80–213.00	0.33–2.62	66.99–161.26	1.41–2.28	0.64–1.5
Xie and Ozbakkaloglu (2016)	2016	26	NA, RCA	0–100	12	0.37–0.62	152.5	305	39.50–78.40	0.19–0.28	23.40–34.60	76.00–236.00	0.11–0.42	48.40–96.60	1.09–1.88	0.94–1.86
Chen et al. (2018)	2018	18	NA, RCA	0–100	20	0.5	150–300	300–600	38.80–45.80	0.23–0.26	26.40–34.00	244	0.11–0.33	41.60–108.90	0.36–2.96	1.00–1.76
Li et al. (2019)	2019	10	NA, RCA	0–100	31.5	0.53	150	300	16.80–23.20	0.20	–	264	0.17–0.50	51.90–114.70	0.95–2.99	0.72–1.27
Jiang et al. (2020)	2020	44	NA, RBA	0–100	20	0.4	150	300	31.10–56.90	0.21–0.27	18.60–31.20	264	0.11–0.33	43.40–120.90	0.91–3.36	1.04–1.56
Zhou et al. (2021)	2021	24	NA, RCL	0–30	20	–	200	400	33.30–67.10	0.29–0.31	–	246	0.33–0.50	79.00–121.30	1.28–3.12	1.10–1.68

Table A.2
The test database for FRCRAC.

Data source properties		Aggregate/fresh concrete properties					Geometry		Unconfined concrete properties			FRP properties		Confined concrete properties		
Source	Year	No of Data	A_t	R_c (%)	R_{max} (mm)	w/c (%)	D (mm)	H (mm)	f_{co} (MPa)	ε_{co} (%)	E_c (GPa)	E_{frp} (GPa)	T_{frp} (mm)	f_{cu} (MPa)	ε_{cu} (%)	$\varepsilon_{h,rup}$ (%)
Zhao et al. (2014)	2014	NA	0	20	0.53	0	153.00	305.00	45.00	0.28	30.70	98.70	0.17	46.70	1.06	1.46
Zhao et al. (2014)	2014	NA	0	20	0.53	0	153.00	305.00	45.00	0.28	30.70	98.70	0.17	48.00	0.84	1.24
Zhao et al. (2014)	2014	NA	0	20	0.53	0	153.00	305.00	45.00	0.28	30.70	98.70	0.34	59.50	1.36	1.33
Zhao et al. (2014)	2014	NA	0	20	0.53	0	153.00	305.00	45.00	0.28	30.70	98.70	0.34	57.40	1.38	1.44
Zhao et al. (2014)	2014	NA	0	20	0.53	0	153.00	305.00	45.00	0.28	30.70	98.70	0.51	69.60	1.61	1.45
Zhao et al. (2014)	2014	NA	0	20	0.53	0	153.00	305.00	45.00	0.28	30.70	98.70	0.51	70.00	1.48	1.45
Zhao et al. (2014)	2014	RCA	20	20	0.53	0	153.00	305.00	44.90	0.26	31.60	98.70	0.17	46.50	0.81	1.26
Zhao et al. (2014)	2014	RCA	20	20	0.53	0	153.00	305.00	44.90	0.26	31.60	98.70	0.17	47.10	0.90	1.43
Zhao et al. (2014)	2014	RCA	20	20	0.53	0	153.00	305.00	44.90	0.26	31.60	98.70	0.34	57.30	0.95	1.24
Zhao et al. (2014)	2014	RCA	20	20	0.53	0	153.00	305.00	44.90	0.26	31.60	98.70	0.34	59.20	1.15	1.35
Zhao et al. (2014)	2014	RCA	20	20	0.53	0	153.00	305.00	44.90	0.26	31.60	98.70	0.51	71.90	1.42	1.33
Zhao et al. (2014)	2014	RCA	20	20	0.53	0	153.00	305.00	44.90	0.26	31.60	98.70	0.51	68.70	1.23	1.31
Zhao et al. (2014)	2014	RCA	100	20	0.53	0	153.00	305.00	34.30	0.30	27.00	98.70	0.17	42.70	0.98	1.18
Zhao et al. (2014)	2014	RCA	100	20	0.53	0	153.00	305.00	37.30	0.28	27.80	98.70	0.17	45.40	1.20	1.42
Zhao et al. (2014)	2014	RCA	100	20	0.53	0	153.00	305.00	34.30	0.30	27.00	98.70	0.34	53.30	1.34	1.24
Zhao et al. (2014)	2014	RCA	100	20	0.53	0	153.00	305.00	34.30	0.30	27.00	98.70	0.34	56.20	1.78	1.54
Zhao et al. (2014)	2014	RCA	100	20	0.53	0	153.00	305.00	34.30	0.30	27.00	98.70	0.51	68.00	1.71	1.50
Zhao et al. (2014)	2014	RCA	100	20	0.53	0	153.00	305.00	34.30	0.30	27.00	98.70	0.51	68.00	1.60	1.41
Teng et al. (2016)	2016	NA	0	70	0.46	0	152.50	305.00	31.70	0.24	–	78.80	2.55	71.50	2.05	1.84
Teng et al. (2016)	2016	NA	0	70	0.46	0	152.50	305.00	31.20	0.25	–	78.80	2.55	80.00	2.49	2.09
Teng et al. (2016)	2016	RCL	15	70	0.46	0	152.50	305.00	31.40	0.23	–	78.80	2.55	87.10	2.86	2.28
Teng et al. (2016)	2016	RCL	15	70	0.46	0	152.50	305.00	32.90	0.25	–	78.80	2.55	68.30	1.56	1.41
Teng et al. (2016)	2016	RCL	30	70	0.46	0	152.50	305.00	34.50	0.23	–	78.80	2.55	80.00	1.92	1.80
Teng et al. (2016)	2016	RCL	30	70	0.46	0	152.50	305.00	34.60	0.24	–	78.80	2.55	82.40	2.18	1.98
Teng et al. (2016)	2016	NA	0	70	0.46	0	152.50	305.00	31.70	0.24	–	78.80	3.4	97.80	3.06	2.21
Teng et al. (2016)	2016	NA	0	70	0.46	0	152.50	305.00	31.20	0.25	–	78.80	3.4	89.80	2.39	1.61
Teng et al. (2016)	2016	RCL	15	70	0.46	0	152.50	305.00	31.40	0.23	–	78.80	3.4	111.90	3.33	2.33
Teng et al. (2016)	2016	RCL	15	70	0.46	0	152.50	305.00	32.90	0.25	–	78.80	3.4	108.40	2.80	2.12
Teng et al. (2016)	2016	RCL	30	70	0.46	0	152.50	305.00	34.50	0.23	–	78.80	3.4	111.30	2.95	2.05
Teng et al. (2016)	2016	RCL	30	70	0.46	0	152.50	305.00	34.60	0.24	–	78.80	3.4	100.80	2.74	1.92
Teng et al. (2016)	2016	NA	0	70	0.45	0	152.50	305.00	68.40	0.22	–	78.80	2.55	84.10	0.83	1.39
Teng et al. (2016)	2016	NA	0	70	0.45	0	152.50	305.00	67.10	0.23	–	78.80	2.55	89.70	1.01	1.58
Teng et al. (2016)	2016	RCL	30	70	0.45	0	152.50	305.00	58.10	0.19	–	78.80	2.55	88.00	1.08	1.59
Teng et al. (2016)	2016	RCL	30	70	0.45	0	152.50	305.00	59.90	0.20	–	78.80	2.55	92.20	1.21	1.59
Teng et al. (2016)	2016	NA	0	70	0.45	0	152.50	305.00	68.40	0.22	–	78.80	3.4	120.80	2.06	1.79
Teng et al. (2016)	2016	NA	0	70	0.45	0	152.50	305.00	67.10	0.23	–	78.80	3.4	109.60	1.34	1.38
Teng et al. (2016)	2016	RCL	30	70	0.45	0	152.50	305.00	58.10	0.19	–	78.80	3.4	117.70	1.56	1.68
Teng et al. (2016)	2016	RCL	30	70	0.45	0	152.50	305.00	59.90	0.20	–	78.80	3.4	123.30	2.24	1.83
Zhou et al. (2016)	2016	NA	0	31.5	0.35	0	150.00	300.00	55.08	0.20	30.30	272.73	0.167	65.14	1.05	1.22
Zhou et al. (2016)	2016	NA	0	31.5	0.35	0	150.00	300.00	55.08	0.20	30.30	272.73	0.167	77.28	1.09	1.22
Zhou et al. (2016)	2016	NA	0	31.5	0.35	0	150.00	300.00	55.08	0.20	30.30	272.73	0.167	76.32	1.00	1.22
Zhou et al. (2016)	2016	NA	0	31.5	0.35	0	150.00	300.00	75.39	0.20	30.30	272.73	0.501	129.80	1.90	1.49
Zhou et al. (2016)	2016	NA	0	31.5	0.35	0	150.00	300.00	75.39	0.20	30.30	272.73	0.501	134.76	1.96	1.49
Zhou et al. (2016)	2016	NA	0	31.5	0.35	0	150.00	300.00	75.39	0.20	30.30	272.73	0.501	125.76	1.76	1.49

(*continued on next page*)

Table A.2 (*continued*)

Data source properties		Aggregate/fresh concrete properties					Geometry		Unconfined concrete properties			FRP properties		Confined concrete properties		
Source	Year	No of Data	A_t	R_c (%)	R_{max} (mm)	w/c (%)	D (mm)	H (mm)	f_{co} (MPa)	ε_{co} (%)	E_c (GPa)	E_{frp} (GPa)	T_{frp} (mm)	f_{cu} (MPa)	ε_{cu} (%)	$\varepsilon_{h,rup}$ (%)
Zhou et al. (2016)	2016	RCA	30	31.5	0.35	0	150.00	300.00	42.63	0.20	31.80	272.73	0.167	67.04	1.05	1.39
Zhou et al. (2016)	2016	RCA	30	31.5	0.35	0	150.00	300.00	42.63	0.20	31.80	272.73	0.167	65.22	0.96	1.39
Zhou et al. (2016)	2016	RCA	30	31.5	0.35	0	150.00	300.00	42.63	0.20	31.80	272.73	0.167	64.04	0.99	1.39
Zhou et al. (2016)	2016	RCA	30	31.5	0.35	0	150.00	300.00	62.93	0.20	31.80	272.73	0.501	96.12	1.80	1.10
Zhou et al. (2016)	2016	RCA	30	31.5	0.35	0	150.00	300.00	62.93	0.20	31.80	272.73	0.501	89.03	1.53	1.10
Zhou et al. (2016)	2016	RCA	30	31.5	0.35	0	150.00	300.00	62.93	0.20	31.80	272.73	0.501	95.78	1.77	1.10
Zhou et al. (2016)	2016	RCA	50	31.5	0.35	0	150.00	300.00	50.65	0.20	30.80	272.73	0.167	61.87	0.82	1.26
Zhou et al. (2016)	2016	RCA	50	31.5	0.35	0	150.00	300.00	50.65	0.20	30.80	272.73	0.167	62.23	0.90	1.26
Zhou et al. (2016)	2016	RCA	50	31.5	0.35	0	150.00	300.00	50.65	0.20	30.80	272.73	0.167	55.09	0.86	1.26
Zhou et al. (2016)	2016	RCA	50	31.5	0.35	0	150.00	300.00	70.95	0.20	30.80	272.73	0.501	119.59	1.49	1.39
Zhou et al. (2016)	2016	RCA	50	31.5	0.35	0	150.00	300.00	70.95	0.20	30.80	272.73	0.501	111.36	1.35	1.39
Zhou et al. (2016)	2016	RCA	50	31.5	0.35	0	150.00	300.00	70.95	0.20	30.80	272.73	0.501	113.40	1.46	1.39
Zhou et al. (2016)	2016	RCA	100	31.5	0.35	0	150.00	300.00	65.26	0.20	31.30	272.73	0.501	102.19	1.42	1.18
Zhou et al. (2016)	2016	RCA	100	31.5	0.35	0	150.00	300.00	65.26	0.20	31.30	272.73	0.501	94.04	1.77	1.18
Zhou et al. (2016)	2016	RCA	100	31.5	0.35	0	150.00	300.00	65.26	0.20	31.30	272.73	0.501	95.01	1.42	1.18
Zhou et al. (2016)	2016	RCA	100	31.5	0.45	0	150.00	300.00	37.82	0.20	31.30	272.73	0.167	58.10	0.92	1.28
Zhou et al. (2016)	2016	RCA	100	31.5	0.45	0	150.00	300.00	37.82	0.20	31.30	272.73	0.167	57.80	0.97	1.28
Zhou et al. (2016)	2016	RCA	100	31.5	0.45	0	150.00	300.00	37.82	0.20	31.30	272.73	0.167	60.92	1.04	1.28
Zhou et al. (2016)	2016	RCA	100	31.5	0.45	0	150.00	300.00	58.12	0.20	31.30	272.73	0.501	101.00	2.25	1.17
Zhou et al. (2016)	2016	RCA	100	31.5	0.45	0	150.00	300.00	58.12	0.20	31.30	272.73	0.501	93.78	2.20	1.17
Zhou et al. (2016)	2016	RCA	100	31.5	0.45	0	150.00	300.00	58.12	0.20	31.30	272.73	0.501	90.00	2.23	1.17
Zhou et al. (2016)	2016	RCA	100	31.5	0.3	0	150.00	300.00	72.23	0.20	33.00	272.73	0.501	124.77	1.61	1.40
Zhou et al. (2016)	2016	RCA	100	31.5	0.3	0	150.00	300.00	72.23	0.20	33.00	272.73	0.501	125.15	1.58	1.40
Zhou et al. (2016)	2016	RCA	100	31.5	0.3	0	150.00	300.00	72.23	0.20	33.00	272.73	0.501	117.89	1.41	1.40
Chen et al. (2016)	2016	NA	0	20	0.5	0	150.00	300.00	44.44	0.35	26.96	250.00	0.111	63.56	1.17	1.34
Chen et al. (2016)	2016	NA	0	20	0.5	0	150.00	300.00	44.44	0.35	26.96	250.00	0.111	61.71	1.40	1.35
Chen et al. (2016)	2016	NA	0	20	0.5	0	150.00	300.00	44.44	0.35	26.96	250.00	0.111	61.90	1.08	1.45
Chen et al. (2016)	2016	NA	0	20	0.5	0	150.00	300.00	44.44	0.35	26.96	250.00	0.222	78.94	1.42	1.18
Chen et al. (2016)	2016	NA	0	20	0.5	0	150.00	300.00	44.44	0.35	26.96	250.00	0.222	78.94	1.82	1.43
Chen et al. (2016)	2016	NA	0	20	0.5	0	150.00	300.00	44.44	0.35	26.96	250.00	0.222	78.74	1.56	1.26
Chen et al. (2016)	2016	NA	0	20	0.5	0	150.00	300.00	44.44	0.35	26.96	250.00	0.333	97.04	2.06	1.31
Chen et al. (2016)	2016	NA	0	20	0.5	0	150.00	300.00	44.44	0.35	26.96	250.00	0.333	95.09	1.82	1.20
Chen et al. (2016)	2016	NA	0	20	0.5	0	150.00	300.00	44.44	0.35	26.96	250.00	0.333	95.87	2.21	1.31
Chen et al. (2016)	2016	RCA	25	20	0.5	0	150.00	300.00	40.75	0.32	25.70	250.00	0.111	60.64	1.24	1.24
Chen et al. (2016)	2016	RCA	25	20	0.5	0	150.00	300.00	40.75	0.32	25.70	250.00	0.111	57.72	1.14	1.36
Chen et al. (2016)	2016	RCA	25	20	0.5	0	150.00	300.00	40.75	0.32	25.70	250.00	0.111	58.98	1.16	1.20
Chen et al. (2016)	2016	RCA	25	20	0.5	0	150.00	300.00	40.75	0.32	25.70	250.00	0.222	77.18	1.52	1.27
Chen et al. (2016)	2016	RCA	25	20	0.5	0	150.00	300.00	40.75	0.32	25.70	250.00	0.222	76.00	1.40	1.20
Chen et al. (2016)	2016	RCA	25	20	0.5	0	150.00	300.00	40.75	0.32	25.70	250.00	0.222	75.72	1.61	1.13
Chen et al. (2016)	2016	RCA	25	20	0.5	0	150.00	300.00	40.75	0.32	25.70	250.00	0.333	91.20	2.10	1.18
Chen et al. (2016)	2016	RCA	25	20	0.5	0	150.00	300.00	40.75	0.32	25.70	250.00	0.333	94.61	2.28	1.04
Chen et al. (2016)	2016	RCA	25	20	0.5	0	150.00	300.00	40.75	0.32	25.70	250.00	0.333	94.41	2.08	1.21
Chen et al. (2016)	2016	RCA	50	20	0.5	0	150.00	300.00	37.03	0.27	24.78	250.00	0.111	57.43	1.37	1.18
Chen et al. (2016)	2016	RCA	50	20	0.5	0	150.00	300.00	37.03	0.27	24.78	250.00	0.111	56.55	1.30	1.47
Chen et al. (2016)	2016	RCA	50	20	0.5	0	150.00	300.00	37.03	0.27	24.78	250.00	0.111	55.58	1.35	1.33
Chen et al. (2016)	2016	RCA	50	20	0.5	0	150.00	300.00	37.03	0.27	24.78	250.00	0.222	76.11	2.04	1.46
Chen et al. (2016)	2016	RCA	50	20	0.5	0	150.00	300.00	37.03	0.27	24.78	250.00	0.222	75.72	1.83	1.24
Chen et al. (2016)	2016	RCA	50	20	0.5	0	150.00	300.00	37.03	0.27	24.78	250.00	0.222	73.00	1.76	1.21
Chen et al. (2016)	2016	RCA	50	20	0.5	0	150.00	300.00	37.03	0.27	24.78	250.00	0.333	95.09	2.69	1.16
Chen et al. (2016)	2016	RCA	50	20	0.5	0	150.00	300.00	37.03	0.27	24.78	250.00	0.333	89.06	2.78	1.30
Chen et al. (2016)	2016	RCA	50	20	0.5	0	150.00	300.00	37.03	0.27	24.78	250.00	0.333	91.39	2.24	1.20
Chen et al. (2016)	2016	RCA	75	20	0.5	0	150.00	300.00	37.48	0.28	23.62	250.00	0.111	56.65	1.31	1.35
Chen et al. (2016)	2016	RCA	75	20	0.5	0	150.00	300.00	37.48	0.28	23.62	250.00	0.111	54.99	1.44	1.44
Chen et al. (2016)	2016	RCA	75	20	0.5	0	150.00	300.00	37.48	0.28	23.62	250.00	0.111	58.89	1.37	1.45
Chen et al. (2016)	2016	RCA	75	20	0.5	0	150.00	300.00	37.48	0.28	23.62	250.00	0.222	74.75	1.86	1.38
Chen et al. (2016)	2016	RCA	75	20	0.5	0	150.00	300.00	37.48	0.28	23.62	250.00	0.222	77.87	1.97	1.32
Chen et al. (2016)	2016	RCA	75	20	0.5	0	150.00	300.00	37.48	0.28	23.62	250.00	0.222	74.46	1.71	1.61
Chen et al. (2016)	2016	RCA	75	20	0.5	0	150.00	300.00	37.48	0.28	23.62	250.00	0.333	89.84	2.60	1.13
Chen et al. (2016)	2016	RCA	75	20	0.5	0	150.00	300.00	37.48	0.28	23.62	250.00	0.333	88.18	2.31	1.08
Chen et al. (2016)	2016	RCA	75	20	0.5	0	150.00	300.00	37.48	0.28	23.62	250.00	0.333	89.06	1.98	1.11
Chen et al. (2016)	2016	RCA	100	20	0.5	0	150.00	300.00	32.87	0.29	22.27	250.00	0.111	56.74	1.37	1.32
Chen et al. (2016)	2016	RCA	100	20	0.5	0	150.00	300.00	32.87	0.29	22.27	250.00	0.111	56.36	1.35	1.36
Chen et al. (2016)	2016	RCA	100	20	0.5	0	150.00	300.00	32.87	0.29	22.27	250.00	0.111	55.38	1.47	1.32
Chen et al. (2016)	2016	RCA	100	20	0.5	0	150.00	300.00	32.87	0.29	22.27	250.00	0.222	72.12	2.27	1.34
Chen et al. (2016)	2016	RCA	100	20	0.5	0	150.00	300.00	32.87	0.29	22.27	250.00	0.222	75.34	2.14	1.39
Chen et al. (2016)	2016	RCA	100	20	0.5	0	150.00	300.00	32.87	0.29	22.27	250.00	0.222	74.95	2.11	1.33
Chen et al. (2016)	2016	RCA	100	20	0.5	0	150.00	300.00	32.87	0.29	22.27	250.00	0.333	86.63	2.59	1.11
Chen et al. (2016)	2016	RCA	100	20	0.5	0	150.00	300.00	32.87	0.29	22.27	250.00	0.333	86.92	2.60	1.18
Chen et al. (2016)	2016	RCA	100	20	0.5	0	150.00	300.00	32.87	0.29	22.27	250.00	0.333	89.35	2.68	1.17
Gao et al. (2016)	2016	RBA	0	10	0.41	0	100.00	200.00	35.86	0.26	–	60.80	1.744	129.21	1.78	1.41
Gao et al. (2016)	2016	RBA	50	10	0.41	0	100.00	200.00	35.55	0.27	–	60.80	1.744	123.20	1.79	1.41
Gao et al. (2016)	2016	RBA	100	10	0.41	0	100.00	200.00	31.73	0.30	–	60.80	1.744	104.67	1.91	1.41

(*continued on next page*)

Table A.2 (*continued*)

Data source properties		Aggregate/fresh concrete properties					Geometry		Unconfined concrete properties			FRP properties		Confined concrete properties		
Source	Year	No of Data	A_t	R_c (%)	R_{max} (mm)	w/c (%)	D (mm)	H (mm)	f_{co} (MPa)	ε_{co} (%)	E_c (GPa)	E_{frp} (GPa)	T_{frp} (mm)	f_{cu} (MPa)	ε_{cu} (%)	$\varepsilon_{h,rup}$ (%)
Gao et al. (2016)	2016	RBA	70	10	0.41	0	100.00	200.00	33.27	0.28	–	60.80	1.744	112.93	1.86	1.41
Gao et al. (2016)	2016	RBA	70	10	0.41	0	100.00	200.00	33.27	0.28	–	60.80	2.616	148.59	2.28	1.53
Gao et al. (2016)	2016	RBA	70	10	0.41	0	100.00	200.00	33.27	0.28	–	60.80	0.872	66.99	1.51	1.31
Gao et al. (2016)	2016	RBA	70	10	0.41	0	100.00	200.00	33.27	0.28	–	213.00	0.334	96.16	1.41	0.98
Gao et al. (2016)	2016	RBA	70	10	0.41	0	100.00	200.00	33.27	0.28	–	213.00	0.668	136.99	1.62	0.76
Gao et al. (2016)	2016	RBA	70	10	0.41	0	100.00	200.00	33.27	0.28	–	213.00	1.002	161.26	1.71	0.64
Xie and Ozbakkaloglu (2016)	2016	NA	0	12	0.62	0	152.50	305.00	39.50	0.19	27.30	76.00	0.14	53.50	1.88	1.80
Xie and Ozbakkaloglu (2016)	2016	NA	0	12	0.62	0	152.50	305.00	42.80	0.19	27.30	76.00	0.28	52.20	1.77	1.84
Xie and Ozbakkaloglu (2016)	2016	NA	0	12	0.62	0	152.50	305.00	41.80	0.19	27.30	76.00	0.42	51.80	1.83	1.86
Xie and Ozbakkaloglu (2016)	2016	RCA	50	12	0.62	0	152.50	305.00	43.90	0.21	26.80	76.00	0.14	50.20	1.81	1.66
Xie and Ozbakkaloglu (2016)	2016	RCA	50	12	0.62	0	152.50	305.00	44.90	0.21	26.80	76.00	0.28	51.40	1.72	1.61
Xie and Ozbakkaloglu (2016)	2016	RCA	50	12	0.62	0	152.50	305.00	41.40	0.21	26.80	76.00	0.42	50.90	1.75	1.63
Xie and Ozbakkaloglu (2016)	2016	RCA	100	12	0.62	0	152.50	305.00	45.10	0.25	23.40	76.00	0.14	48.40	1.56	1.50
Xie and Ozbakkaloglu (2016)	2016	RCA	100	12	0.62	0	152.50	305.00	45.40	0.25	23.40	76.00	0.42	48.60	1.63	1.61
Xie and Ozbakkaloglu (2016)	2016	NA	0	12	0.37	8	152.50	305.00	77.40	0.24	34.60	76.00	0.14	86.50	1.53	1.57
Xie and Ozbakkaloglu (2016)	2016	NA	0	12	0.37	8	152.50	305.00	76.00	0.24	34.60	76.00	0.28	87.40	1.35	1.58
Xie and Ozbakkaloglu (2016)	2016	NA	0	12	0.37	8	152.50	305.00	78.40	0.24	34.60	76.00	0.42	83.30	1.43	1.56
Xie and Ozbakkaloglu (2016)	2016	RCA	50	12	0.38	8	152.50	305.00	73.00	0.26	34.00	76.00	0.14	80.80	1.31	1.49
Xie and Ozbakkaloglu (2016)	2016	RCA	50	12	0.38	8	152.50	305.00	73.20	0.26	34.00	76.00	0.28	82.50	1.32	1.50
Xie and Ozbakkaloglu (2016)	2016	RCA	50	12	0.38	8	152.50	305.00	72.50	0.26	34.00	76.00	0.42	83.50	1.27	1.47
Xie and Ozbakkaloglu (2016)	2016	RCA	100	12	0.4	8	152.50	305.00	71.30	0.28	32.30	76.00	0.14	79.30	1.24	1.30
Xie and Ozbakkaloglu (2016)	2016	RCA	100	12	0.4	8	152.50	305.00	71.00	0.28	32.30	76.00	0.28	78.30	1.13	1.35
Xie and Ozbakkaloglu (2016)	2016	RCA	100	12	0.4	8	152.50	305.00	71.60	0.28	32.30	76.00	0.42	81.50	1.20	1.33
Xie and Ozbakkaloglu (2016)	2016	NA	0	12	0.37	8	152.50	305.00	73.10	0.24	34.60	236.00	0.111	92.80	1.31	1.23
Xie and Ozbakkaloglu (2016)	2016	NA	0	12	0.37	8	152.50	305.00	74.40	0.24	34.60	236.00	0.222	96.60	1.27	1.19
Xie and Ozbakkaloglu (2016)	2016	NA	0	12	0.37	8	152.50	305.00	74.40	0.24	34.60	236.00	0.333	95.30	1.32	1.19
Xie and Ozbakkaloglu (2016)	2016	RCA	50	12	0.38	8	152.50	305.00	76.50	0.26	34.00	236.00	0.111	90.10	1.17	1.09
Xie and Ozbakkaloglu (2016)	2016	RCA	50	12	0.38	8	152.50	305.00	75.70	0.26	34.00	236.00	0.222	90.80	1.28	1.08

(*continued on next page*)

Table A.2 (*continued*)

Data source properties		Aggregate/fresh concrete properties					Geometry		Unconfined concrete properties			FRP properties		Confined concrete properties		
Source	Year	No of Data	A_t	R_c (%)	R_{max} (mm)	w/c (%)	D (mm)	H (mm)	f_{co} (MPa)	ε_{co} (%)	E_c (GPa)	E_{frp} (GPa)	T_{frp} (mm)	f_{cu} (MPa)	ε_{cu} (%)	$\varepsilon_{h,rup}$ (%)
Xie and Ozbakkaloglu (2016)	2016	RCA	50	12	0.38	8	152.50	305.00	74.90	0.26	34.00	236.00	0.333	92.90	1.22	1.05
Xie and Ozbakkaloglu (2016)	2016	RCA	100	12	0.4	8	152.50	305.00	74.40	0.28	32.30	236.00	0.111	85.10	1.09	1.02
Xie and Ozbakkaloglu (2016)	2016	RCA	100	12	0.4	8	152.50	305.00	76.40	0.28	32.30	236.00	0.222	83.00	1.14	0.99
Xie and Ozbakkaloglu (2016)	2016	RCA	100	12	0.4	8	152.50	305.00	77.40	0.28	32.30	236.00	0.333	83.50	1.12	0.94
Chen et al. (2018)	2018	NA	0	20	0.5	0	150.00	300.00	45.80	0.24	34.00	244.00	0.111	56.10	0.89	1.27
Chen et al. (2018)	2018	NA	0	20	0.5	0	150.00	300.00	45.80	0.24	34.00	244.00	0.222	84.90	1.86	1.44
Chen et al. (2018)	2018	NA	0	20	0.5	0	150.00	300.00	45.80	0.24	34.00	244.00	0.333	108.90	2.81	1.53
Chen et al. (2018)	2018	NA	0	20	0.5	0	200.00	400.00	44.30	0.24	32.20	244.00	0.111	49.20	0.70	1.29
Chen et al. (2018)	2018	NA	0	20	0.5	0	200.00	400.00	44.30	0.24	32.20	244.00	0.222	68.80	1.56	1.57
Chen et al. (2018)	2018	NA	0	20	0.5	0	200.00	400.00	44.30	0.24	32.20	244.00	0.333	92.20	2.54	1.76
Chen et al. (2018)	2018	NA	0	20	0.5	0	300.00	600.00	43.60	0.26	30.10	244.00	0.111	42.50	0.36	1.05
Chen et al. (2018)	2018	NA	0	20	0.5	0	300.00	600.00	43.60	0.26	30.10	244.00	0.222	52.80	0.96	1.33
Chen et al. (2018)	2018	NA	0	20	0.5	0	300.00	600.00	43.60	0.26	30.10	244.00	0.333	70.60	1.48	1.65
Chen et al. (2018)	2018	RCA	100	20	0.5	0	150.00	300.00	41.60	0.23	27.70	244.00	0.111	54.10	1.13	1.43
Chen et al. (2018)	2018	RCA	100	20	0.5	0	150.00	300.00	41.60	0.23	27.70	244.00	0.222	80.50	2.16	1.48
Chen et al. (2018)	2018	RCA	100	20	0.5	0	150.00	300.00	41.60	0.23	27.70	244.00	0.333	101.00	2.96	1.47
Chen et al. (2018)	2018	RCA	100	20	0.5	0	200.00	400.00	41.50	0.25	27.00	244.00	0.111	46.00	0.55	1.00
Chen et al. (2018)	2018	RCA	100	20	0.5	0	200.00	400.00	41.50	0.25	27.00	244.00	0.222	69.40	1.98	1.67
Chen et al. (2018)	2018	RCA	100	20	0.5	0	200.00	400.00	41.50	0.25	27.00	244.00	0.333	87.90	2.37	1.56
Chen et al. (2018)	2018	RCA	100	20	0.5	0	300.00	600.00	38.80	0.25	26.40	244.00	0.111	41.60	0.46	1.18
Chen et al. (2018)	2018	RCA	100	20	0.5	0	300.00	600.00	38.80	0.25	26.40	244.00	0.222	49.30	1.18	1.34
Chen et al. (2018)	2018	RCA	100	20	0.5	0	300.00	600.00	38.80	0.25	26.40	244.00	0.333	62.30	1.74	1.62
Li et al. (2019)	2019	NA	0	31.5	0.53	0	150.00	300.00	16.80	0.20	–	264.00	0.167	58.90	1.45	1.15
Li et al. (2019)	2019	NA	0	31.5	0.53	0	150.00	300.00	16.80	0.20	–	264.00	0.167	51.90	1.19	0.72
Li et al. (2019)	2019	RCA	50	31.5	0.53	0	150.00	300.00	18.60	0.20	–	264.00	0.167	55.20	1.51	0.98
Li et al. (2019)	2019	RCA	50	31.5	0.53	0	150.00	300.00	18.60	0.20	–	264.00	0.167	53.90	1.39	0.98
Li et al. (2019)	2019	RCA	50	31.5	0.53	0	150.00	300.00	18.60	0.20	–	264.00	0.334	72.60	1.76	0.95
Li et al. (2019)	2019	RCA	50	31.5	0.53	0	150.00	300.00	18.60	0.20	–	264.00	0.334	83.30	2.53	1.27
Li et al. (2019)	2019	RCA	50	31.5	0.53	0	150.00	300.00	18.60	0.20	–	264.00	0.501	101.70	2.99	1.06
Li et al. (2019)	2019	RCA	50	31.5	0.53	0	150.00	300.00	18.60	0.20	–	264.00	0.501	114.70	2.80	1.03
Li et al. (2019)	2019	RCA	100	31.5	0.53	0	150.00	300.00	23.20	0.20	–	264.00	0.167	57.40	1.29	1.10
Li et al. (2019)	2019	RCA	100	31.5	0.53	0	150.00	300.00	23.20	0.20	–	264.00	0.167	51.90	0.95	0.89
Jiang et al. (2020)	2020	NA	0	20	0.4	0	150.00	300.00	56.90	0.25	31.20	264.00	0.111	71.90	0.98	1.38
Jiang et al. (2020)	2020	NA	0	20	0.4	0	150.00	300.00	56.90	0.25	31.20	264.00	0.111	71.90	0.97	1.45
Jiang et al. (2020)	2020	NA	0	20	0.4	0	150.00	300.00	56.90	0.25	31.20	264.00	0.111	70.90	0.96	1.44
Jiang et al. (2020)	2020	NA	0	20	0.4	0	150.00	300.00	56.90	0.25	31.20	264.00	0.222	94.90	1.49	1.56
Jiang et al. (2020)	2020	NA	0	20	0.4	0	150.00	300.00	56.90	0.25	31.20	264.00	0.222	96.40	1.56	1.35
Jiang et al. (2020)	2020	NA	0	20	0.4	0	150.00	300.00	56.90	0.25	31.20	264.00	0.333	120.90	1.98	1.55
Jiang et al. (2020)	2020	NA	0	20	0.4	0	150.00	300.00	56.90	0.25	31.20	264.00	0.333	118.10	1.73	1.54
Jiang et al. (2020)	2020	NA	0	20	0.4	0	150.00	300.00	56.90	0.25	31.20	264.00	0.333	117.40	1.86	1.46
Jiang et al. (2020)	2020	RBA	15	20	0.4	0	150.00	300.00	49.20	0.27	29.00	264.00	0.111	62.80	0.97	1.28
Jiang et al. (2020)	2020	RBA	15	20	0.4	0	150.00	300.00	49.20	0.27	29.00	264.00	0.111	62.40	1.04	1.17
Jiang et al. (2020)	2020	RBA	15	20	0.4	0	150.00	300.00	49.20	0.27	29.00	264.00	0.111	60.70	0.95	1.28
Jiang et al. (2020)	2020	RBA	15	20	0.4	0	150.00	300.00	49.20	0.27	29.00	264.00	0.222	88.00	1.91	1.49
Jiang et al. (2020)	2020	RBA	15	20	0.4	0	150.00	300.00	49.20	0.27	29.00	264.00	0.222	85.10	1.73	1.30
Jiang et al. (2020)	2020	RBA	15	20	0.4	0	150.00	300.00	49.20	0.27	29.00	264.00	0.222	84.50	1.60	1.27
Jiang et al. (2020)	2020	RBA	15	20	0.4	0	150.00	300.00	49.20	0.27	29.00	264.00	0.333	108.30	2.37	1.35
Jiang et al. (2020)	2020	RBA	15	20	0.4	0	150.00	300.00	49.20	0.27	29.00	264.00	0.333	107.30	2.50	1.27

(*continued on next page*)

Table A.2 (*continued*)

Data source properties		Aggregate/fresh concrete properties					Geometry		Unconfined concrete properties			FRP properties		Confined concrete properties		
Source	Year	No of Data	A_t	R_c (%)	R_{max} (mm)	w/c (%)	D (mm)	H (mm)	f_{co} (MPa)	ε_{co} (%)	E_c (GPa)	E_{frp} (GPa)	T_{frp} (mm)	f_{cu} (MPa)	ε_{cu} (%)	$\varepsilon_{h,rup}$ (%)
Jiang et al. (2020)	2020	RBA	15	20	0.4	0	150.00	300.00	49.20	0.27	29.00	264.00	0.333	106.00	2.31	1.31
Jiang et al. (2020)	2020	RBA	30	20	0.4	0	150.00	300.00	44.90	0.23	28.80	264.00	0.111	58.50	0.94	1.32
Jiang et al. (2020)	2020	RBA	30	20	0.4	0	150.00	300.00	44.90	0.23	28.80	264.00	0.111	55.20	1.00	1.04
Jiang et al. (2020)	2020	RBA	30	20	0.4	0	150.00	300.00	44.90	0.23	28.80	264.00	0.111	57.30	0.91	1.23
Jiang et al. (2020)	2020	RBA	30	20	0.4	0	150.00	300.00	44.90	0.23	28.80	264.00	0.222	76.70	1.61	1.26
Jiang et al. (2020)	2020	RBA	30	20	0.4	0	150.00	300.00	44.90	0.23	28.80	264.00	0.222		1.86	79.40
Jiang et al. (2020)	2020	RBA	30	20	0.4	0	150.00	300.00	44.90	0.23	28.80	264.00	0.222		1.51	77.60
Jiang et al. (2020)	2020	RBA	30	20	0.4	0	150.00	300.00	44.90	0.23	28.80	264.00	0.333		2.27	95.40
Jiang et al. (2020)	2020	RBA	30	20	0.4	0	150.00	300.00	44.90	0.23	28.80	264.00	0.333		2.30	93.90
Jiang et al. (2020)	2020	RBA	30	20	0.4	0	150.00	300.00	44.90	0.23	28.80	264.00	0.333		2.38	96.00
Jiang et al. (2020)	2020	RBA	60	20	0.4	0	150.00	300.00	34.60	0.21	21.70	264.00	0.111		1.00	48.40
Jiang et al. (2020)	2020	RBA	60	20	0.4	0	150.00	300.00	34.60	0.21	21.70	264.00	0.111		0.93	47.20
Jiang et al. (2020)	2020	RBA	60	20	0.4	0	150.00	300.00	34.60	0.21	21.70	264.00	0.111		1.00	48.40
Jiang et al. (2020)	2020	RBA	60	20	0.4	0	150.00	300.00	34.60	0.21	21.70	264.00	0.222		1.53	65.10
Jiang et al. (2020)	2020	RBA	60	20	0.4	0	150.00	300.00	34.60	0.21	21.70	264.00	0.222		1.91	69.10
Jiang et al. (2020)	2020	RBA	60	20	0.4	0	150.00	300.00	34.60	0.21	21.70	264.00	0.222		2.07	65.20
Jiang et al. (2020)	2020	RBA	60	20	0.4	0	150.00	300.00	34.60	0.21	21.70	264.00	0.333		2.51	83.70
Jiang et al. (2020)	2020	RBA	60	20	0.4	0	150.00	300.00	34.60	0.21	21.70	264.00	0.333		2.77	85.50
Jiang et al. (2020)	2020	RBA	60	20	0.4	0	150.00	300.00	34.60	0.21	21.70	264.00	0.333		2.23	78.80
Jiang et al. (2020)	2020	RBA	100	20	0.4	0	150.00	300.00	31.10	0.23	18.60	264.00	0.111		1.23	43.40
Jiang et al. (2020)	2020	RBA	100	20	0.4	0	150.00	300.00	31.10	0.23	18.60	264.00	0.111		1.20	44.50
Jiang et al. (2020)	2020	RBA	100	20	0.4	0	150.00	300.00	31.10	0.23	18.60	264.00	0.111		1.23	43.90
Jiang et al. (2020)	2020	RBA	100	20	0.4	0	150.00	300.00	31.10	0.23	18.60	264.00	0.222		2.20	58.60
Jiang et al. (2020)	2020	RBA	100	20	0.4	0	150.00	300.00	31.10	0.23	18.60	264.00	0.222		2.20	58.40
Jiang et al. (2020)	2020	RBA	100	20	0.4	0	150.00	300.00	31.10	0.23	18.60	264.00	0.222		2.27	60.10
Jiang et al. (2020)	2020	RBA	100	20	0.4	0	150.00	300.00	31.10	0.23	18.60	264.00	0.333		3.36	76.70
Jiang et al. (2020)	2020	RBA	100	20	0.4	0	150.00	300.00	31.10	0.23	18.60	264.00	0.333		3.31	74.50
Jiang et al. (2020)	2020	RBA	100	20	0.4	0	150.00	300.00	31.10	0.23	18.60	264.00	0.333		2.78	73.30
Zhou et al. (2021)	2021	NA	0	20	–	0	200.00	400.00	42.10	0.31	–	246.00	0.334		2.40	79.70
Zhou et al. (2021)	2021	NA	0	20	–	0	200.00	400.00	41.90	0.31	–	246.00	0.334		2.40	79.70
Zhou et al. (2021)	2021	RCL	15	20	–	0	200.00	400.00	35.90	0.31	–	246.00	0.334		2.24	79.00
Zhou et al. (2021)	2021	RCL	15	20	–	0	200.00	400.00	37.10	0.31	–	246.00	0.334		2.24	79.00
Zhou et al. (2021)	2021	RCL	30	20	–	0	200.00	400.00	33.30	0.31	–	246.00	0.334		2.25	80.20
Zhou et al. (2021)	2021	RCL	30	20	–	0	200.00	400.00	33.30	0.31	–	246.00	0.334		2.25	80.20
Zhou et al. (2021)	2021	NA	0	20	–	0	200.00	400.00	42.10	0.31	–	246.00	0.501		3.04	98.00
Zhou et al. (2021)	2021	NA	0	20	–	0	200.00	400.00	41.90	0.31	–	246.00	0.501		3.12	109.60
Zhou et al. (2021)	2021	RCL	15	20	–	0	200.00	400.00	35.90	0.31	–	246.00	0.501		3.08	105.70
Zhou et al. (2021)	2021	RCL	15	20	–	0	200.00	400.00	37.10	0.31	–	246.00	0.501		2.41	99.00
Zhou et al. (2021)	2021	RCL	30	20	–	0	200.00	400.00	33.30	0.31	–	246.00	0.501		2.12	91.50
Zhou et al. (2021)	2021	RCL	30	20	–	0	200.00	400.00	33.30	0.31	–	246.00	0.501		2.61	103.80
Zhou et al. (2021)	2021	NA	0	20	–	0	200.00	400.00	65.20	0.31	–	246.00	0.334		1.64	99.50
Zhou et al. (2021)	2021	NA	0	20	–	0	200.00	400.00	67.10	0.31	–	246.00	0.334		1.42	93.80
Zhou et al. (2021)	2021	RCL	15	20	–	0	200.00	400.00	56.60	0.31	–	246.00	0.334		1.33	86.30
Zhou et al. (2021)	2021	RCL	15	20	–	0	200.00	400.00	56.60	0.31	–	246.00	0.334		1.43	94.90

(*continued on next page*)

Table A.2 (*continued*)

Data source properties		Aggregate/fresh concrete properties					Geometry		Unconfined concrete properties			FRP properties		Confined concrete properties		
Source	Year	No of Data	A_t	R_c (%)	R_{max} (mm)	w/c (%)	D (mm)	H (mm)	f_{co} (MPa)	ε_{co} (%)	E_c (GPa)	E_{frp} (GPa)	T_{frp} (mm)	f_{cu} (MPa)	ε_{cu} (%)	$\varepsilon_{h,rup}$ (%)
Zhou et al. (2021)	2021	RCL	30	20	–	0	200.00	400.00	50.00	0.31	–	246.00	0.334		1.28	89.80
Zhou et al. (2021)	2021	RCL	30	20	–	0	200.00	400.00	48.00	0.31	–	246.00	0.334		1.43	94.20
Zhou et al. (2021)	2021	NA	0	20	–	0	200.00	400.00	65.20	0.29	–	246.00	0.501		1.75	119.50
Zhou et al. (2021)	2021	NA	0	20	–	0	200.00	400.00	67.10	0.29	–	246.00	0.501		1.61	113.50
Zhou et al. (2021)	2021	RCL	15	20	–	0	200.00	400.00	56.60	0.29	–	246.00	0.501		1.95	121.30
Zhou et al. (2021)	2021	RCL	15	20	–	0	200.00	400.00	56.60	0.29	–	246.00	0.501		2.00	120.30
Zhou et al. (2021)	2021	RCL	30	20	–	0	200.00	400.00	50.00	0.29	–	246.00	0.501		2.08	120.40
Zhou et al. (2021)	2021	RCL	30	20	–	0	200.00	400.00	48.00	0.29	–	246.00	0.501		1.78	115.30

Data availability

Some data and models that support the findings of this study are provided in the appendix and can be accessed via https://frcrac.streamlit.app/. Other data used in this study are not publicly available.

References

Akiba, T., Sano, S., Yanase, T., Ohta, T., Koyama, M., 2019. Optuna: a next-generation hyperparameter optimization framework. In: Proceedings of the 25th ACM SIGKDD International Conference on Knowledge Discovery & Data Mining. Association for Computing Machinery, New York, NY, USA, pp. 2623–2631. https://doi.org/10.1145/3292500.3330701.

Ali, R., Muayad, M., Mohammed, A.S., Asteris, P.G., 2023. Analysis and prediction of the effect of nanosilica on the compressive strength of concrete with different mix proportions and specimen sizes using various numerical approaches. Struct. Concr. 24, 4161–4184. https://doi.org/10.1002/suco.202200718.

Ali, L., Isleem, H.F., Bahrami, A., Jha, I., Zou, G., Kumar, R., Sadeq, A.M., Jahami, A., 2024. Integrated behavioural analysis of FRP-confined circular columns using FEM and machine learning. Composites Part C: Open Access 13, 100444. https://doi.org/10.1016/j.jcomc.2024.100444.

Behnood, A., Olek, J., Glinicki, M.A., 2015. Predicting modulus elasticity of recycled aggregate concrete using M5′ model tree algorithm. Constr. Build. Mater. 94, 137–147. https://doi.org/10.1016/j.conbuildmat.2015.06.055.

Bessa, M.A., Bostanabad, R., Liu, Z., Hu, A., Apley, D.W., Brinson, C., Chen, W., Liu, W.K., 2017. A framework for data-driven analysis of materials under uncertainty: countering the curse of dimensionality. Comput. Methods Appl. Mech. Eng. 320, 633–667. https://doi.org/10.1016/j.cma.2017.03.037.

Bonifácio, A.L., Mendes, J.C., Farage, M.C.R., Barbosa, F.S., Barbosa, C.B., Beaucour, A.-L., 2019. Application of support vector machine and finite element method to predict the mechanical properties of concrete. Lat. Am. J. Solid. Struct. 16. https://doi.org/10.1590/1679-78255297.

Chakrabarti, A., Chandra, A., Bharagava, P., 2008. Finite element analysis of concrete columns confined with FRP sheets. J. Reinforc. Plast. Compos. 27, 1349–1373. https://doi.org/10.1177/0731684408089859.

Chen, G.M., He, Y.H., Jiang, T., Lin, C.J., 2016. Behavior of CFRP-confined recycled aggregate concrete under axial compression. Constr. Build. Mater. 111, 85–97. https://doi.org/10.1016/j.conbuildmat.2016.01.054.

Chen, G.M., Zhang, J.J., Jiang, T., Lin, C.J., He, Y.H., 2018. Compressive behavior of CFRP-confined recycled aggregate concrete in different-sized circular sections. J. Compos. Construct. 22. https://doi.org/10.1061/(asce)cc.1943-5614.0000859.

Chen, W., Xu, J., Yu, K., Yu, J., Ma, M., Ma, Z., 2025. Performance-based design of FRP-confined recycled aggregate concrete powered by machine learning techniques. Eng. Struct. 336, 120478. https://doi.org/10.1016/j.engstruct.2025.120478.

Dada, T.E., Gong, G., Xia, J., Di Sarno, L., 2024. Stress-strain behaviour of axially loaded FRP-confined natural and recycled aggregate concrete using design-oriented and machine learning approaches. J. Build. Eng. 95, 110256. https://doi.org/10.1016/j.jobe.2024.110256.

e Silva, L.M., Christoforo, A.L., Carvalho, R.C., 2021. Calibration of concrete damaged plasticity model parameters for shear walls. Materia 26, e12944. https://doi.org/10.1590/S1517-707620210001.1244.

Fardis, M.N., Khalili, H.H., 1982. FRP-encased concrete as a structural material. Mag. Concr. Res. 34, 191–202. https://doi.org/10.1680/macr.1982.34.121.191.

Fu, W., Sun, B., Noguchi, T., Zhao, W., Ye, J., 2023. Prediction of internal relative humidity of concrete under different thermal conditions using an enhanced long short-term memory network. Therm. Sci. Eng. Prog. 38, 101629. https://doi.org/10.1016/j.tsep.2022.101629.

Gao, C., Huang, L., Yan, L., Kasal, B., Li, W., 2016. Behavior of glass and carbon FRP tube encased recycled aggregate concrete with recycled clay brick aggregate. Compos. Struct. 155, 245–254. https://doi.org/10.1016/j.compstruct.2016.08.021.

Gers, F.A., Schmidhuber, J., Cummins, F., 2000. Learning to forget: continual prediction with LSTM. Neural Comput. 12, 2451–2471. https://doi.org/10.1162/089976600300015015.

Hochreiter, S., Schmidhuber, J., 1997. Long short-term memory. Neural Comput. 9, 1735–1780. https://doi.org/10.1162/neco.1997.9.8.1735.

Isleem, H.F., Tayeh, B.A., Abid, M., Iqbal, M., Mohamed, A.M., El Sherbiny, M.G., 2022. Finite element and artificial neural network modeling of FRP-RC columns under axial compression loading. Front. Mater. 9–2022. https://doi.org/10.3389/fmats.2022.888909.

Isleem, H.F., Qiong, T., Chukka, N.D.K.R., Kumar, R., Nagaraju, T.V., Hamed, A.Y., 2025. Machine learning and nonlinear finite element analysis of fiber-reinforced polymer-confined concrete-steel double-skin tubular columns under axial compression. Struct. Concr. 26, 248–292. https://doi.org/10.1002/suco.202300835.

Jiang, Wang, X.M., Zhang, W.P., Chen, G.M., Lin, Z.H., 2020. Behavior of FRP-confined recycled brick aggregate concrete under monotonic compression. J. Compos. Construct. 24. https://doi.org/10.1061/(asce)cc.1943-5614.0001080.

Jolly, C.K., Lilistone, D., 1998. The stress–strain behavior of concrete confined by advanced fibre composites. In: 8th BCA Conference Higher Education and the Concrete Industry. Southampton.

Karbhari, V.M., Gao, Y., 1997. Composite jacketed concrete under uniaxial compression–verification of simple design equations. J. Mater. Civ. Eng. 9, 185–193. https://api.semanticscholar.org/CorpusID:137031219.

Kurad, R., Silvestre, J.D., de Brito, J., Ahmed, H., 2017. Effect of incorporation of high volume of recycled concrete aggregates and fly ash on the strength and global warming potential of concrete. J. Clean. Prod. 166, 485–502. https://doi.org/10.1016/j.jclepro.2017.07.236.

Lam, L., Teng, J.G., 2001. A new stress-strain model for FRP-confined concrete. In: International Conference FRP Composite in Civil Engineering, Hong Kong, pp. 283–292.

Lam, L., Teng, J.G., 2003a. Design-oriented stress–strain model for FRP-confined concrete. Constr. Build. Mater. 17, 471–489. https://doi.org/10.1016/S0950-0618(03)00045-X.

Lam, L., Teng, J.G., 2003b. Design-oriented stress-strain model for FRP-confined concrete. Constr. Build. Mater. 17, 471–489. https://doi.org/10.1016/S0950-0618(03)00045-X.

Leite, M.B., Figueire do Filho, J.G.L., Lima, P.R.L., 2013. Workability study of concretes made with recycled mortar aggregate. Mater. Struct. 46, 1765–1778. https://doi.org/10.1617/s11527-012-0010-4.

Li, P.-D., Wu, Y.-F., 2023. Damage evolution and full-field 3D strain distribution in passively confined concrete. Cem. Concr. Compos. 138, 104979. https://doi.org/10.1016/j.cemconcomp.2023.104979.

Li, P., Sui, L., Xing, F., Zhou, Y., 2019. Static and cyclic response of low-strength recycled aggregate concrete strengthened using fiber-reinforced polymer. Compos. B Eng. 160, 37–49. https://doi.org/10.1016/j.compositesb.2018.10.002.

Li, B., Hou, S., Duan, Z., Li, L., Guo, W., 2021. Rheological behavior and compressive strength of concrete made with recycled fine aggregate of different size range. Constr. Build. Mater. 268, 121172. https://doi.org/10.1016/j.conbuildmat.2020.121172.

Lin, C.T., Li, Y.F., 2003. An effective peak stress formula for concrete confined with carbon fiber reinforced plastics. Can. J. Civ. Eng. 30, 882–889. https://doi.org/10.1139/l03-047.

Medina, C., Zhu, W., Howind, T., Sánchez De Rojas, M.I., Frías, M., 2014. Influence of mixed recycled aggregate on the physical-mechanical properties of recycled concrete. J. Clean. Prod. 68, 216–225. https://doi.org/10.1016/j.jclepro.2014.01.002.

Meng, F., Pei, H., 2023. Cyclic shear stress-strain prediction of saturated sand based on the unrolled seq2seq model and scheduled sampling. Soil Dynam. Earthq. Eng. 165, 107665. https://doi.org/10.1016/j.soildyn.2022.107665.

Nguyen, Q.T., Livaoğlu, R., 2020. The effect of the ratio of Λ-shaped shear connectors on the flexural behavior of a reinforced concrete frame. Adv. Struct. Eng. 23, 2724–2740. https://doi.org/10.1177/1369433220920442.

Omer, B., Jaf, D.K.I., Abdalla, A., Mohammed, A.S., Abdulrahman, P.I., Kurda, R., 2024. Advanced modeling for predicting compressive strength in fly ash-modified recycled aggregate concrete: xgboost, MEP, MARS, and ANN approaches. Innov. Infrastruct. Solution 9, 61. https://doi.org/10.1007/s41062-024-01365-0.

Popovics, S., 1973. A numerical approach to the complete stress-strain curve of concrete. Cement Concr. Res. 3, 583–599. https://doi.org/10.1016/0008-8846(73)90096-3.

Prokhorenkova, L., Gusev, G., Vorobev, A., Dorogush, A.V., Gulin, A., 2018. CatBoost: unbiased boosting with categorical features. https://github.com/catboost/catboost.

Qureshi, L.A., Ali, B., Ali, A., 2020. Combined effects of supplementary cementitious materials (silica fume, GGBS, fly ash and rice husk ash) and steel fiber on the hardened properties of recycled aggregate concrete. Constr. Build. Mater. 263, 120636. https://doi.org/10.1016/j.conbuildmat.2020.120636.

Richard, R.M., Abbott, B.J., 1975. Versatile elastic-plastic stress-strain formula. J. Eng. Mech. Div. 101, 511–515. https://doi.org/10.1061/JMCEA3.0002047.

Teng, J.G., Jiang, T., Lam, L., Luo, Y.Z., 2009. Refinement of a design-oriented stress-strain model for FRP-confined concrete. J. Compos. Construct. 13, 269–278. https://doi.org/10.1061/(ASCE)CC.1943-5614.0000012.

Teng, J.G., Zhao, J.L., Yu, T., Li, L.J., Guo, Y.C., 2016. Behavior of FRP-confined compound concrete containing recycled concrete lumps. J. Compos. Construct. 20, 4015038. https://doi.org/10.1061/(asce)cc.1943-5614.0000602.

Thomas, C., Setién, J., Polanco, J.A., Alaejos, P., Sánchez De Juan, M., 2013. Durability of recycled aggregate concrete. Constr. Build. Mater. 40, 1054–1065. https://doi.org/10.1016/j.conbuildmat.2012.11.106.

Wu, Y.-F., Li, R.-Y., Li, P.-D., 2025. Stress–strain behavior of FRP-confined concrete under eccentric loading. J. Compos. Construct. 29, 04025048. https://doi.org/10.1061/JCCOF2.CCENG-5335.

Xiao, Y., Wu, H., 2000. Compressive behavior of concrete confined by carbon fiber composite jackets. J. Mater. Civ. Eng. 12, 139–146.

Xiao, Y., Wu, H., 2003. Compressive behavior of concrete confined by various types of FRP composite jackets. J. Reinforc. Plast. Compos. 22, 1187–1202. https://doi.org/10.1177/0731684403035430.

Xie, T., Ozbakkaloglu, T., 2016. Behavior of recycled aggregate concrete-filled basalt and carbon FRP tubes. Constr. Build. Mater. 105, 132–143. https://doi.org/10.1016/j.conbuildmat.2015.12.068.

Xie, T., Gholampour, A., Ozbakkaloglu, T., 2018. Toward the development of sustainable concretes with recycled concrete aggregates: comprehensive review of studies on mechanical properties. J. Mater. Civ. Eng. 30, 4018211. https://doi.org/10.1061/(ASCE)MT.1943-5533.0002304.

Xu, J., Chen, W., Yu, Y., Xu, J., Zhao, X., 2022. Data-driven analysis on compressive behavior of unconfined and confined recycled aggregate concretes. Constr. Build. Mater. 356, 129282. https://doi.org/10.1016/j.conbuildmat.2022.129282.

Yang, Y., Xu, L., Huang, L., Yu, M., Chi, Y., 2024. A methodology for stress-strain behavior characterization and mixture optimization of recycled aggregate concrete based on machine learning. Mater. Today Commun. 38, 108109. https://doi.org/10.1016/j.mtcomm.2024.108109.

Youssef, M.N., Feng, M.Q., Mosallam, A.S., 2007. Stress-strain model for concrete confined by FRP composites. Compos. B Eng. 38, 614–628. https://doi.org/10.1016/j.compositesb.2006.07.020.

Yu, Y., Zheng, Y., Zhao, X.-Y., 2021. Mesoscale modeling of recycled aggregate concrete under uniaxial compression and tension using discrete element method. Constr. Build. Mater. 268, 121116. https://doi.org/10.1016/j.conbuildmat.2020.121116.

Zhang, N., Shen, S.-L., Zhou, A., Jin, Y.-F., 2021. Application of LSTM approach for modelling stress–strain behaviour of soil. Appl. Soft Comput. 100, 106959. https://doi.org/10.1016/j.asoc.2020.106959.

Zhang, S., Chen, W., Xu, J., Xie, T., 2024. Use of interpretable machine learning approaches for quantificationally understanding the performance of steel fiber-reinforced recycled aggregate concrete: from the perspective of compressive strength and splitting tensile strength. Eng. Appl. Artif. Intell. 137, 109170. https://doi.org/10.1016/j.engappai.2024.109170.

Zhao, J.L., Yu, T., Teng, J.G., Asce, M., 2014. Stress-strain behavior of FRP-confined recycled aggregate concrete. https://doi.org/10.1061/(ASCE)CC.1943-5614.

Zhao, X.Y., Chen, J.X., Chen, G.M., Xu, J.J., Zhang, L.W., 2023. Prediction of ultimate condition of FRP-confined recycled aggregate concrete using a hybrid boosting model enriched with tabular generative adversarial networks. Thin-Walled Struct. 182, 110318. https://doi.org/10.1016/J.TWS.2022.110318.

Zhou, Y.-W., Wu, Y.-F., 2012. General model for constitutive relationships of concrete and its composite structures. Compos. Struct. 94, 580–592. https://doi.org/10.1016/j.compstruct.2011.08.022.

Zhou, Y., Hu, J., Li, M., Sui, L., Xing, F., 2016. FRP-confined recycled coarse aggregate concrete: experimental investigation and model comparison. Polymers 8. https://doi.org/10.3390/polym8100375.

Zhou, J.K., Lin, G., Teng, J.G., 2021. Stress-strain behavior of FRP-confined concrete containing recycled concrete lumps. Constr. Build. Mater. 267. https://doi.org/10.1016/j.conbuildmat.2020.120915.